

AERO

TJ778  
.m41  
624  
no.181  
c.2



CHANNEL FLOW MODELING OF IMPINGEMENT  
COOLING OF A ROTATING TURBINE BLADE

by

JaHye Jenny Koo

GT&PDL Report No. 181

December 1984



**GAS TURBINE & PLASMA DYNAMICS LABORATORY**  
**MASSACHUSETTS INSTITUTE OF TECHNOLOGY**  
CAMBRIDGE, MASSACHUSETTS

CHANNEL FLOW MODELING OF IMPINGEMENT  
COOLING OF A ROTATING TURBINE BLADE

by

JaHye Jenny Koo

GT&PDL Report No. 181

December 1984

This research was supported by the NASA Lewis Research Center  
under Grant No. NAG3-335.

## ABSTRACT

Local heat transfer distributions in impingement cooling have been measured by Kreatsoulas [1] and Preiser [2] for a range of conditions which model those in actual turbine blades, including the effects of rotation. These data were reported as local Nusselt numbers, but referred to coolant supply conditions. By means of a channel flow modeling of the flow in the supply and impingement passages, the same data are here presented in terms of local Nusselt number distributions such as are used in design. The results in this form are compared to the nonrotating impingement results of Chupp [3] and to the rotating but non-impingement results of Morris [4]. Rotation reduces the mean Nusselt numbers from these found by Chupp by about 30 percent, and introduces important radial variations which are sensitive to rotation and to leading edge stagger angle.

## ACKNOWLEDGEMENTS

I would like to express my deepest appreciation to my advisor, teacher and friend, Professor Jack L. Kerrebrock. It was his enthusiasm, optimism and endless encouragement, as much as his extensive knowledge and hard work into this project throughout the year, which led to the completion of this work.

Special thanks to Professor Alan H. Epstein, Dr. Robert Norton, and Dr. Hyoun-Woo Shin for their comments and suggestions in the initial stage of the program.

My sincere thanks to Messrs. Bob Haines, Mike Giles, and Mark Drela for their patience in answering my numerous questions. Their personal warmth and invaluable assistance throughout the program helped me survive my first year at MIT.

## TABLE OF CONTENTS

	<u>Page</u>
Abstract	2
Acknowledgements	3
Table of Contents	4
Nomenclature	5
List of Tables and Figures	7
I. Introduction	8
II. Experimental Apparatus	11
III. Formulation of the Model	13
IV. Data Analysis	20
V. Results and Discussions	24
VI. Conclusion	28
References	29
Tables	30
Figures	32

## NOMENCLATURE

English Symbols

A	cross-sectional area	(sq. m)
C <sub>p</sub>	specific heat under constant	(J/Kg K)
d	impingement jet diameter	(m)
D	leading edge diameter	(m)
d <sub>e</sub>	equivalent diameter (A/s)	(m)
f	friction factor	
h	heat transfer coefficient	W/sq.m K)
k	thermal conductivity	(W/m K)
$\bar{M}$	Mach number	
Nu	Nusselt number	
p	pressure	(N/sq.m)
P	jet hole pitch	(m)
r	position vector	
r	radius	(m)
Re	Reynolds number	
s	perimeter	(m)
S	surface area	(sq.m)
S	jet span	(m)
St	Stanton number	
T <sub>s</sub>	average surface temperature	(K)
T <sub>f</sub>	average fluid temperature	(K)
T <sub>t</sub>	total fluid temperature	(K)

$T_w$	effective wall temperature	(K)
$u$	velocity vector	
$u$	velocity component in r direction	(m/sec)
$V_j$	impingement jet velocity	(m/sec)
$z$	wall to jet distance	(m)

#### Greek Symbols

$\gamma$	$C_p/C_v =$ specific heat ratio	
$\gamma$	stagger angle	(rad)
$\mu$	viscosity	(Nsec/sq.m)
$\rho$	density	(kg/cu.m)
$\Omega$	angular velocity	(rad/sec)

#### Subscripts

1	impingement channel
2	supply channel

## LIST OF TABLES AND FIGURES

	<u>Page</u>
<u>Tables</u>	
Table 1: Test section geometry	30
Table 2: Summary of -30 degree stagger angle tests	31
Table 3: Summary of 0 degree stagger angle tests	31
<u>Figures</u>	
Figure 1: Experimental apparatus schematic drawing	32
Figure 2: Blade model cross-section (side view)	33
Figure 3: Flow in radial coolant passage	34
Figure 4: Elementary radial volume	34
Figure 5: Test section geometry (top view)	
Figures 6-22: Local flow distribution and Nu for 30 degree stagger angle tests	36
Figures 23-34: Local flow distribution and Nu for 0 degree stagger angle tests	70

## I. INTRODUCTION

One of the most challenging tasks for advancing gas turbine technology is to improve gas turbine efficiency by increased turbine inlet temperature, while maintaining low enough metal temperature levels to achieve acceptable component life. To maintain acceptable temperatures of turbine components, it is necessary to develop effective cooling methods, and the importance of using coolant air in airfoils has been repeatedly emphasized. One of the most effective cooling methods for local internal cooling of turbine blades is jet impingement, which is achieved by blowing cooling air through a series of holes located inside the blades. The effectiveness of this internal cooling technique is measured by the heat transfer coefficient which gives the heat flux per temperature difference between the airfoil and the coolant.

The accurate prediction of the local convection heat transfer coefficient is essential in order to optimize the use of the coolant supply and minimize thermal stresses. Although numerous impingement heat transfer studies have been conducted and reported, most of the available data have been measured in stationary systems, so they do not address the rotational effects in impingement cooling systems. Recently, an extensive set of data on impingement cooling with rotational effects has been obtained by Kreatsoulas [1]. These experiments have revealed large effects due to rotation, on both the mean Nusselt number (averaged on the leading edge surface) and on the detailed heat transfer distribution, which is created by the impinging jets. All of Kreatsoulas' experiments were conducted with a -30 degree stagger angle, typical of the inlet of a high work rotor at the mean radius.

To assess the effect of stagger, the experiments were repeated by Preiser [2] with zero stagger and with the same geometry at similar conditions. These data give the local heat transfer rate on the leading edge surface of the blade model. Thus, they contain more detailed information than has been available from prior experiments, in addition to the effects of rotation. Previous experiments have averaged the heat transfer, over either the entire inner surface of a cooling passage or over radial strips.

The interpretation of this more detailed data, either for comparison with previous experiments or for application to design, is a complex matter because the fine details of the heat transfer distribution depend sensitively on the complex flow pattern in the impingement passage. The cooling pattern generated by any one impinging jet depends on its velocity, of course, but also on the temperature of the gas in the impingement passage at its radial location and on the corresponding radial velocity. For a given geometry, the velocity of each impingement jet depends on the pressures in the supply chamber and the impingement chamber, and the radial velocity in the impingement chamber depends on the temperature, pressure and mass flow there. All these quantities are sensitive to rotation, and, since it is not possible to measure them in the rotating experiment, they must be inferred theoretically.

The work presented here is an initial step toward modeling the flow in the impingement region of the blade, to include the effects of rotation. Considering the complexity of the flow, the modeling has been conceptually divided into two stages. In the first stage, which is addressed here, the flows in the supply passage and in the impingement region itself are both

modeled as channel flows, using friction coefficients and heat transfer coefficients which represent averages around the circumference of the passages, and are functions of the radial coordinate along each passage.

Because of the complexity of the flow, it has been possible to describe the effectiveness of impingement cooling only with reference to specific geometries. Thus, Ref. [3] gives correlations in terms of the jet Reynolds number, jet diameter, and the geometric parameters. We describe the effects of rotation relative to this correlation.

Some experiments have been conducted in simple rotating cylindrical passages which show the effects of rotation in such simple geometries and, again, we have compared the data of Kreatsoulas and Preiser with this data, to show the effect of the impingement jets on the heat transfer in the rotating passage. Within the channel flow approximation adopted here, the effects of rotation which are encompassed in the empirical correlations, at least in first approximation, are: 1) the radial pressure gradient in the supply and impingement passages, and its dependence on the heat addition in each passage, which is important in that it controls the flow rates in the impingement orifices, 2) the effect of buoyancy on the heat transfer, and 3) the averaged effect of Coriolis induced cross flow in the passages.

## II. EXPERIMENTAL APPARATUS

The experimental apparatus for study of impingement cooling in a rotating system was mainly designed and developed at the MIT Gas Turbine Laboratory and is described in detail by Kreatsoulas [1]. A brief description of the apparatus will be discussed in this section in order to present the modeling of the flow in the impingement region.

The apparatus consists of the rotor, the supporting structure, heat exchangers, instrumentation, calibrating body and blade model, as illustrated in Figure [1]. The blade model, which simulates the leading edge geometry of a real turbine blade, rotates in a vacuum chamber. The vacuum chamber is used to reduce heat transfer by convection from the outer wall to the environment, as well as to eliminate any absorbing medium between radiometer and measurement spot. The infrared radiometer measures the external surface temperature of the foil with a spatial resolution of about 1mm. The local heat transfer coefficients throughout the leading edge region of the blade are then determined from the measured electrical input power and the skin temperature distribution.

Figure [2] shows a geometric description of the flow system of the test model. A thin stainless steel foil (Kanthal A-1), a high resistivity and low thermal coefficient of resistivity material, is electrically heated by dissipation in the skin while being cooled from one side by impinging jets of refrigerant gas (Freon 12). The coolant enters into the supply plenum, flows through the jet holes to the impingement section, and exhausts radially to the exhaust channel. Inside the cooling passage of the model, type E thermocouples and pressure probes are placed to measure

the recovery temperatures and static pressures respectively.

A series of parametric studies was conducted with the described impingement test facility. The effects of rotation on impingement cooling were investigated by varying the following parameters:

1. low, medium, and high rotational speed -  
(850, 1450, and 2000 rpm);
2. low, medium, and high coolant mass flow -  
(0.005, 0.010, and 0.020 kg/sec);
3. low and high temperature ratio between the model  
skin and the inlet coolant temperature -  
(1.196 and 1.243);
4. stagger angle (-30 and 0 degrees).

### III. FORMULATION OF THE MODEL

Figure [3] illustrates a tube rotating about an axis with a constant angular velocity. Fluid flows in the tube and the motion of this fluid is referred to as a reference coordinate system  $(r, \theta, z)$ . The acceleration vector of a fluid particle, which has a position vector  $\vec{r}$  and a velocity vector  $\vec{u}$ , relative to the rotating coordinate system is

$$\vec{a} = \frac{D\vec{u}}{Dt} + 2\vec{\Omega} \times \vec{u} + \vec{\Omega} \times (\vec{\Omega} \times \vec{r}) \quad (1)$$

$D\vec{u}/Dt$ ,  $2\vec{\Omega} \times \vec{u}$ , and  $\vec{\Omega} \times (\vec{\Omega} \times \vec{r})$  refer respectively to the total derivative of the velocity vector, Coriolis acceleration, and the centrifugal acceleration.

The Navier-Stokes equation may then be approximated as

$$\rho \frac{D\vec{u}}{Dt} + 2\vec{\Omega} \times \vec{u} + \vec{\Omega} \times (\vec{\Omega} \times \vec{r}) = -\nabla p + \mu \nabla^2 \vec{u} \quad (2)$$

where  $\rho$ ,  $\mu$ , and  $p$  are the density, viscosity, and pressure of the fluid respectively. For a steady flow in the radial direction, Eq. (2) may be simplified as

$$\rho u \frac{\partial u}{\partial r} - \rho \Omega^2 r = -\frac{\partial p}{\partial r} + \mu \nabla^2 u \quad (3)$$

Equation (3), however, does not include the effects of the incoming jets from the supply channel, which we shall assume enter the impingement passage with zero radial momentum. If an elementary radial volume, as shown in Fig. 4, is considered, the momentum balance becomes

$$-\frac{dp}{dr} = \rho u \frac{du}{dr} + u \frac{d}{dr} (\rho u) \quad (4)$$

From continuity,

$$\frac{d}{dr} (\rho u A) = \rho V_j \frac{dA_j}{dr} \quad (5)$$

where  $A$  is the cross-sectional area of the passage,  $\rho V_j$  is the mass flux per unit area through the jets, and  $dA_j/dr$  is the total jet area per unit passage height. For a constant passage area, Eq. (5) becomes

$$\frac{d}{dr} (\rho u) = \frac{\rho V_j}{A} \frac{dA_j}{dr} \quad (6)$$

Substituting Eq. (6) into Eq. (4),

$$-\frac{dp}{dr} = \rho u \frac{du}{dr} + \frac{\rho u V_j}{A} \frac{dA_j}{dr} \quad (7)$$

Replacing the viscous term by an equivalent pipe flow representation and substituting Eq. (7) into Eq. (3), the equation of motion may be expressed as follows.

$$\rho u \frac{du}{dr} + \frac{\rho u V_j}{A} \frac{dA_j}{dr} - \rho \Omega^2 r + \frac{f}{d_e} \frac{\rho u^2}{2} = -\frac{dp}{dr} \quad (8)$$

$f$  and  $d_e$  are the friction factor and the equivalent diameter of the passage respectively. For the impingement and supply, regions which are denoted with subscripts 1 and 2 respectively, these equations become

$$-\frac{dp_1}{dr} = \rho_1 u_1 \frac{du_1}{dr} + \frac{\rho_2 u_1 V_j}{A_1} \frac{dA_j}{dr} - \rho_1 \Omega^2 r + \frac{f}{d_{e1}} \frac{\rho_1 u_1^2}{2} \quad (9)$$

$$-\frac{dp_2}{dr} = \rho_2 u_2 \frac{du_2}{dr} - \rho_2 \Omega^2 r + \frac{f}{d_{e2}} \frac{\rho_2 u_2^2}{2} \quad (10)$$

$$\frac{d}{dr} (\rho_1 u_1 A_1) = \rho_2 V_j \frac{dA_j}{dr} \quad (11)$$

$$\frac{d}{dr} (\rho_2 u_2 A_2) = -\rho_2 V_j \frac{dA_j}{dr} \quad (12)$$

$$v_j = [2(p_2 - p_1)/\rho_2]^{1/2}, \quad p_2 > p_1 \quad (13)$$

The energy equation can be derived in a similar manner as the equation of motion by taking a radial element. The heat transfer rate across the surface  $dS$  is written in terms of the heat transfer coefficient and the temperature difference as

$$dq = h(T_w - T)dS \quad (14)$$

As a first approximation, the heat transfer rate is estimated by taking the temperature difference between the average temperature of the fluid  $T$  and the effective wall temperature  $T_w$ , which is assumed to be constant along the passage.  $T_w$  is defined as

$$T_w = \frac{A_1 T_s + A_2 T_f}{A_1 + A_2} \quad (15)$$

where

$A_1$  = impingement channel cross-sectional area

$A_2$  = supply channel cross-sectional area

$T_s$  = average surface temperature

$T_f$  = average fluid temperature

In the final heat transfer coefficient calculation,  $T_w$  is replaced with the measured local wall temperature, and  $T$  is replaced with the local fluid temperature. This is to be described in detail in IV.

The average heat transfer coefficient, as a first approximation, is estimated by applying the following analogies. The Reynolds analogy, which assumes complete similarity of momentum and heat transfer, provides the following equation.

$$St = \frac{Nu}{Pr Re} = \frac{h}{\rho c_p u} \quad (16)$$

The Stanton number,  $St$ , is a ratio of the Nusselt number and the product of the Reynolds and Prandtl numbers.  $C_p$  is the specific heat of the fluid. The Colburn analogy expresses the product of the Stanton and Prandtl numbers in terms of friction factor,  $f$ .

$$St Pr^{2/3} = \frac{1}{2} C_f = \frac{1}{8} f \quad (17)$$

Combining Eqs. (15) and (16), and assuming the Prandtl number to be approximately equal to 1, a simple relation between friction loss and heat transfer may be obtained.

$$St = \frac{h}{\rho c_p u} = \frac{1}{8} f \quad (18)$$

Substituting  $dS = \pi d_e dr$  and  $h = St \rho c_p u$ , Eq. (14) becomes

$$dq = St \rho c_p u (T_w - T) \pi d_e dr \quad (19)$$

By taking an energy balance on a small radial element of  $dr$ , the following equations are obtained.

For the impingement region,

$$\begin{aligned} \rho_1 u_1 A_1 c_p \frac{dT_{t_1}}{dr} = & \pi d_e \rho_1 u_1 c_p (T_w - T_{t_1}) St + \rho_1 \Omega^2 r u_1 A_1 \\ & + \rho_2 V_j c_p (T_{t_2} - T_{t_1}) \frac{dA_j}{dr} + kA_1 \frac{d^2 T_{t_1}}{dr^2} \end{aligned} \quad (20)$$

and for the supply region,

$$\rho_2 u_2 A_2 c_p \frac{dT_{t_2}}{dr} = \pi d_e \rho_2 u_2 c_p (T_w - T_{t_2}) St + \rho_2 \Omega^2 r u_2 A_2 \quad (21)$$

where the total temperatures

$$T_{t_1} = T_1 + \frac{u_1^2}{2c_p}$$

and

(22)

$$T_{t_2} = T_2 + \frac{u_2^2}{2c_p}$$

The final six differential equations describing the flow characteristics derived for the regions of interest are presented in non-dimensional form as follows.

Impingement region,

$$\begin{aligned} \frac{1-M_1^2}{1+\frac{\gamma-1}{2}M_1^2} \frac{r}{u_1} \frac{du_1}{dr} &= \frac{\pi d_1 r}{A_1} \left( \frac{T_w}{T_{t_1}} - 1 \right) St + \left( \frac{\rho_2 V_j}{\rho_1 u_1} \right) \left[ \frac{1+\gamma M_1^2}{1+\frac{\gamma-1}{2}M_1^2} + \frac{T_{t_2}}{T_{t_1}} - 1 \right] \frac{r}{A_1} \frac{dA_j}{dr} \\ &- \frac{M_{T_1}^2}{1+\frac{\gamma-1}{2}M_1^2} + \frac{\gamma M_1^2/2}{1+\frac{\gamma-1}{2}M_1^2} \frac{s_1}{A_1} r \\ &- \frac{1+\gamma M_1^2}{1+\frac{\gamma-1}{2}M_1^2} \frac{r}{A_1} \frac{dA_1}{dr} + \frac{k}{\rho_1 u_1 c_p} \frac{r}{T_{t_1}} \frac{d^2 T_{t_1}}{dr^2} \end{aligned} \quad (23)$$

$$\begin{aligned} \frac{r}{T_{t_1}} \frac{dT_{t_1}}{dr} &= \frac{\pi d_1 r}{A_1} \left( \frac{T_w}{T_{t_1}} - 1 \right) St + \left( \frac{\rho_2 V_j}{\rho_1 u_1} \right) \left[ \frac{T_{t_2}}{T_{t_1}} - 1 \right] \frac{r}{A_1} \frac{dA_j}{dr} \\ &+ \frac{(\gamma-1)M_{T_1}^2}{1+\frac{\gamma-1}{2}M_1^2} + \frac{k}{\rho_1 u_1 c_p} \frac{r}{T_{t_1}} \frac{d^2 T_{t_1}}{dr^2} \end{aligned} \quad (24)$$

$$\begin{aligned} \frac{r}{p_1} \frac{dp_1}{dr} &= (1 + \frac{\gamma-1}{2} M_1^2) \frac{r}{T_{t_1}} \frac{dT_{t_1}}{dr} - [1 + (\gamma-1)M_1^2] \frac{r}{u_1} \frac{du_1}{dr} \\ &+ \frac{\rho_2}{\rho_1} \left(\frac{v_j}{u_1}\right) \frac{r}{A_1} \frac{dA_j}{dr} - \frac{r}{A_1} \frac{dA_1}{dr} \end{aligned} \quad (25)$$

Supply region,

$$\begin{aligned} \frac{1-M_2^2}{1+\frac{\gamma-1}{2}M_2^2} \frac{r}{u_2} \frac{du_2}{dr} &= \frac{\pi d_2 r}{A_2} \left(\frac{T_w}{T_{t_2}} - 1\right) St + \left(\frac{v_j}{u_2}\right) \frac{1}{1+\frac{\gamma-1}{2}M_2^2} \frac{r}{A_2} \frac{dA_j}{dr} \\ &- \frac{M_{T_2}^2}{1+\frac{\gamma-1}{2}M_2^2} + \frac{\gamma M_2^2/2}{1+\frac{\gamma-1}{2}M_2^2} \frac{s_2}{f_{A_2} r} - \frac{1+\gamma M_2^2}{1+\frac{\gamma-1}{2}M_2^2} \frac{r}{A_2} \frac{dA}{dr} \end{aligned} \quad (26)$$

$$\frac{r}{T_{t_2}} \frac{dT_{t_2}}{dr} = \frac{\pi d_2 r}{A_2} \left(\frac{T_w}{T_{t_2}} - 1\right) St + \frac{(\gamma-1)M_{T_2}^2}{1 + \frac{\gamma-1}{2} M_2^2} \quad (27)$$

$$\frac{r}{p_2} \frac{dp_2}{dr} = (1 + \frac{\gamma-1}{2} M_2^2) \frac{r}{T_{t_2}} \frac{dT_{t_2}}{dr} - [1 + (\gamma-1)M_2^2] \frac{r}{u_2} \frac{du_2}{dr} - \frac{r}{A_2} \frac{dA_2}{dr} \quad (28)$$

where

$$M_1^2 = \frac{u_1^2}{\gamma R T_1} = \frac{u_1^2}{\gamma R T_{t_1}} \left(1 + \frac{\gamma-1}{2} \bar{M}_1^2\right) \quad (29a)$$

$$M_2^2 = \frac{u_2^2}{\gamma R T_2} = \frac{u_2^2}{\gamma R T_{t_2}} \left(1 + \frac{\gamma-1}{2} \bar{M}_2^2\right) \quad (29b)$$

$$M_{T_1}^2 = \frac{\Omega^2 r^2}{\gamma R T_1} = \frac{\Omega^2 r^2}{\gamma R T_{t_1}} \left(1 + \frac{\gamma-1}{2} \bar{M}_1^2\right) \quad (29c)$$

$$M_{T_2}^2 = \frac{\Omega^2 r^2}{\gamma R T_2} = \frac{\Omega^2 r^2}{\gamma R T_{t_2}} \left(1 + \frac{\gamma-1}{2} M_2^2\right) \quad (29d)$$

where  $\bar{M}$  = Mach number.

The measured total temperatures and the static pressures at the passage hub of both the impingement and supply channels are prescribed as initial conditions for integration of these equations. The velocities at the passage hub of the regions are prescribed as  $u_1 = 0$  and  $u_2 = \dot{m}/\rho_2 A_2$  where  $\dot{m}$  is the total mass flow rate entering the supply region.

#### IV. DATA ANALYSIS

The solutions of the differential equations derived in III enable one to obtain the local flow distribution, which further gives the circumferentially averaged flux to the coolant along the radius. In this section, a method of determining the local flow distribution and heat transfer distribution is outlined.

From the measured heat fluxes Kreatsoulas and Preiser calculated, the local heat transfer coefficient  $h$  of the leading edge surface using the definition

$$h_c = q/(T - T_c) \quad (30)$$

where  $T_c$  is the measured inlet coolant temperature, and  $q$  and  $T$  are the measured local heat flux and skin temperature, respectively. The value of  $h_c$ , calculated using Eq. (30), is based on coolant inlet temperature to the blade, so it includes a number of complex effects, such as heating of the fluid in the supply passage and variations in jet Reynolds number due to differential pressure drops in the supply and impingement passages. A more useful correlation of the local heat transfer distribution may be obtained by basing  $h$  on the local fluid temperature  $T_f$  in the jets, and by correlating in terms of the local jet Reynolds number. Thus,

$$h_f = q/(T - T_f) \quad (31)$$

For the channel flow analysis, the heat transfer coefficient is averaged around the circumference of the passage along the radius, and Eq. (30) becomes,

$$\langle h \rangle_c = \langle q \rangle / (\langle T \rangle - T_c) \quad (32)$$

where  $\langle q \rangle$  and  $\langle T \rangle$  are the measured heat flux and skin temperature, respectively, averaged in the theta direction. Similarly, the circumferentially averaged heat transfer based on local fluid temperature is

$$\langle h \rangle_f = \langle q \rangle / (\langle T \rangle - T_f) \quad (33)$$

The local flow distribution, which includes the local fluid temperature along the radius, is then determined by solving the six differential equations simultaneously with the prescribed initial conditions and the geometric dimensions. Figure 5 and Table 1 present a schematic drawing of the model section and the blade description which provide the necessary geometric dimensions considered in this analysis. The complete solutions provide the local distributions of velocity, pressure, and temperature and, subsequently, the local circumferentially averaged flux to the coolant along the radius.

The differential equations are solved by a computer program which includes subroutine Runge-Kutta-Merson numerical method. This numerical integration routine is a modified version of the fourth-order Runge-Kutta method which involves additional evaluation of a function in the differential equation at each step. This method requires only the initial values of the dependent variables, and also enables the step width to be adjusted automatically as the solution proceeds. As a first approximation, Eq. (17) is used to estimate the average heat transfer where friction factor  $f$  is initially set to 0.02, an approximate value for turbulent flow. Stanton number is then recalculated from the Nusselt number correlation obtained by

Chupp, et al. (Eq. 34) which is expressed as a function of geometric parameters and the jet Reynolds number.

$$\text{Nu}_{\text{avg}} = 0.63 \text{Re}_d^{0.7} \left(\frac{d}{p}\right)^{0.5} \left(\frac{d}{D}\right)^{0.6} \exp[-1.27 \left(\frac{S}{d}\right) \left(\frac{d}{p}\right)^{0.5} \left(\frac{d}{D}\right)^{1.2}] \quad (34)$$

Nu is an arithmetic average of the Nusselt number for strips located in the leading edge region.  $\text{Re}_d$  is the jet Reynolds number which is defined as  $\text{Re} = V_j \rho_2 d / \mu$  where  $d$  is the hole diameter. The friction factor is also recalculated as a function of local Reynolds number.

$$f = \frac{0.0791}{\text{Re}_d^{0.25}} \quad (35)$$

An approximate flow distribution is determined from the calculated average Nusselt number and friction factor based on Eqs. (34) and (35), respectively, with the prescribed initial conditions.

The calculated and measured values of the pressure ratio between impingement and supply regions at the inlet are compared. Then an iteration method is applied to satisfy the continuity and zero mass flow at the tip of the supply region.

In the next and final iteration, the Stanton number defined in Eq. (16) is calculated from the average heat transfer, calculated by using Eq. (32). Subsequently, the new local heat transfer averaged in the theta direction, which is based on the temperature difference between the local skin temperature and fluid temperature, is calculated as defined in Eq. (33).

This analysis is applied to all the test data obtained by Kreatsoulas and Preiser. The new calculated heat transfer distribution is then compared with the correlations obtained by other investigators to ensure that the

experimental results and the modeling formulation are satisfactory. In particular, the results reported by Chupp, et al. [3] and Morris and Ayhan [4] are closely examined. The report by Chupp, et al. presents the impingement effect on heat transfer in a stationary system while the report by Morris and Ayhan includes the rotational effect on heat transfer in coolant channels.

## V. RESULTS AND DISCUSSION

The independent parameters of primary interest in the present study are Reynolds number, rotational speed, heat input, and stagger angle. Tables 2 and 3 summarize the series of parametric studies performed by Kreatsoulas and Preiser which are considered in this analysis. Figures 6A to 34C are the graphical representation of the calculated local flow distribution for all the cases. In Figures 6A to 22C, the velocity, pressure, and temperature of the fluid in both the impingement and supply channels are plotted for each test conducted at -30 degree stagger angle. The results of the local flow distribution calculated for 0 degree stagger angle are similarly illustrated in Figs. 23A to 34C. On the temperature vs radius graphs, the temperatures measured by thermocouples at the passage hub and tip are also plotted.

In the impingement passage, the initial condition was applied that  $T_{t_1}$  should be equal to the value given by the thermocouple at the base of the impingement passage, and in the region below the first jet, conduction in the radial direction was included in the energy equation. This is why the temperature shows an initial drop before rising due to convective heating.

The outer thermocouple gave fluid temperatures quite different from those computed, and quite inconsistent with the measured heat transfer values. We infer that such measurements are unreliable in the complex, thermally stratified flow found in the impingement passage.

Figures 6D to 22D and 23D to 34D present the Nusselt numbers averaged around the circumference of the passage along the radius for the 30 and 0 degree stagger angle tests. Rotation introduces important radial variations

in heat transfer, which are sensitive to rotation and to leading edge stagger angle. The results show that the Nusselt numbers averaged around the circumference show more distinct traces of heat transfer measurement, showing modulations due to the individual jets along the radius, than the Nusselt numbers averaged in radial strips, as illustrated in Ref. [1]. The calculated Nusselt numbers, based on the local gas temperature, are plotted and compared with the calculated Nusselt numbers based on the inlet coolant temperature. In examining all the plots, it is shown that the difference between them is relatively small, having the maximum difference of about 17 percent.

The effect of rotation on heat transfer is investigated by examining its variation with rotational speed at the same nominal conditions. Figures 11D, 17D, and 22D show the results of the heat transfer measurement averaged around the circumference of the passage at different rotational speeds corresponding to 850, 1425, and 2000 rpm. All three tests were conducted at 30 degree stagger angle, keeping the Reynolds number and the wall to coolant temperature at the highest values.

The average Nusselt numbers do not vary significantly as the rotational speed increases from 850 to 2000 rpm. However, a steep thermal gradient is present between the first and second jet holes at high rotational speed. The flow pattern of the jets is determined by the balance of the Coriolis and centrifugal buoyancy accelerations. The tangential velocity variation tends to deflect each jet toward the hub while the buoyancy effect, as well as the pressure gradient of the cross flow, tends to deflect it toward the tip. Since the first jet, which is located near the base of the passage,

is subject to minimal cross flow and buoyancy effects, it is dominated by the tangential velocity effect and deflects toward the hub. The third jet, under the influence of increasing buoyancy and cross flow, is deflected toward the tip and hence creates a large thermal gradient.

The effect of Reynolds number on heat transfer can be examined by comparing Figs. 13D, 15D, and 17D. In all three cases, the tests were conducted at medium rotational speed and high temperature ratio at 30 degree stagger angle. As the average jet Reynolds number varies from 17000 to 74000, the heat transfer rate increases about three times, the average values ranging from 100 to 280. Similar trends are shown for the low and high speed cases but, at the high rotational speed, the thermal gradients between the jet holes along the passage are more pronounced. For the 0 stagger cases, Figs. 26D and 31D show the increase in heat transfer rate by a factor of 2 as the Reynolds number increases from low to medium. In all the cases, the temperature ratio between the average skin temperature and the coolant temperature seems to have almost no effect on Nusselt number as shown in Figs. 21D and 22D.

The stagger angle effect on impingement-cooled rotating blades is examined by comparing the data obtained by Kreatsoulas and Preiser, which are conducted at 30 and 0 stagger angles, respectively, holding all other nominal conditions the same. Figures 22D and 34D show that the heat transfer rate are lower at zero degrees by approximately 30%, and the high thermal gradient effect due to the dominant tangential velocity effect between the second and third jets is not seen at this angle.

Also indicated in Figs. 6D to 34D are the comparable Nusselt number

results from Refs. [3] and [4] at the corresponding Reynolds and Rossby numbers. It is shown that the result from Chupp [3] predicts about 30 percent higher Nusselt numbers, which do not include the rotational effect. In Ref. [4], Morris and Ayhan report the effect of rotation on the Nusselt number but without the influence of impingement cooling, which results in lower heat transfer than the present work. At the tip section of the model where there is no impingement cooling, the Nusselt numbers coincide with these found by Morris.

## VI. CONCLUSION

A channel flow model of flow in the impingement cooling passage of a rotating turbine blade leading edge is used to correct measured heat transfer coefficients to local fluid conditions. The flows in the supply and impingement regions are both modeled as steady state channel flows, using friction and heat transfer coefficients. The local flow properties are obtained by solving the momentum, mass and energy equations with the prescribed initial conditions, and using the local heat transfer rates calculated from the data of Kreatsoulas and Preiser. The local Nusselt number, based on calculated local fluid temperature, is re-evaluated by circumferentially averaging the heat transfer rate. When this result is compared with the Nusselt number, based on the inlet coolant temperature, the maximum difference between them is determined to be about 17 percent. By comparing the calculated Nusselt numbers with the correlations obtained by other investigators, it is concluded that the experimental and modeling formulations are satisfactory. The modeling and the analysis illustrated here, therefore, offer a means for more accurate prediction of impingement cooling heat transfer rates.

## REFERENCES

1. Kreatsoulas, J.C., "Experimental Study of Impingement Cooling in Rotating Turbine Blades," Ph.D Thesis, MIT Department of Aeronautics and Astronautics, September 1983.
2. Preiser, Uriel Z., "Stagger Angle Effects on Impingement Cooling of a Rotating Turbine Blade," M.S. Thesis, MIT Department of Aeronautics and Astronautics, May 1984.
3. Chupp, R.E., Helms, H.E., McFadden, P.W. and Brown, T.R., "Evaluation of Internal Heat Transfer Coefficients for Impingement Cooled Turbine Airfoils," Journal of Aircraft, Vol. 6, 1969, pp. 203-208.
4. Morris, W.D. and Ayhan, T., "Observations on the Influence of Rotation on Heat Transfer in the Coolant Channels of Gas Turbine Rotor Blades," Proceedings of the Institute of Mechanical Engineers, Vol. 193, 1979, pp. 303-311.

TABLE 1: TEST SECTION GEOMETRY

Span	S	101.6 mm	4.000 in
Hub radius	Rh	406.4 mm	16.000 in
Tip radius	Rt	508.0 mm	20.000 in
Leading edge diameter	D	12.7 mm	0.500 in
Stagger angle (from axial)	$\gamma$	0.523 rad	30.0 deg
Impingement hole diameter	d	2.1 mm	0.081 in
Impingement hole pitch	p	6.1 mm	0.240 in
Wall to jet distance	z	4.1 mm	0.162 in
Impingement insert span	Si	76.2 mm	3.000 in

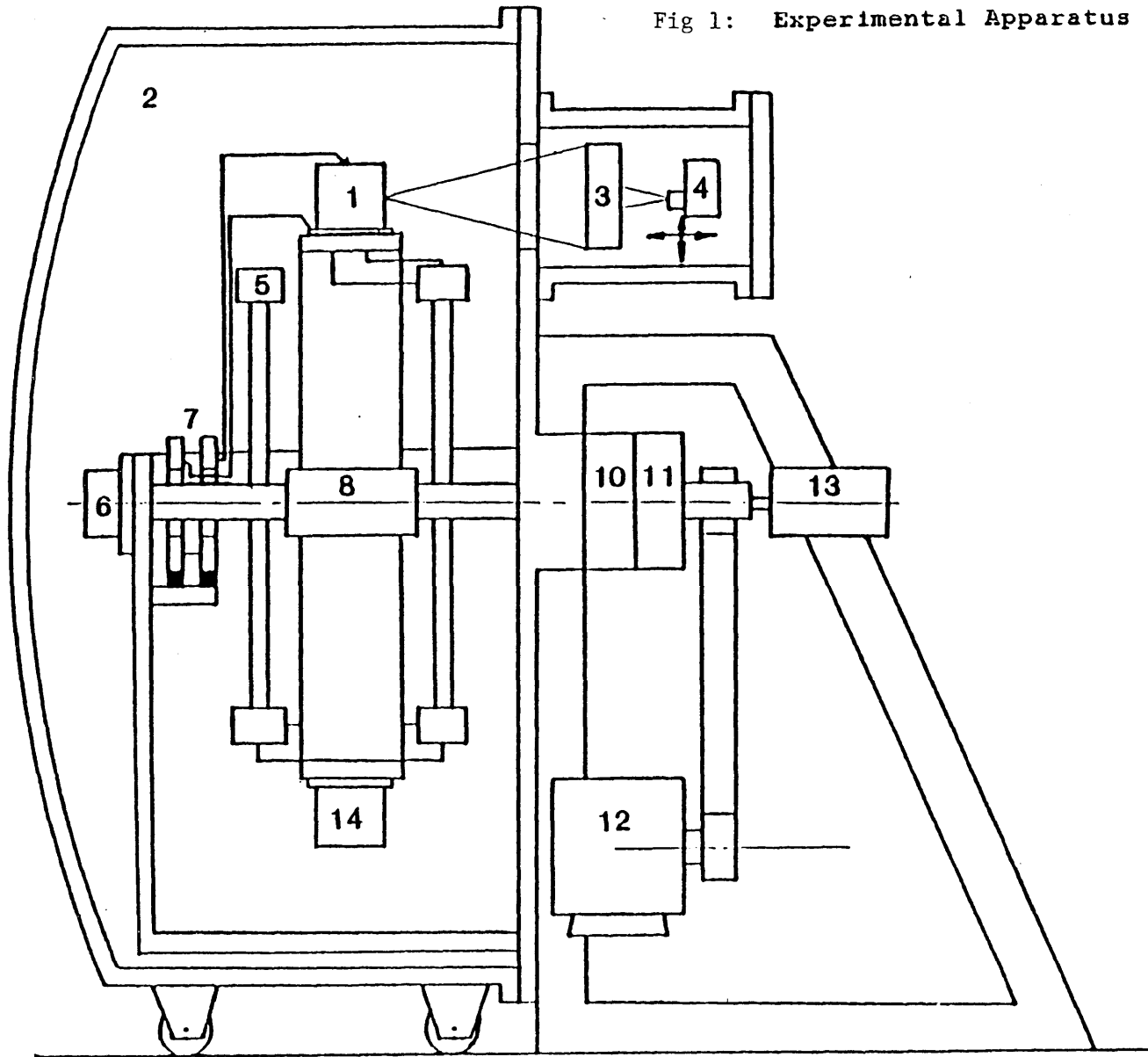
TABLE 2: -30 degree stagger angle tests

TEST #	ROTATIONAL SPEED	RE #	TW/TC
43	low	low	low
42	low	low	high
39	low	medium	low
44	low	medium	high
40	low	high	low
41	low	high	high
57	medium	low	low
56	medium	low	high
55	medium	medium	low
54	medium	medium	high
59	medium	high	low
58	medium	high	high
63	high	low	low
65	high	medium	low
64	high	medium	high
66	high	high	low
67	high	high	high

TABLE 3: 0 degree stagger angle tests

TEST #	ROTATIONAL SPEED	RE #	TW/TC
113	low	low	high
114	low	medium	high
115	low	medium	high
123	medium	low	high
124	medium	low	high
122	medium	medium	low
119	medium	medium	high
120	medium	medium	high
121	medium	medium	high
128	high	medium	low
126	high	medium	high
127	high	high	high

Fig 1: Experimental Apparatus Schematic Drawing



- 1. Blade Model
- 2. Vacuum Chamber
- 3. Imaging System
- 4. IR Detector
- 5. Heat Exchanger
- 6. Encoder
- 7. Power Slip Rings
- 8. Gun Bored Shaft
- 9. Seal
- 10. R-12 Inlet
- 11. R-12 Outlet
- 12. Var. Speed Drive
- 13. Instr. Slip Rings
- 14. Calibration Body

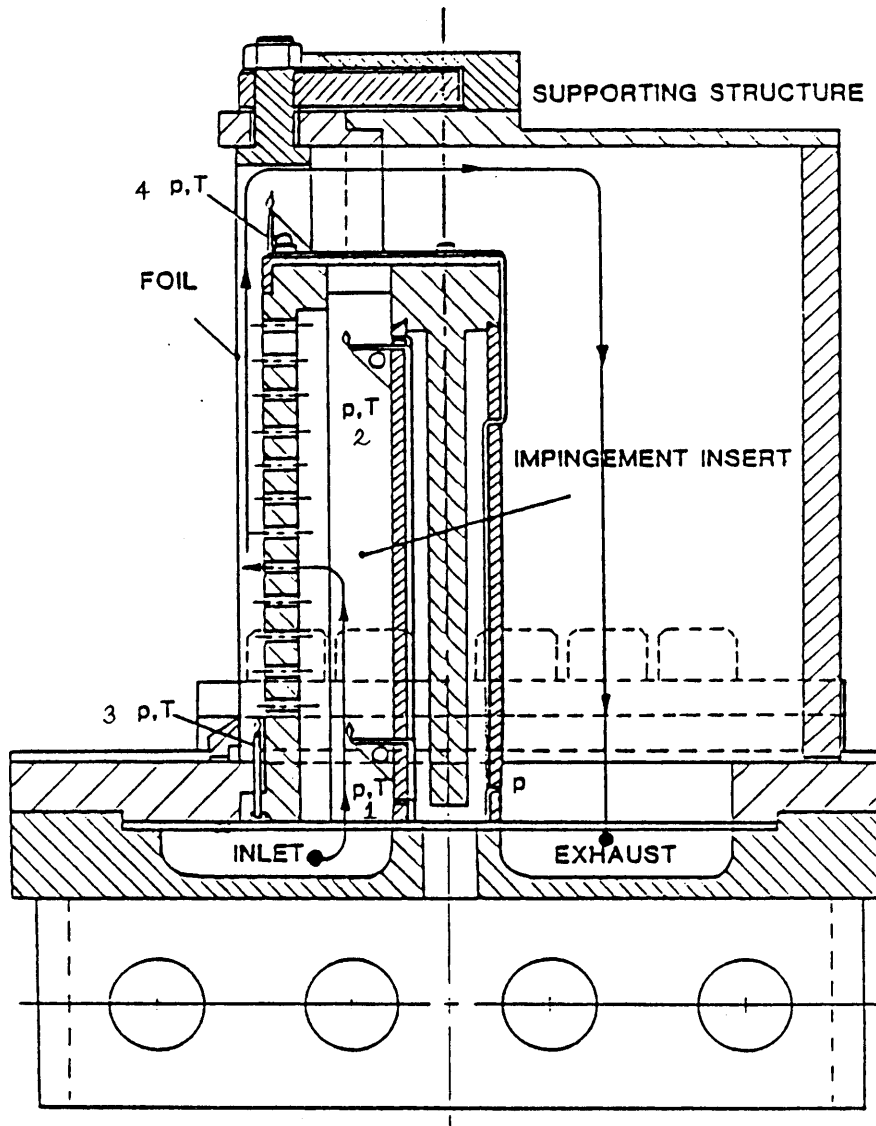


Fig. 2: Blade Model Cross Section (Side View)  
 1. T - Thermocouple  
 2. P - Pressure Tap

Thermocouple and pressure tap locations\*

1. 0.3905 m
2. 0.4747 m
3. 0.4008 m
4. 0.4921 m

\* measured from the center of the shaft

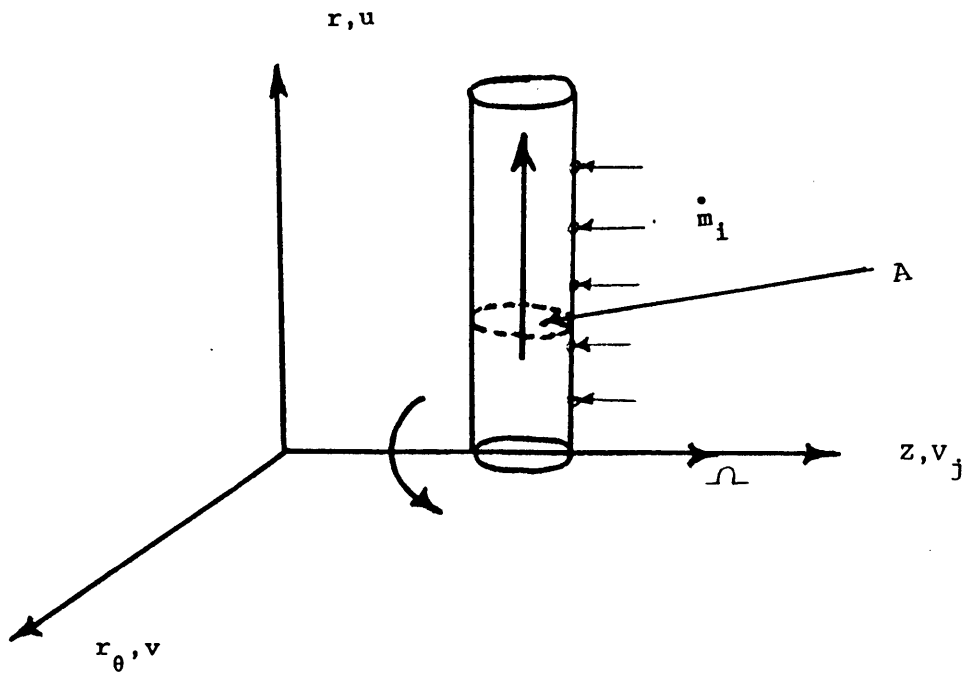


Figure 3: Flow in radial coolant passage

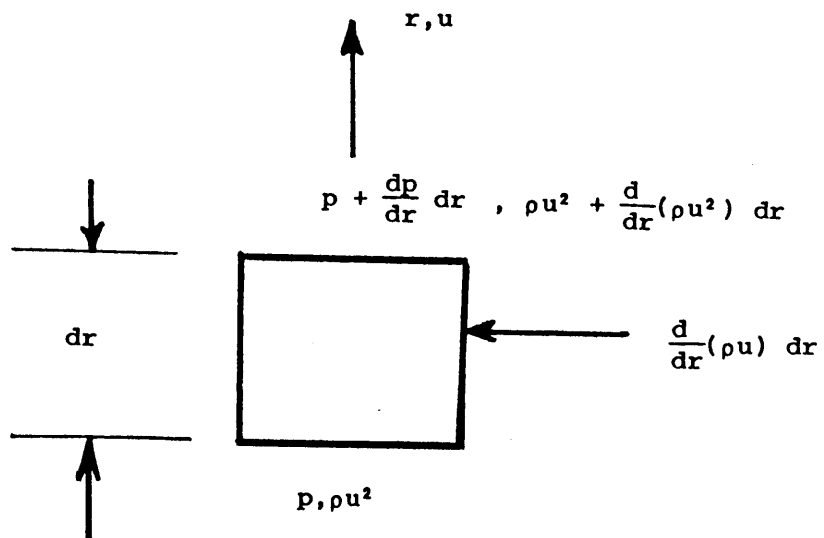


Figure 4: Elementary radial volume

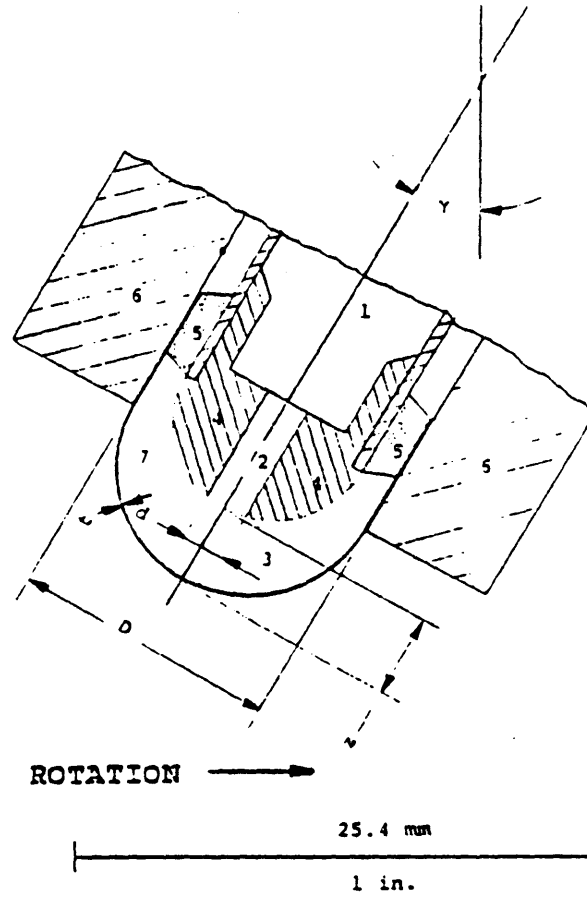


Fig 5: Test Section Geometry (Top View)

1. Supply Plenum
2. Jet Hole
3. Impingement Space
4. Impingement Insert
5. Rubber Seal
6. Cover
7. Resistive Wall

VELOCITY VS RADIUS

TEST #: 43

SYMBOLS: IMPINGEMENT -  $\circ$   
 SUPPLY - X

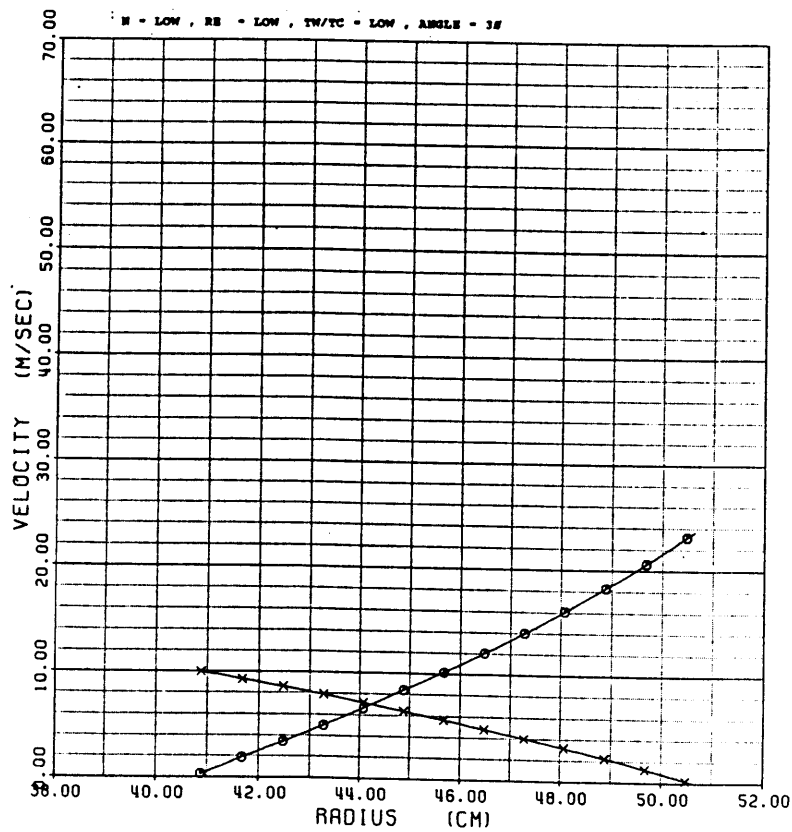


Figure 6A

PRESSURE VS RADIUS

TEST #: 43

SYMBOLS: IMPINGEMENT -  $\circ$   
 SUPPLY - X

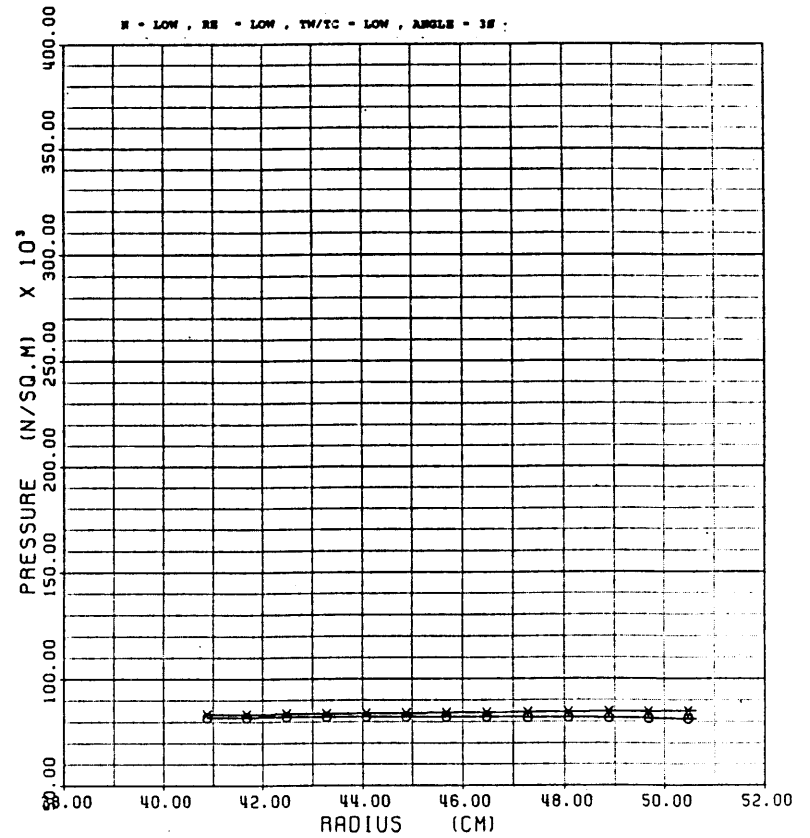


Figure 6B

### TEMPERATURE VS RADIUS

TEST #: 43

SYMBOLS: IMPINGEMENT - ○  
 SUPPLY - X  
 THERMOCOUPLE - ▲

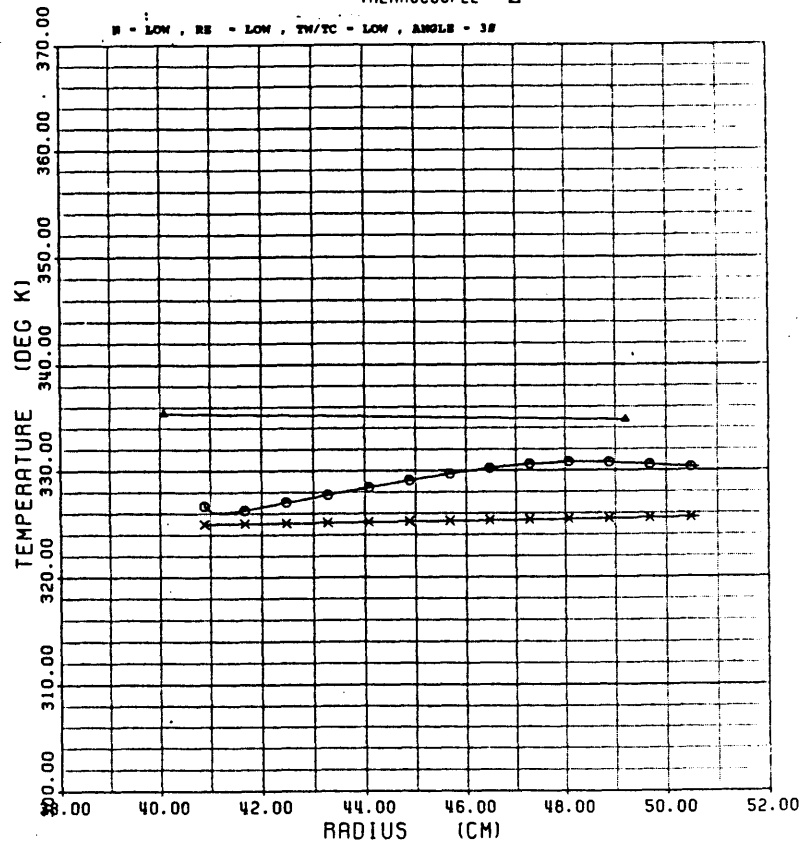


Figure 6C

### AVERAGE NUSSELT NUMBER

TEST #: 43

SYMBOLS: NU NO BASED ON LOCAL GAS TEMP - ○  
 NU NO BASED ON COOLANT TEMP - X  
 CHUPP'S CORRELATION - ▲  
 MORRIS' CORRELATION - □

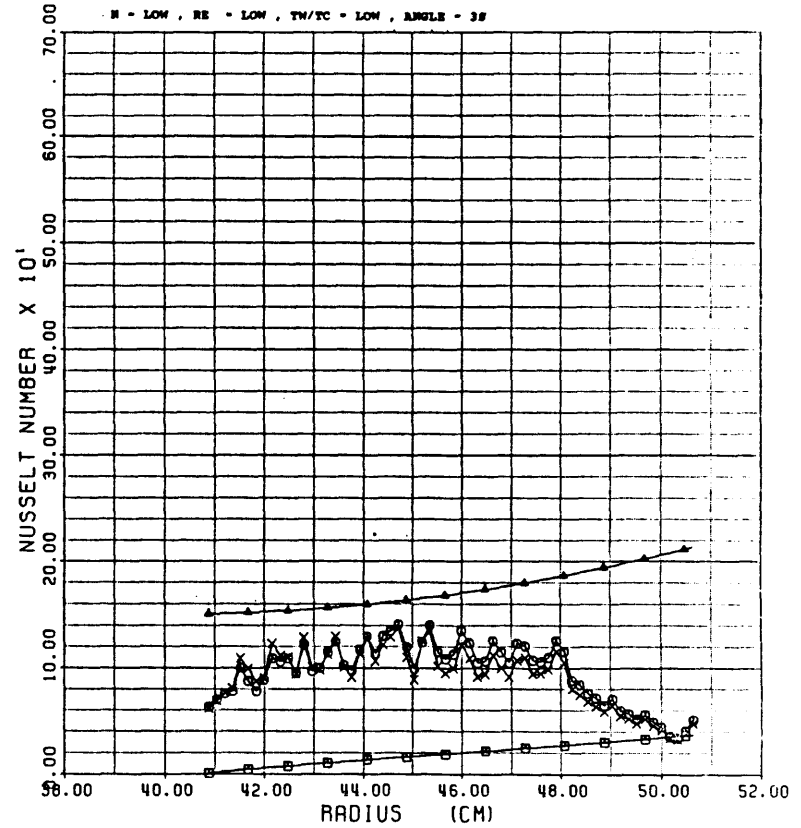


Figure 6D

# VELOCITY VS RADIUS

TEST #: 42

SYMBOLS: IMPINGEMENT - O  
SUPPLY - X

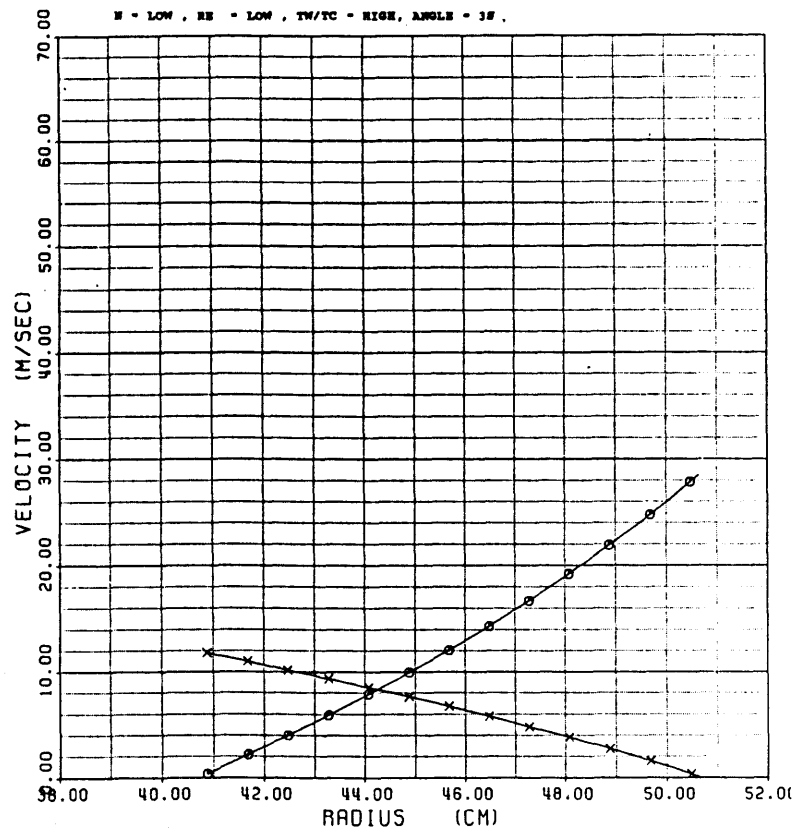


Figure 7A

# PRESSURE VS RADIUS

TEST #: 42

SYMBOLS: IMPINGEMENT - O  
SUPPLY - X

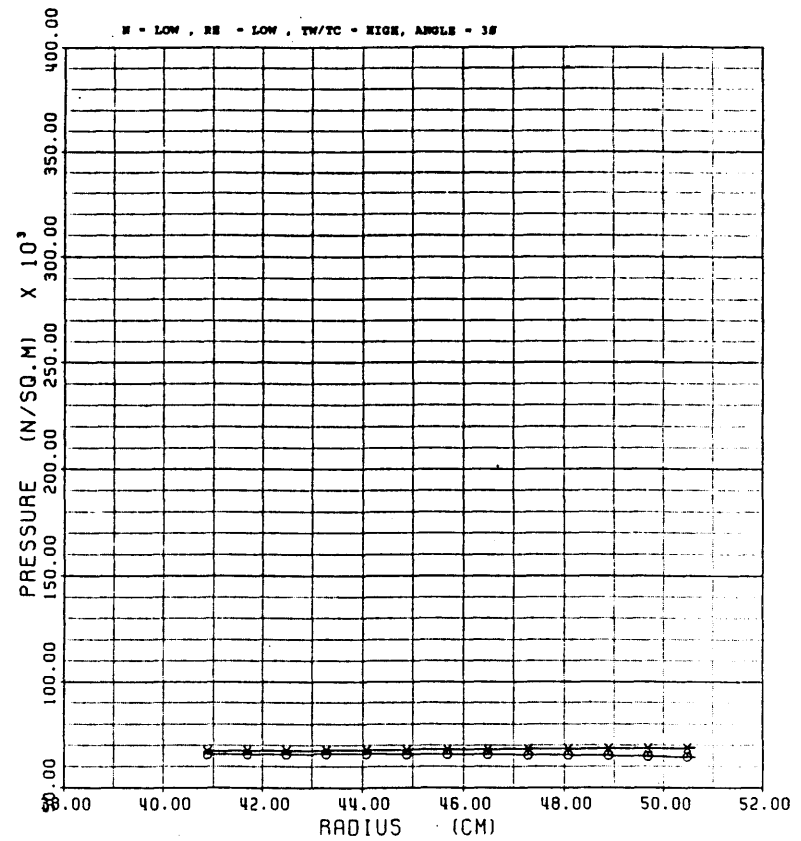


Figure 7B

### TEMPERATURE VS RADIUS

TEST #: 42

SYMBOLS: IMPINGEMENT -  $\circ$   
 SUPPLY -  $\times$   
 THERMOCOUPLE -  $\triangle$

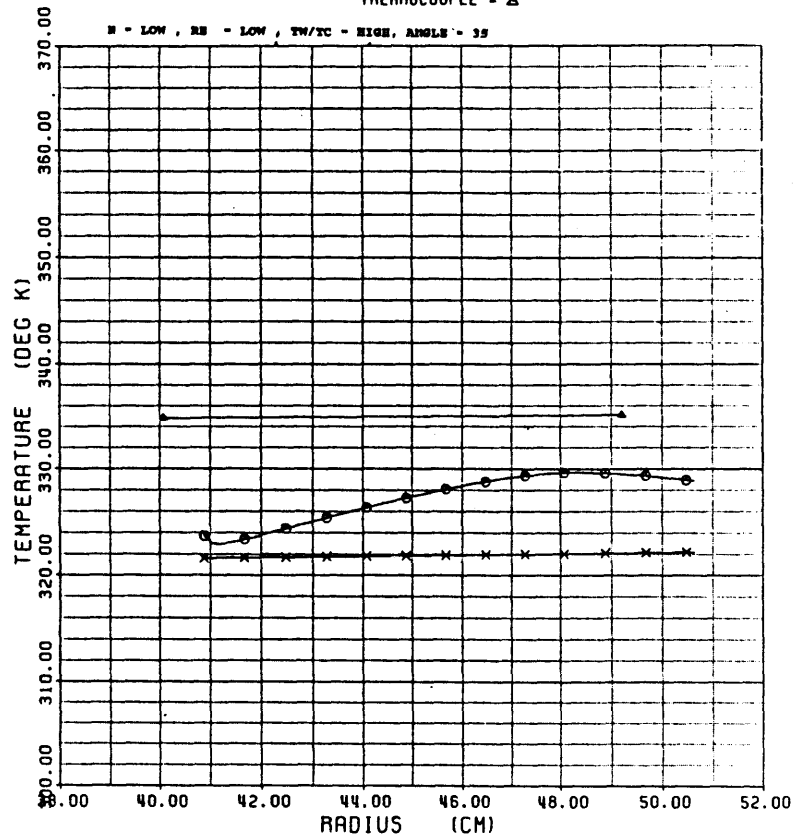


Figure 7C

### AVERAGE NUSSÉLT NUMBER

TEST #: 42

SYMBOLS: NU NO BASED ON LOCAL GAS TEMP -  $\circ$   
 NU NO BASED ON COOLANT TEMP -  $\times$   
 CHUPP'S CORRELATION -  $\triangle$   
 MORRIS' CORRELATION -  $\square$

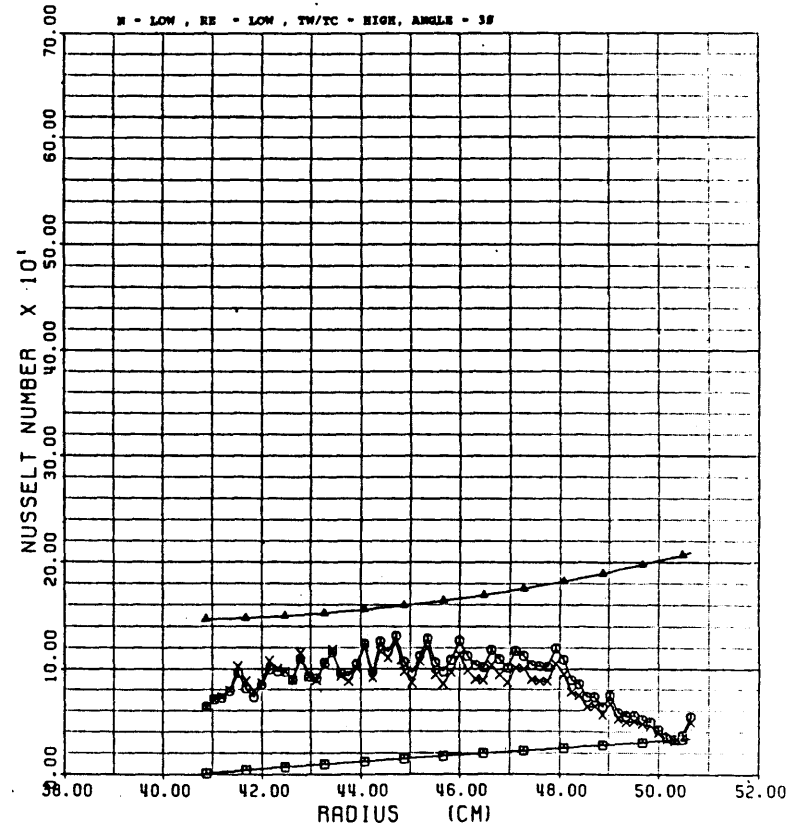


Figure 7D

### VELOCITY VS RADIUS

TEST #: 39

SYMBOLS: IMPINGEMENT = ○  
SUPPLY = X

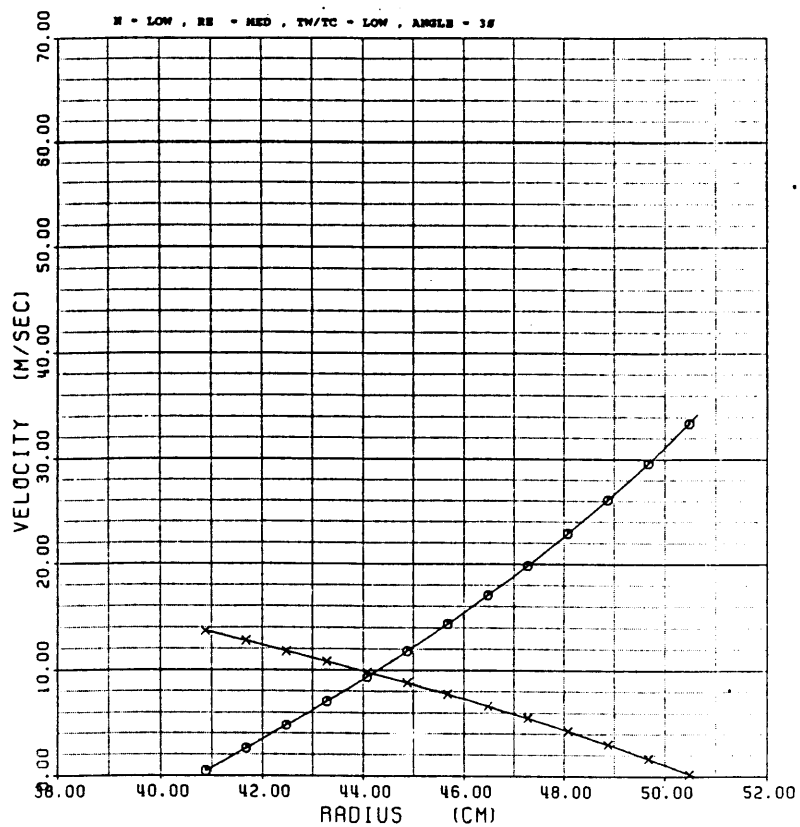


Figure 8A

### PRESSURE VS RADIUS

TEST #: 39

SYMBOLS: IMPINGEMENT = ○  
SUPPLY = X

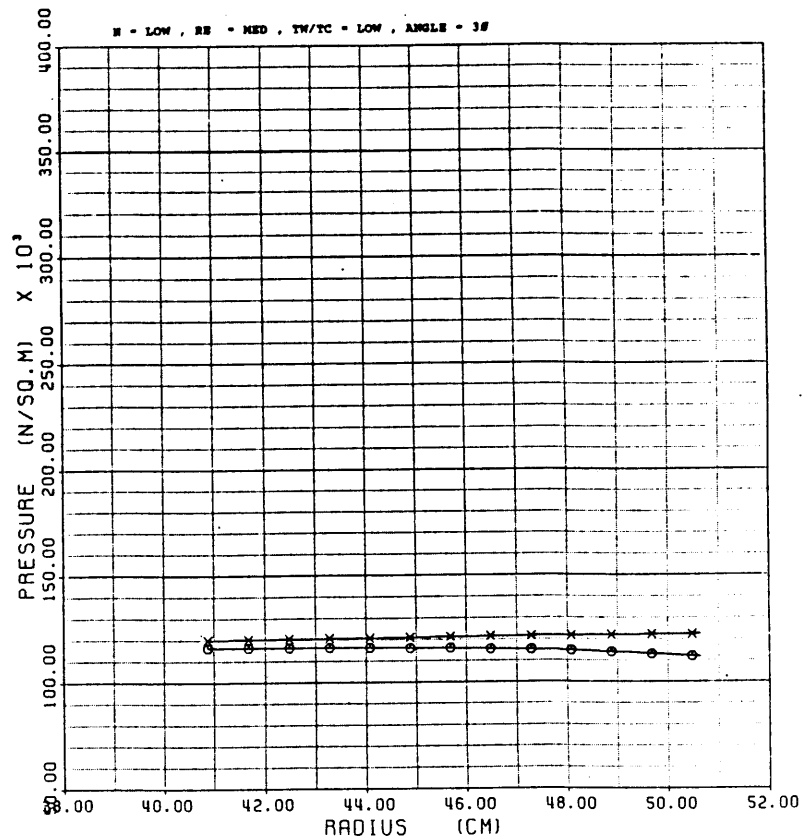


Figure 8B

### TEMPERATURE VS RADIUS

TEST #: 39

SYMBOLS: IMPINGEMENT - ○  
 SUPPLY - ×  
 THERMOCOUPLE - ▲

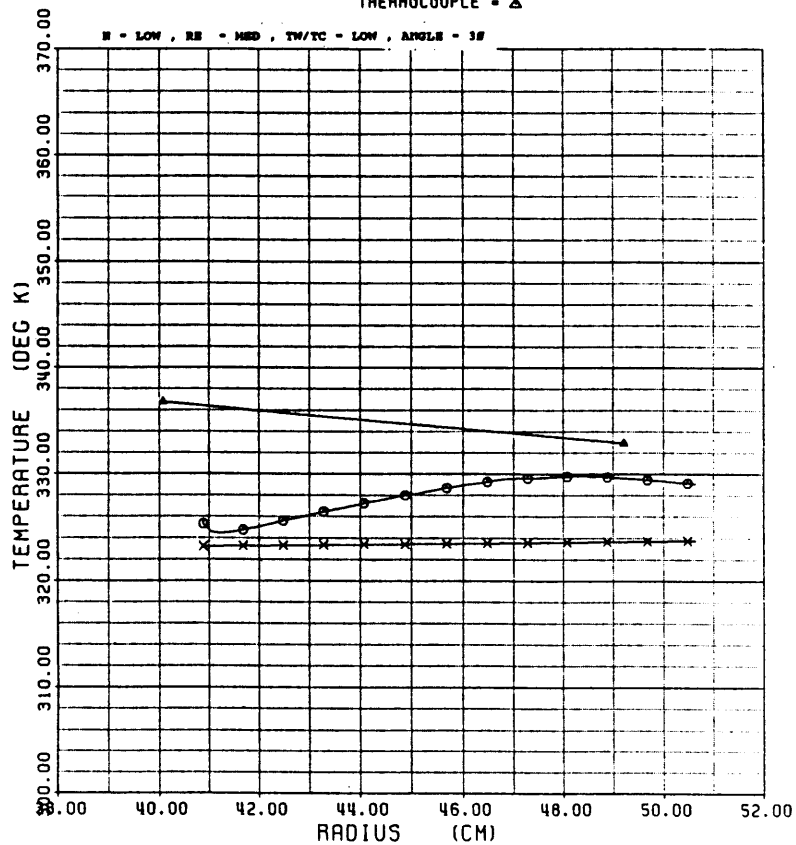


Figure 8C

### AVERAGE NUSSELT NUMBER

TEST #: 39

SYMBOLS: NU NO BASED ON LOCAL GAS TEMP - ○  
 NU NO BASED ON COOLANT TEMP - ×  
 CHUPP'S CORRELATION - ▲  
 MORRIS' CORRELATION - □

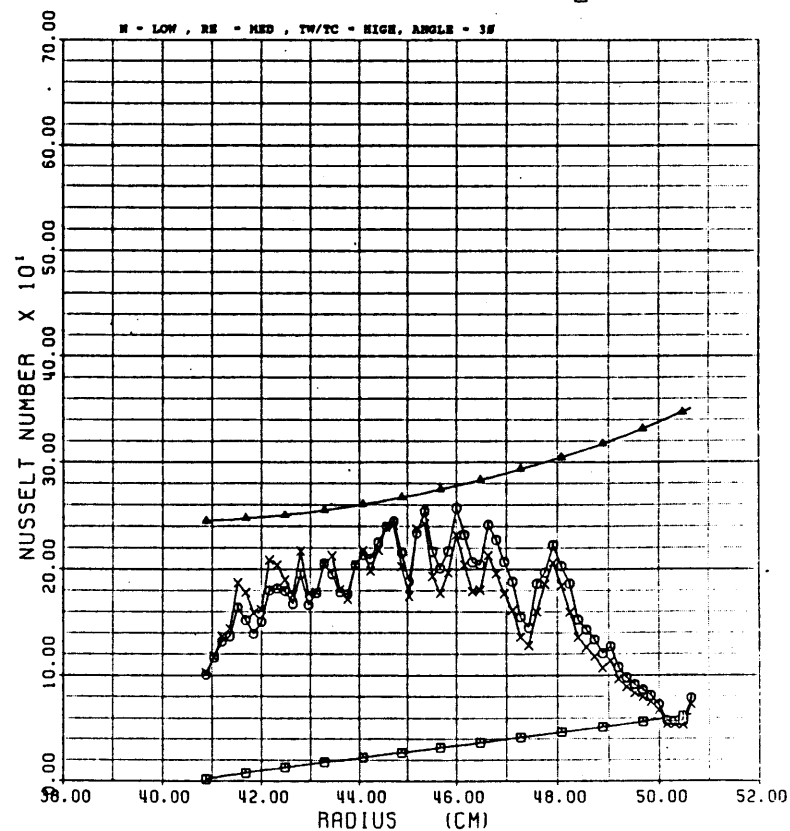


Figure 8D

### VELOCITY VS RADIUS

TEST #: 44

SYMBOLS: IMPINGEMENT = ○  
SUPPLY = X

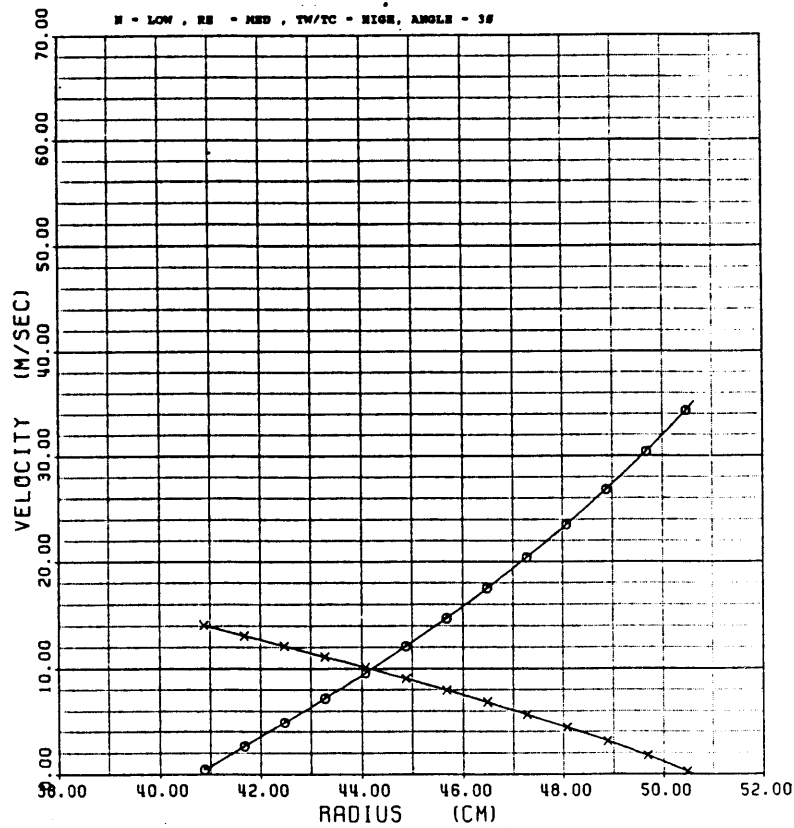


Figure 9A

### PRESSURE VS RADIUS

TEST #: 44

SYMBOLS: IMPINGEMENT = ○  
SUPPLY = X

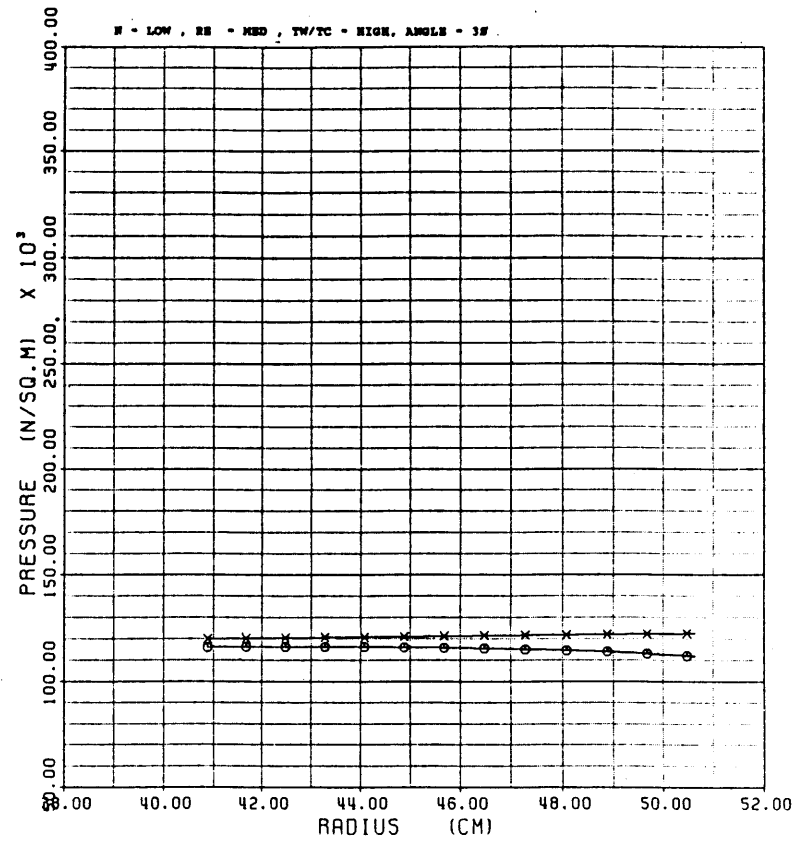


Figure 9B

### TEMPERATURE VS RADIUS

TEST #: 44

SYMBOLS: IMPINGEMENT - ○  
 SUPPLY - ×  
 THERMOCOUPLE - ▲

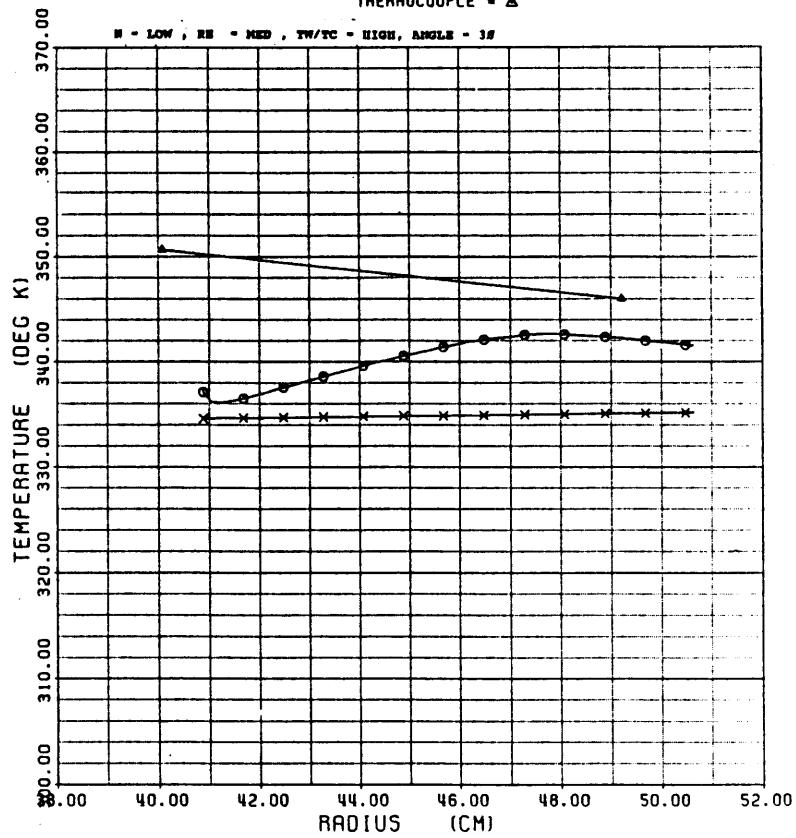


Figure 9C

### AVERAGE NUSSELT NUMBER

TEST #: 44

SYMBOLS: NU NO BASED ON LOCAL GAS TEMP - ○  
 NU NO BASED ON COOLANT TEMP - ×  
 CHUPP'S CORRELATION - ▲  
 MORRIS' CORRELATION - □

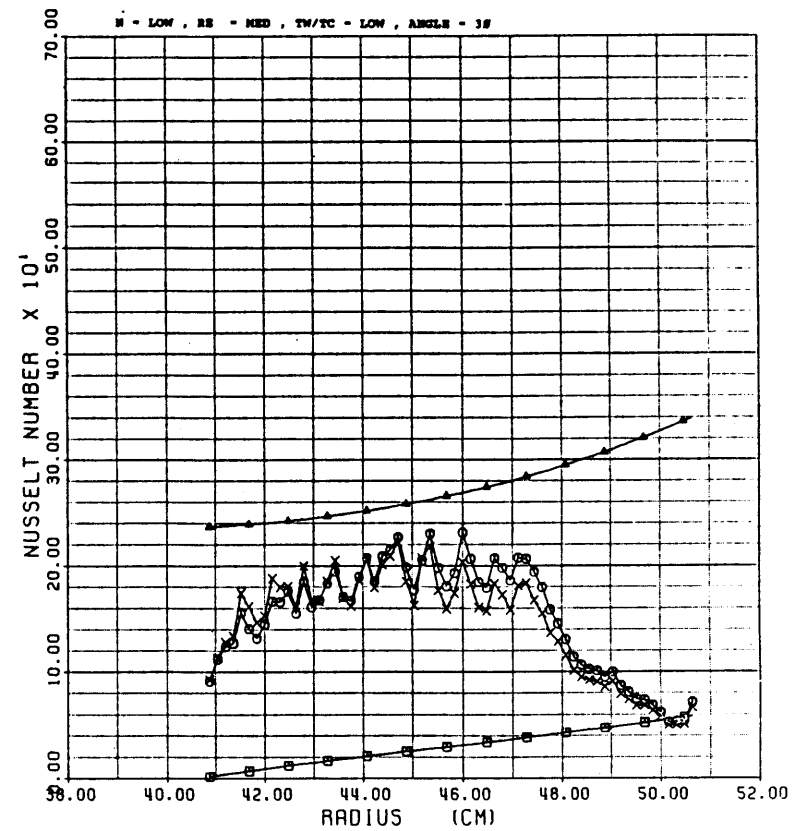


Figure 9D

VELOCITY VS RADIUS

TEST #: 40

SYMBOLS: IMPINGEMENT - ○  
SUPPLY - X

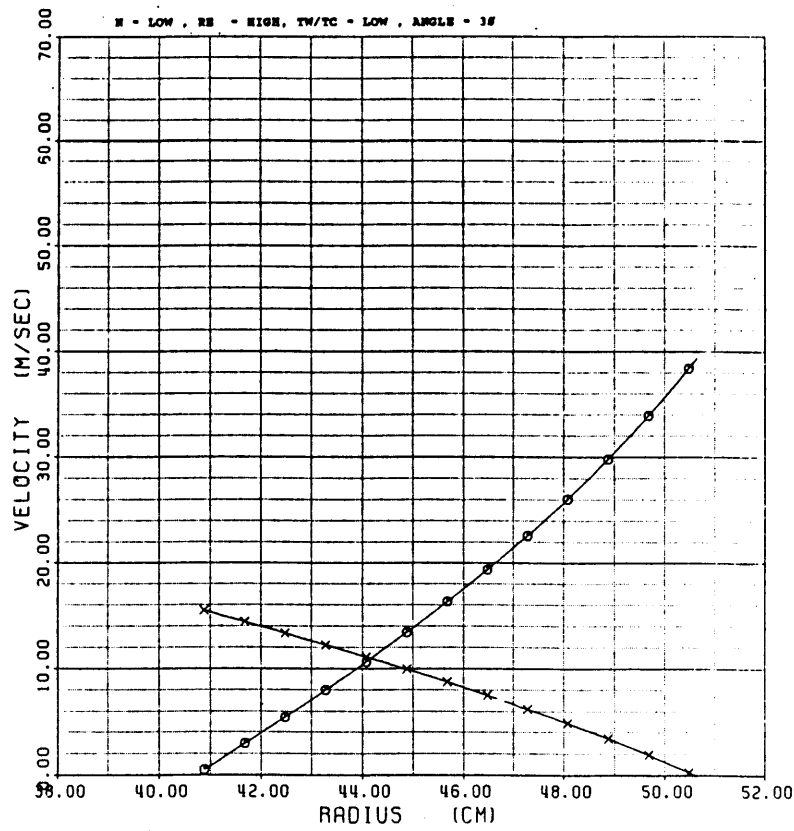


Figure 10A

PRESSURE VS RADIUS

TEST #: 40

SYMBOLS: IMPINGEMENT - ○  
SUPPLY - X

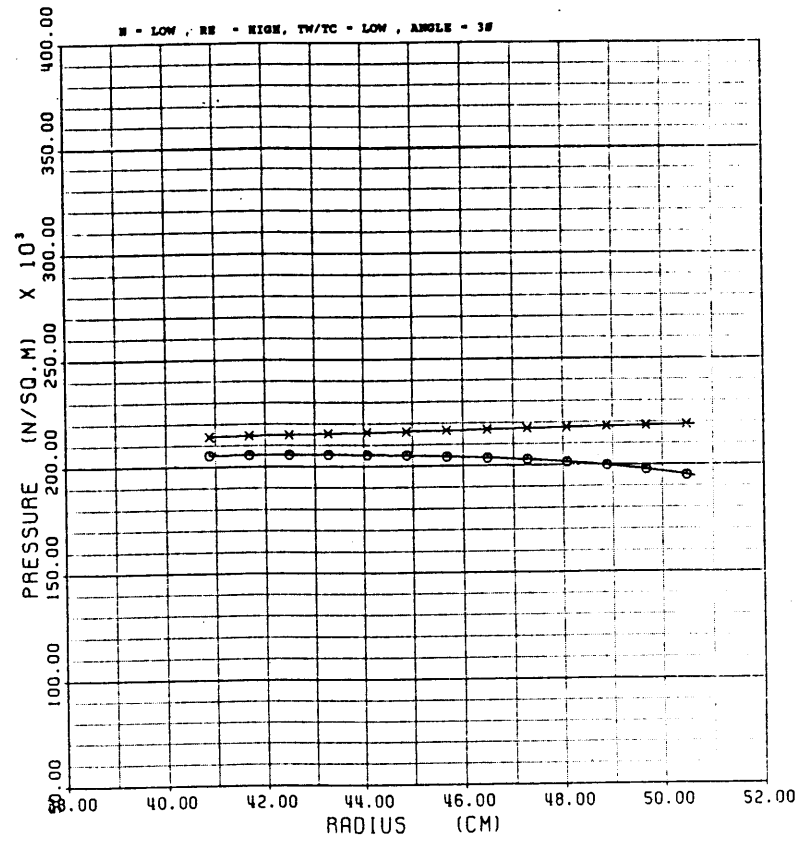


Figure 10B

### TEMPERATURE VS RADIUS

TEST #: 40

SYMBOLS: IMPINGEMENT -  $\circ$   
 SUPPLY -  $\times$   
 THERMOCOUPLE -  $\triangle$

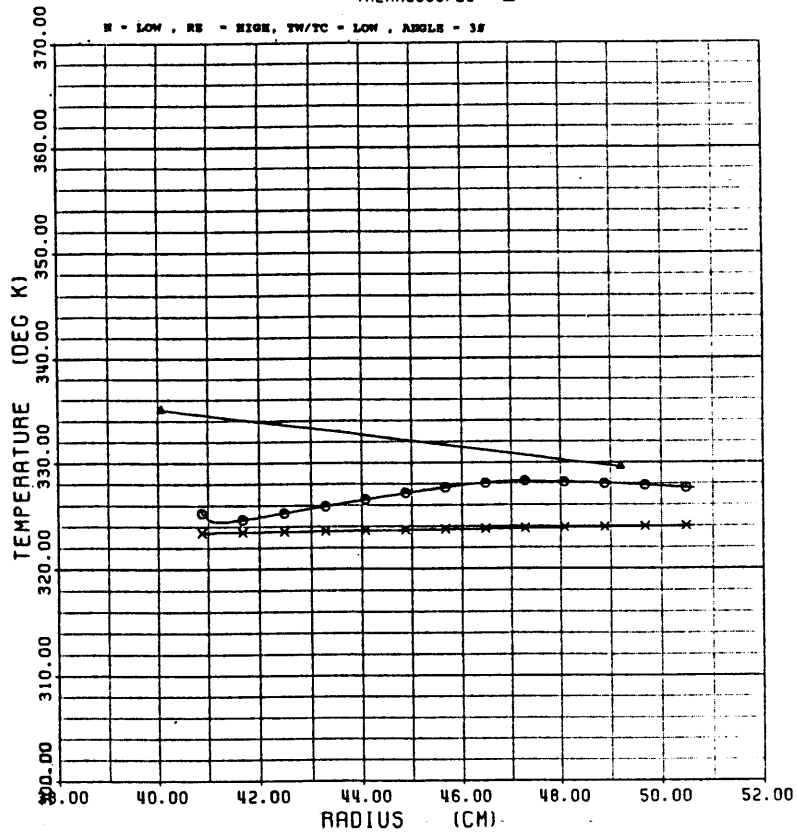


Figure 10C

### AVERAGE NUSSELT NUMBER

TEST #: 40

SYMBOLS: NU NO BASED ON LOCAL GAS TEMP -  $\circ$   
 NU NO BASED ON COOLANT TEMP -  $\times$   
 CHUPP'S CORRELATION -  $\triangle$   
 MORRIS' CORRELATION -  $\square$

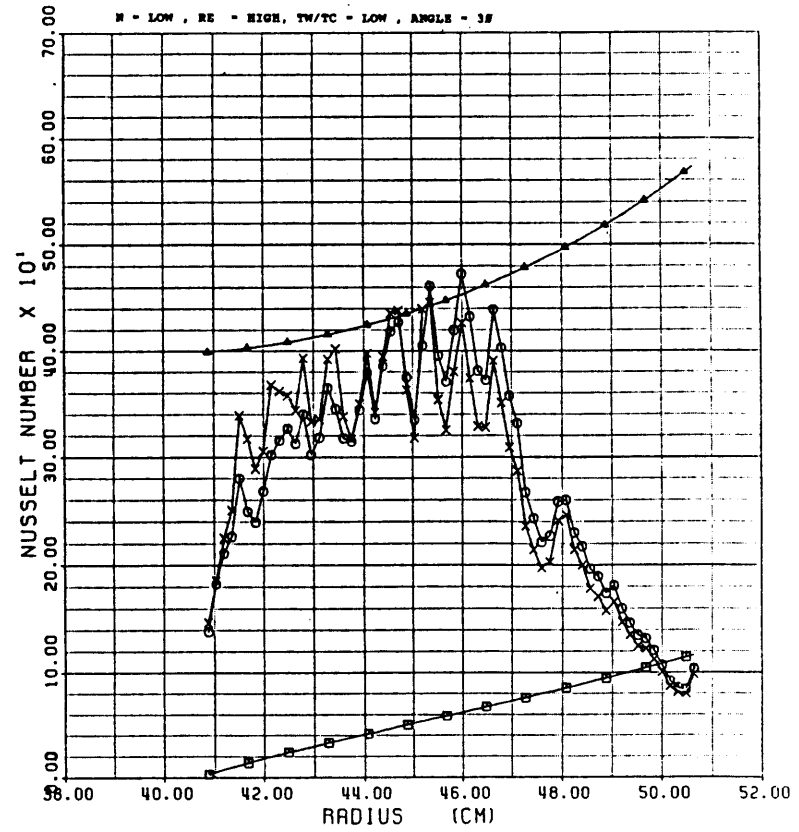


Figure 10D

### VELOCITY VS RADIUS

TEST #: 41

SYMBOLS: IMPINGEMENT - ○  
SUPPLY - ×

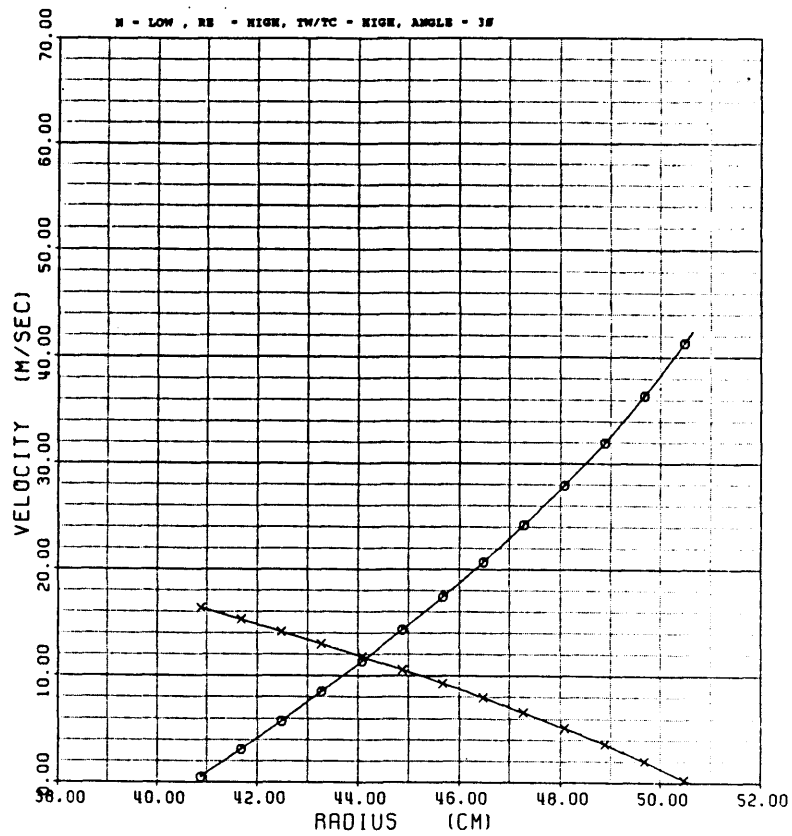


Figure 11A

### PRESSURE VS RADIUS

TEST #: 41

SYMBOLS: IMPINGEMENT - ○  
SUPPLY - ×

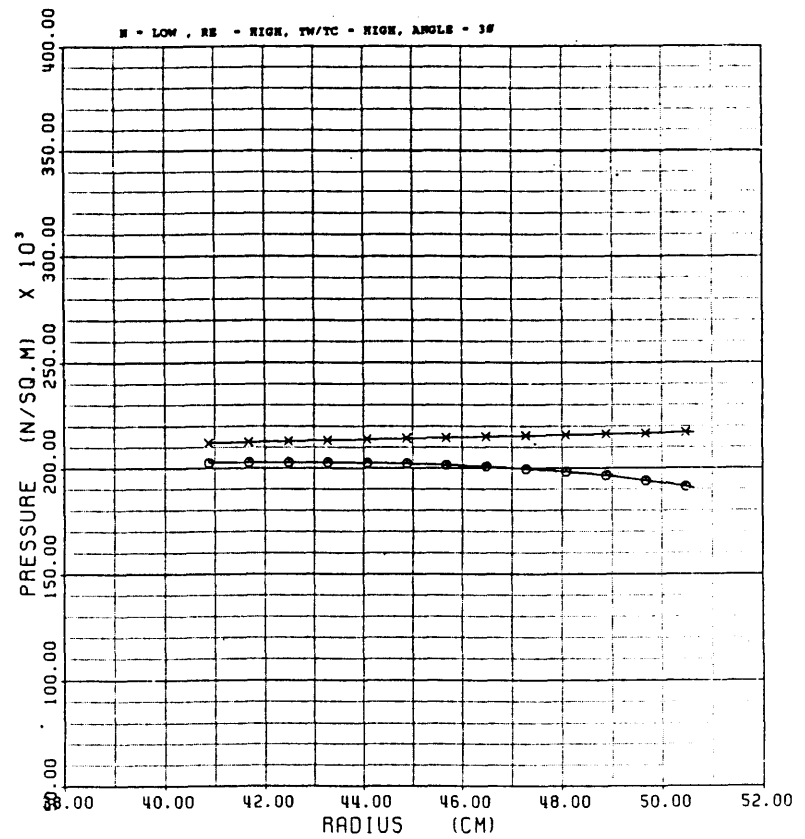


Figure 11B

### TEMPERATURE VS RADIUS

TEST #: 41

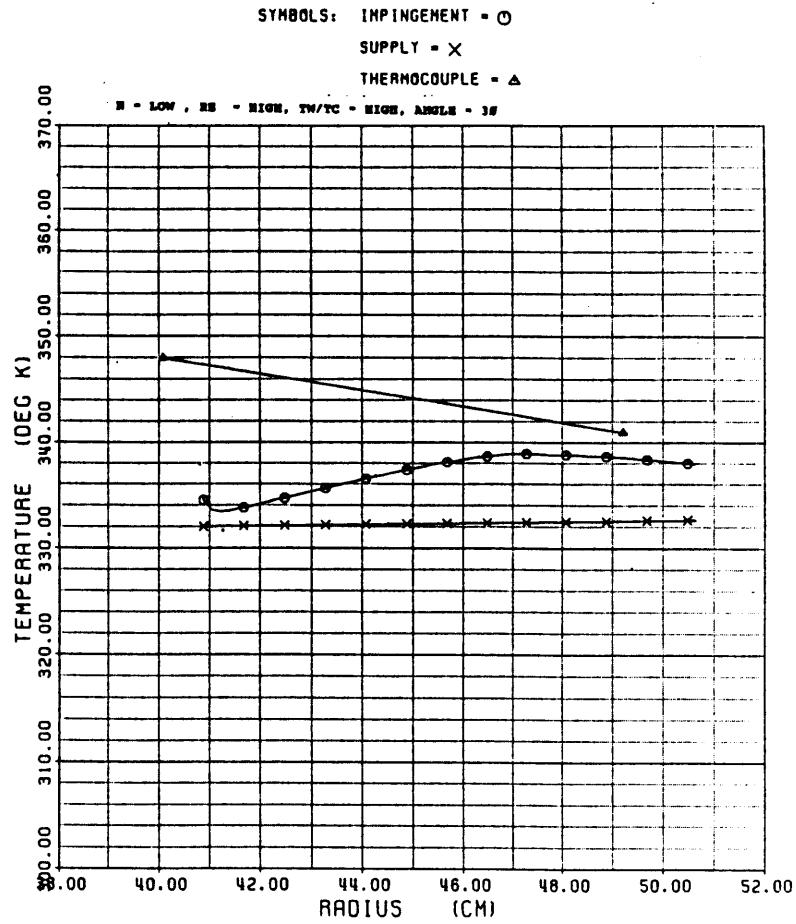


Figure 11C

### AVERAGE NUSSELT NUMBER

TEST #: 41

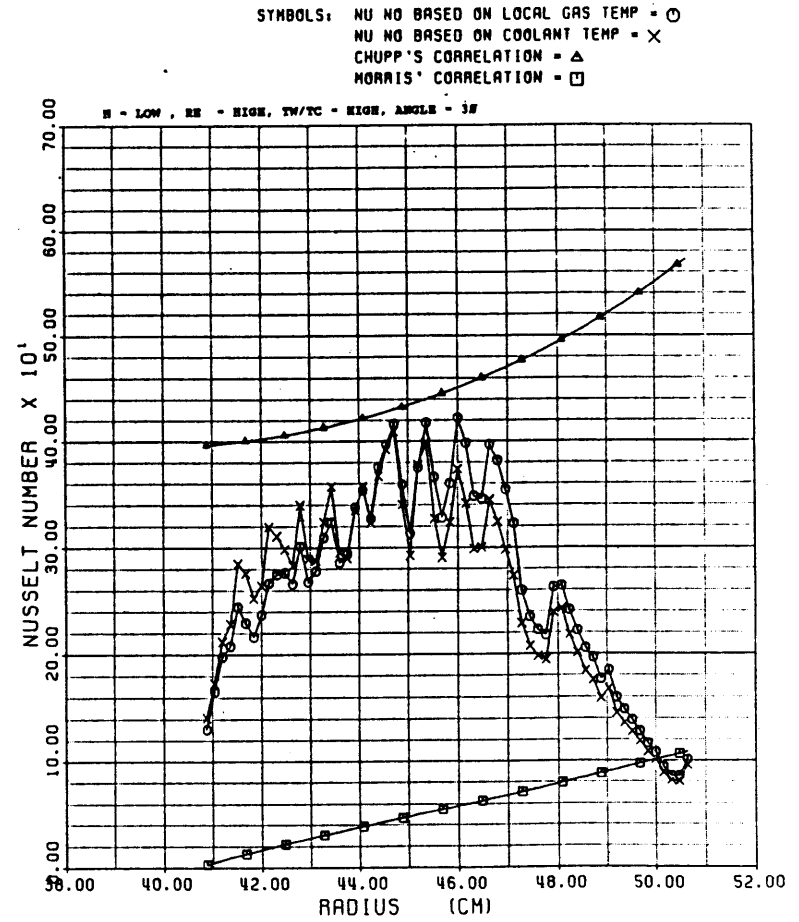


Figure 11D

### VELOCITY VS RADIUS

TEST #: 57

SYMBOLS: IMPINGEMENT = ○  
SUPPLY = ×

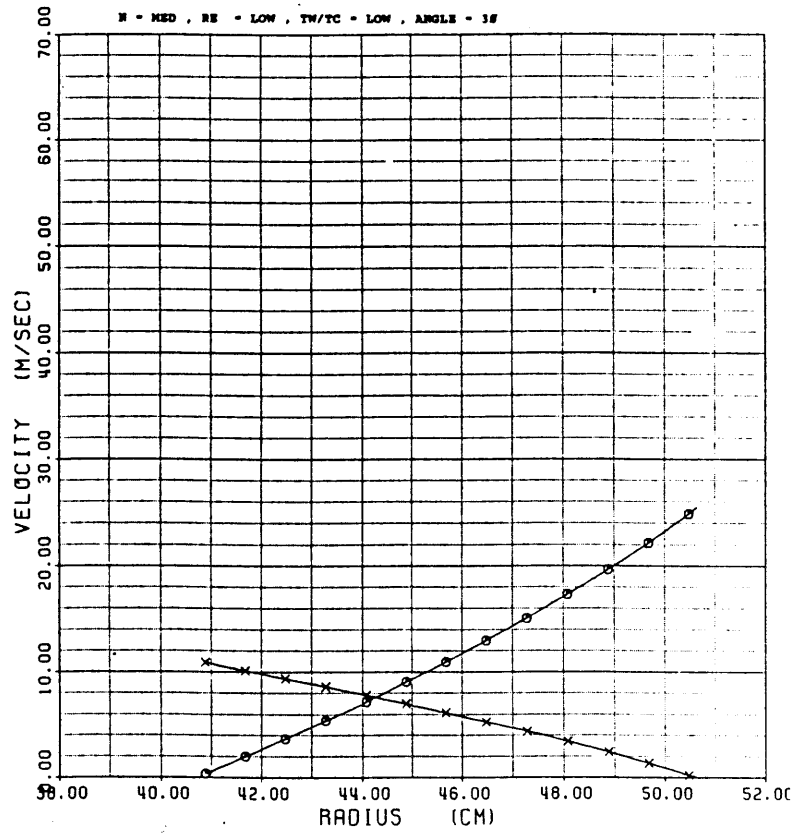


Figure 12A

### PRESSURE VS RADIUS

TEST #: 57

SYMBOLS: IMPINGEMENT = ○  
SUPPLY = ×

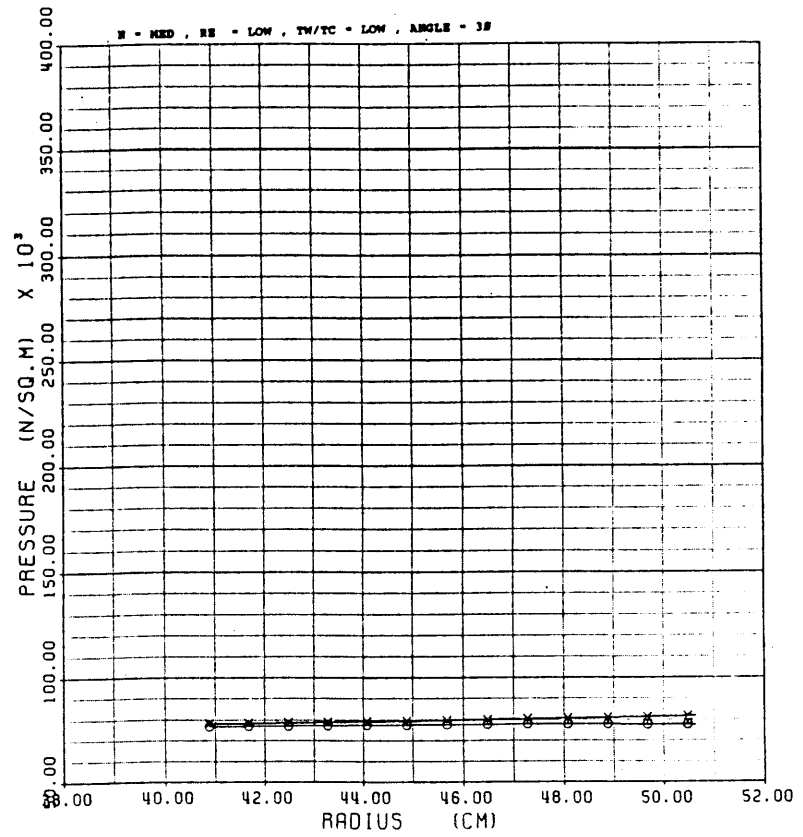


Figure 12B

### TEMPERATURE VS RADIUS

TEST #: 57

SYMBOLS: IMPINGEMENT =  $\circ$   
 SUPPLY = X  
 THERMOCOUPLE =  $\Delta$

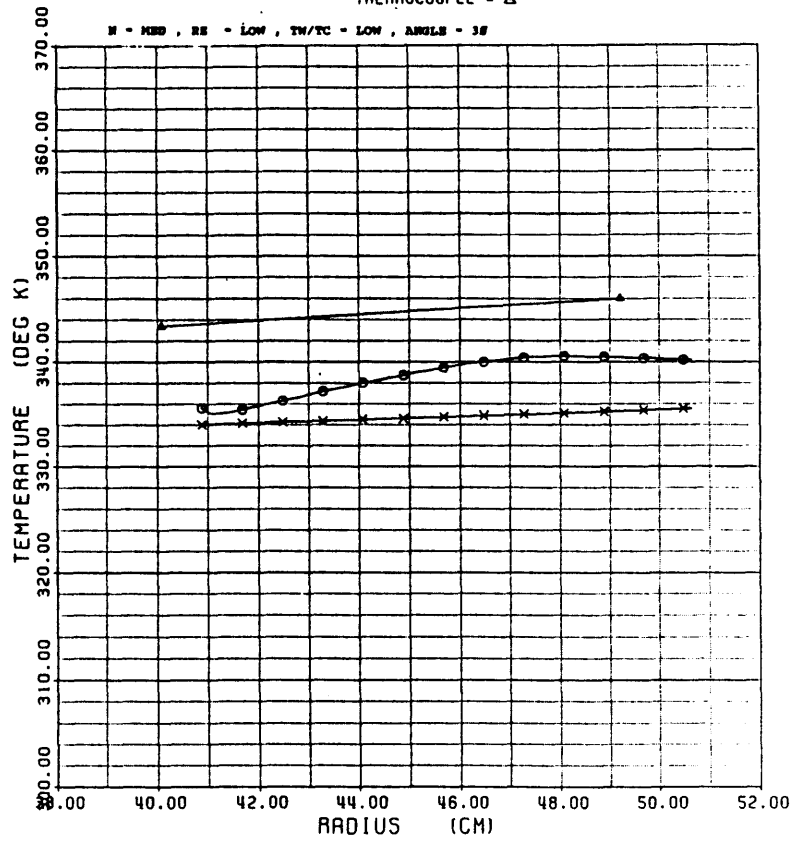


Figure 12C

### AVERAGE NUSSELT NUMBER

TEST #: 57

SYMBOLS: NU NO BASED ON LOCAL GAS TEMP =  $\circ$   
 NU NO BASED ON COOLANT TEMP = X  
 CHUPP'S CORRELATION =  $\Delta$   
 MORRIS' CORRELATION =  $\square$

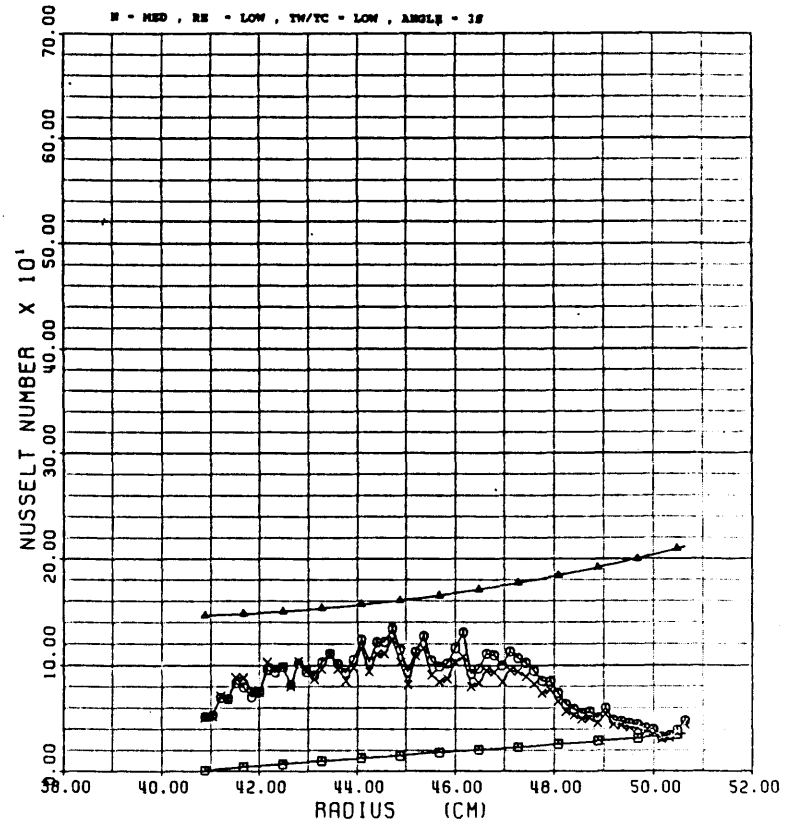


Figure 12D

### VELOCITY VS RADIUS

TEST #: 56

SYMBOLS: IMPINGEMENT - ○  
SUPPLY - X

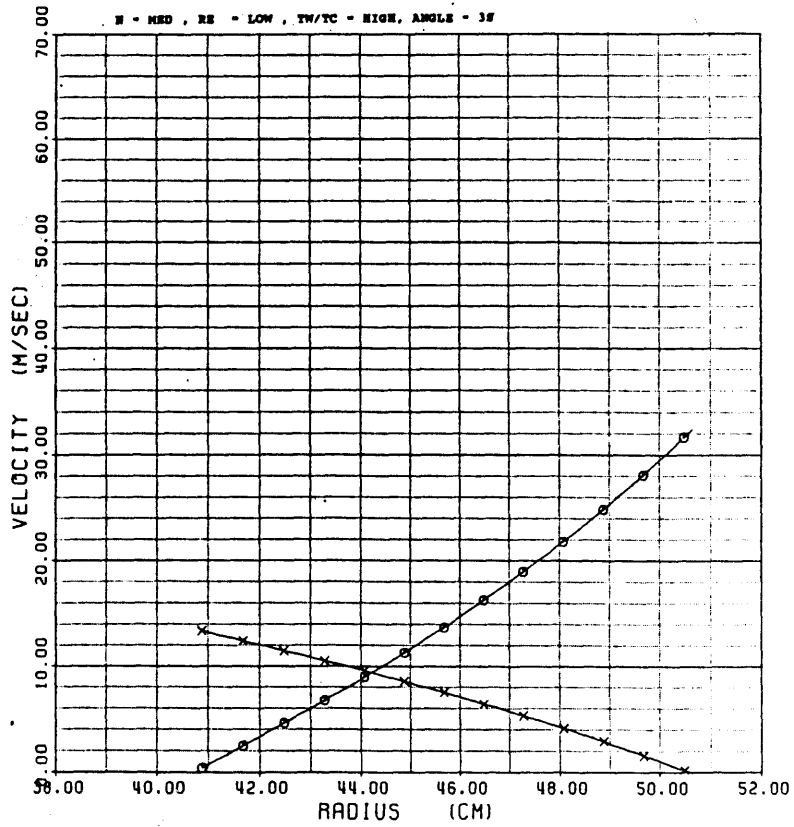


Figure 13A

### PRESSURE VS RADIUS

TEST #: 56

SYMBOLS: IMPINGEMENT - ○  
SUPPLY - X

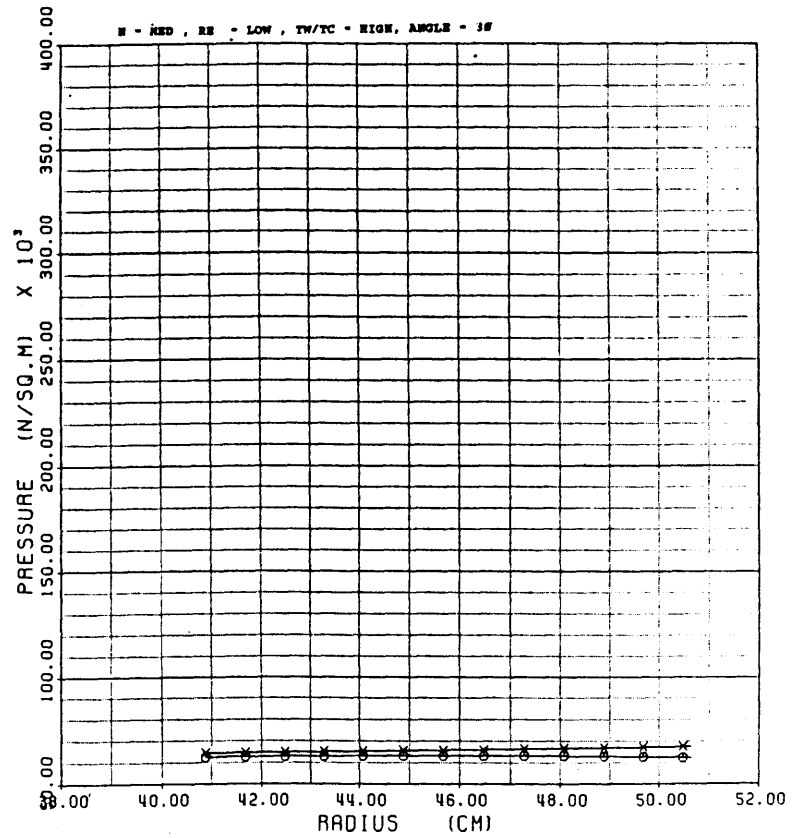


Figure 13B

TEMPERATURE VS RADIUS

TEST #: 56

SYMBOLS: IMPINGEMENT -  $\circ$   
 SUPPLY -  $\times$   
 THERMOCOUPLE -  $\Delta$

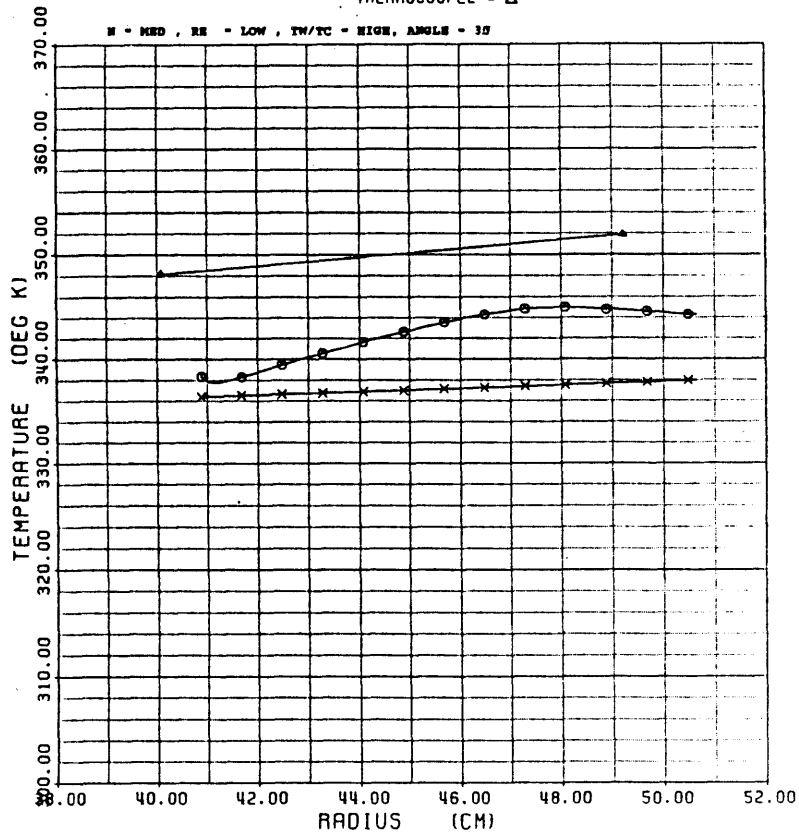


Figure 13C

AVERAGE NUSSELT NUMBER

TEST #: 56

SYMBOLS: NU NO BASED ON LOCAL GAS TEMP -  $\circ$   
 NU NO BASED ON COOLANT TEMP -  $\times$   
 CHUPP'S CORRELATION -  $\Delta$   
 MORRIS' CORRELATION -  $\square$

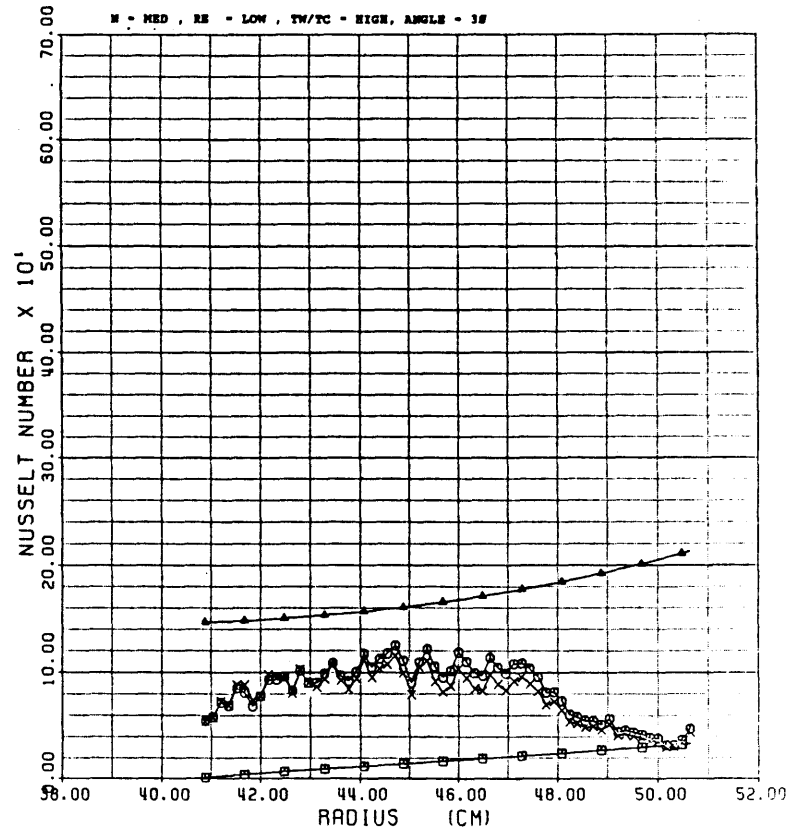


Figure 13D

### VELOCITY VS RADIUS

TEST #: 55

SYMBOLS: IMPINGEMENT - ○  
SUPPLY - X

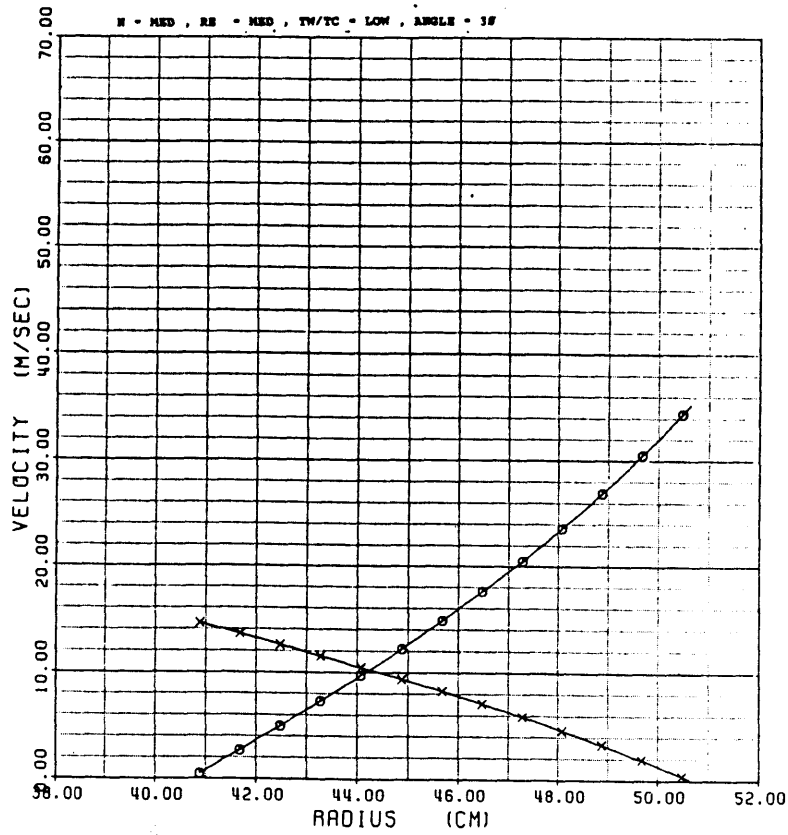


Figure 14A

### PRESSURE VS RADIUS

TEST #: 55

SYMBOLS: IMPINGEMENT - ○  
SUPPLY - X

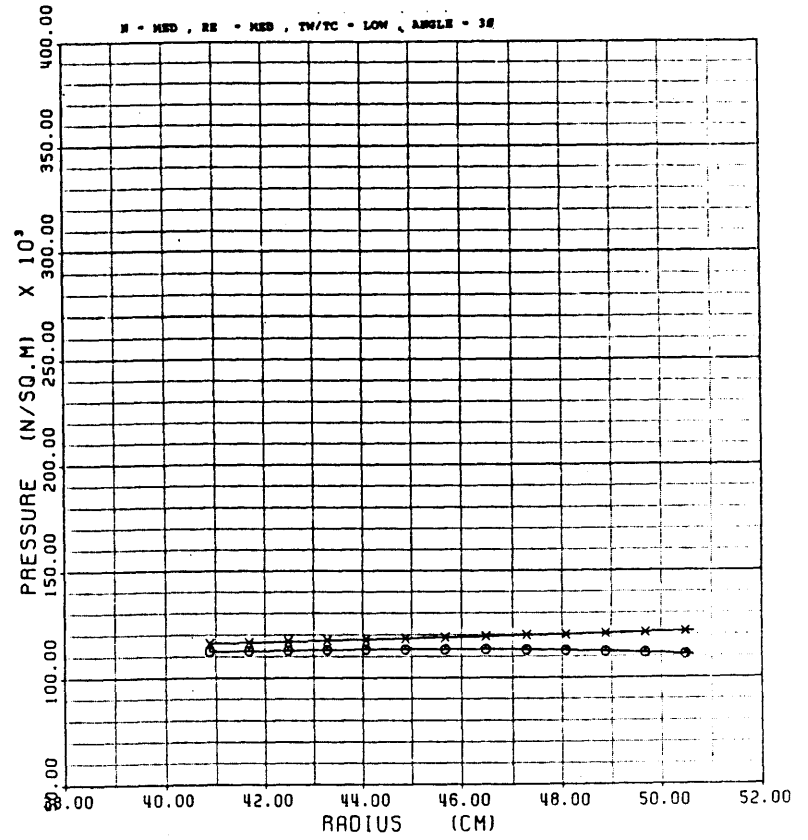


Figure 14B

TEMPERATURE VS RADIUS

TEST #: 55

SYMBOLS: IMPINGEMENT -  $\circ$   
 SUPPLY -  $\times$   
 THERMOCOUPLE -  $\triangle$

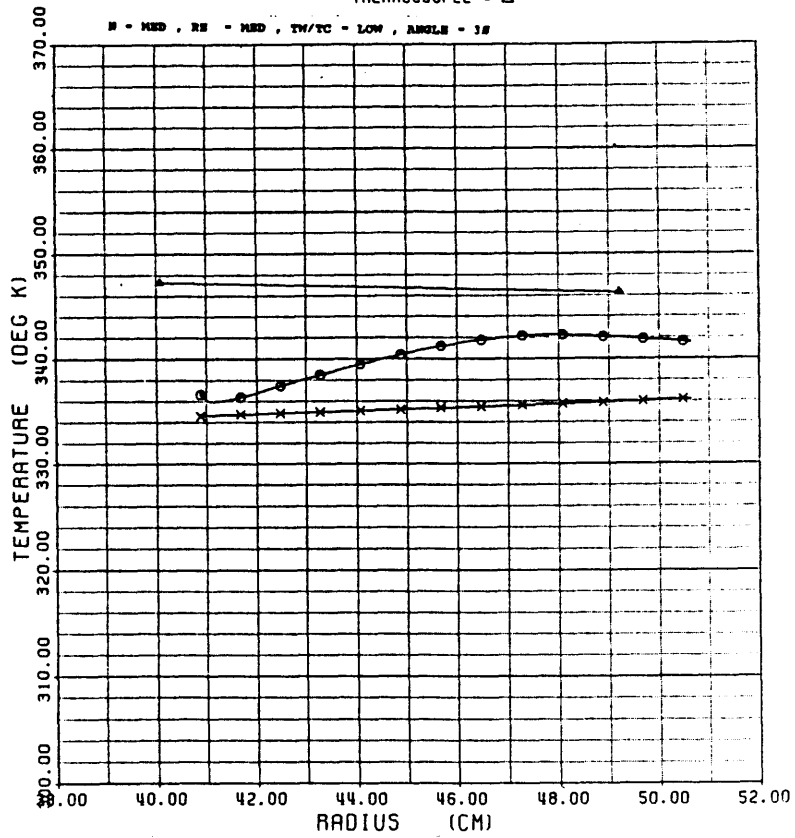


Figure 14C

AVERAGE NUSSELT NUMBER

TEST #: 55

SYMBOLS: NU NO BASED ON LOCAL GAS TEMP -  $\circ$   
 NU NO BASED ON COOLANT TEMP -  $\times$   
 CHUPP'S CORRELATION -  $\triangle$   
 MORRIS' CORRELATION -  $\square$

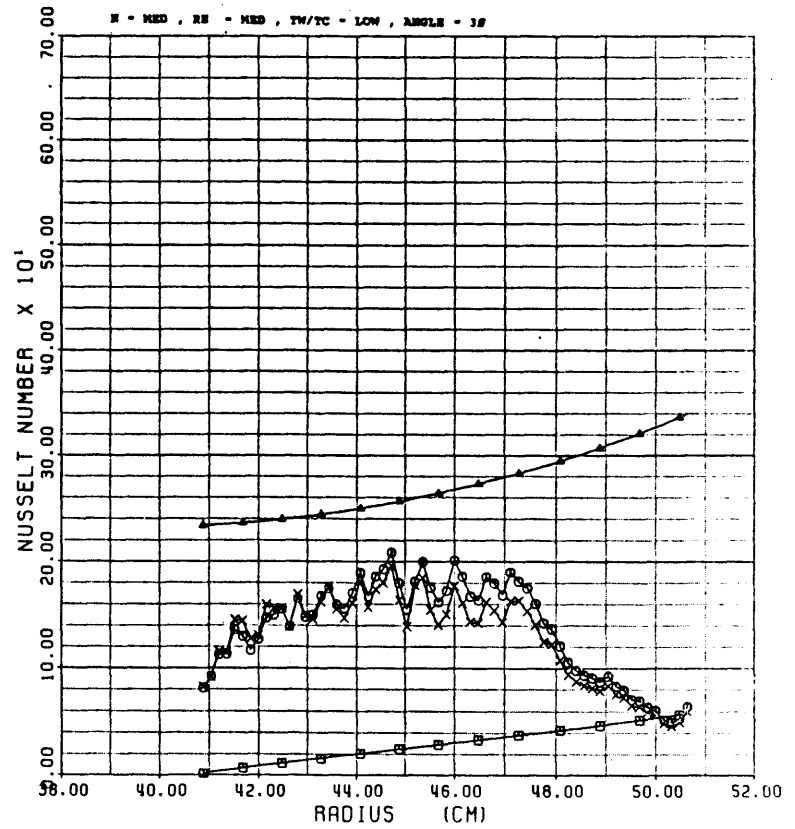


Figure 14D

### VELOCITY VS RADIUS

TEST #: 54

SYMBOLS: IMPINGEMENT - ○  
SUPPLY - X

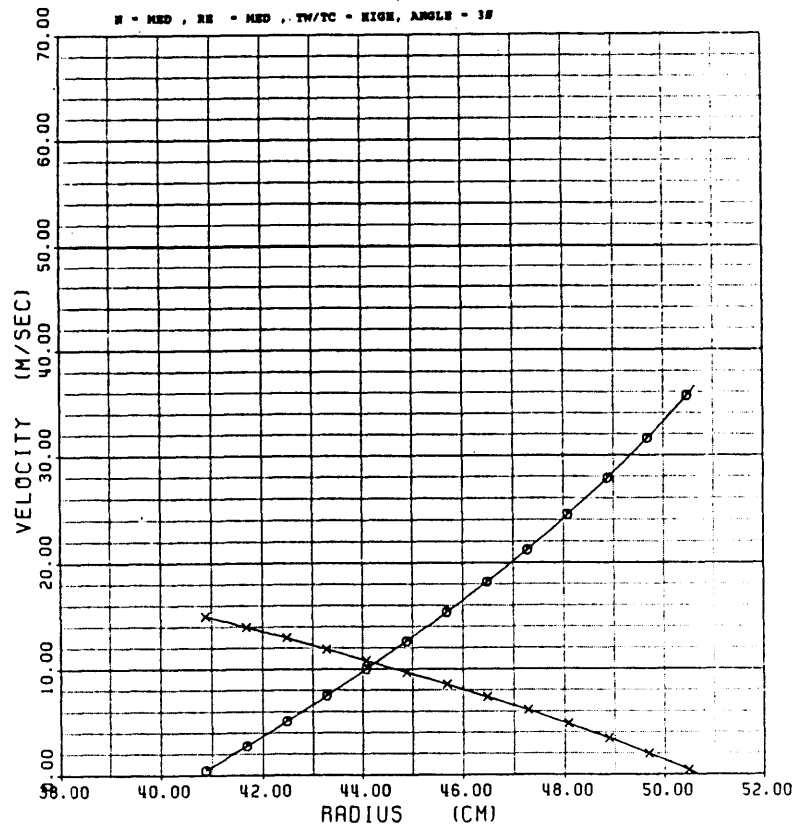


Figure 15A

### PRESSURE VS RADIUS

TEST #: 54

SYMBOLS: IMPINGEMENT - ○  
SUPPLY - X

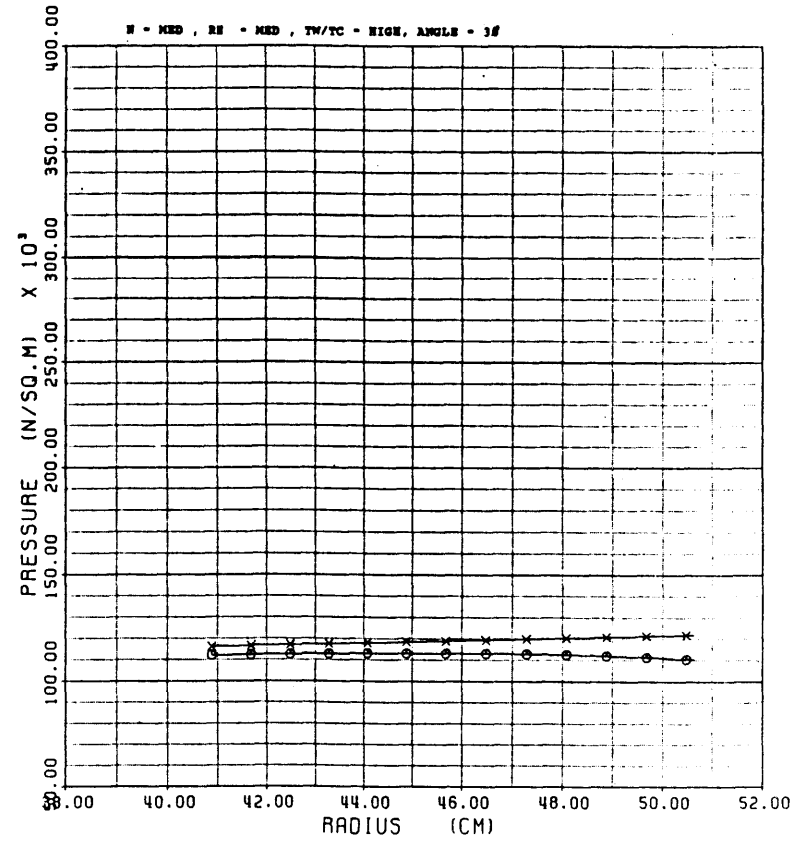


Figure 15B

### TEMPERATURE VS RADIUS

TEST #: 54

SYMBOLS: IMPINGEMENT - ○  
 SUPPLY - ×  
 THERMOCOUPLE - △

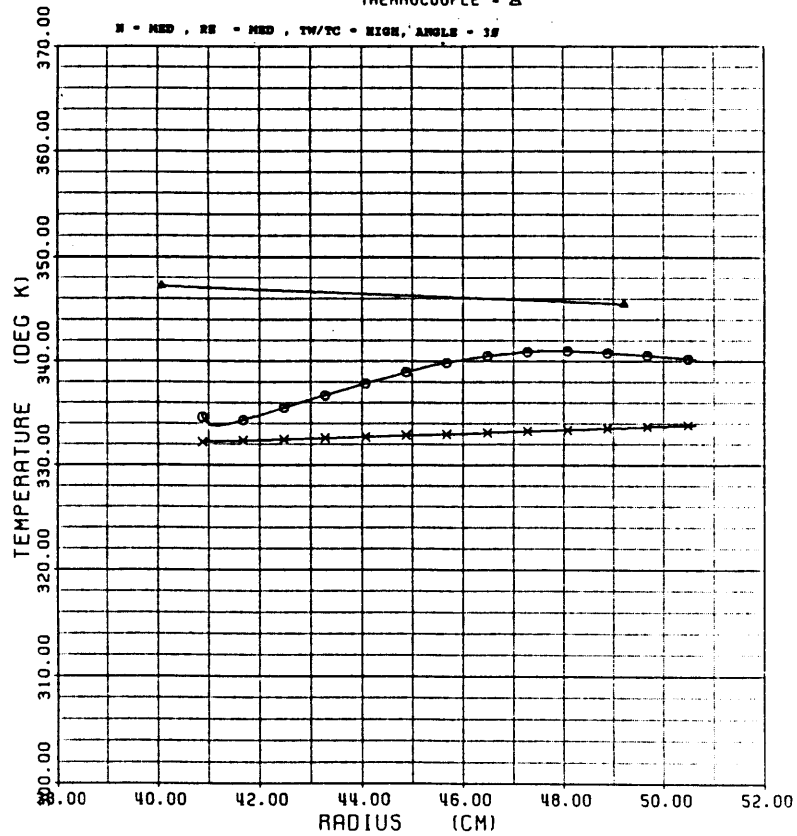


Figure 15C

### AVERAGE NUSSELT NUMBER

TEST #: 54

SYMBOLS: NU NO BASED ON LOCAL GAS TEMP - ○  
 NU NO BASED ON COOLANT TEMP - ×  
 CHUPP'S CORRELATION - △  
 MORRIS' CORRELATION - □

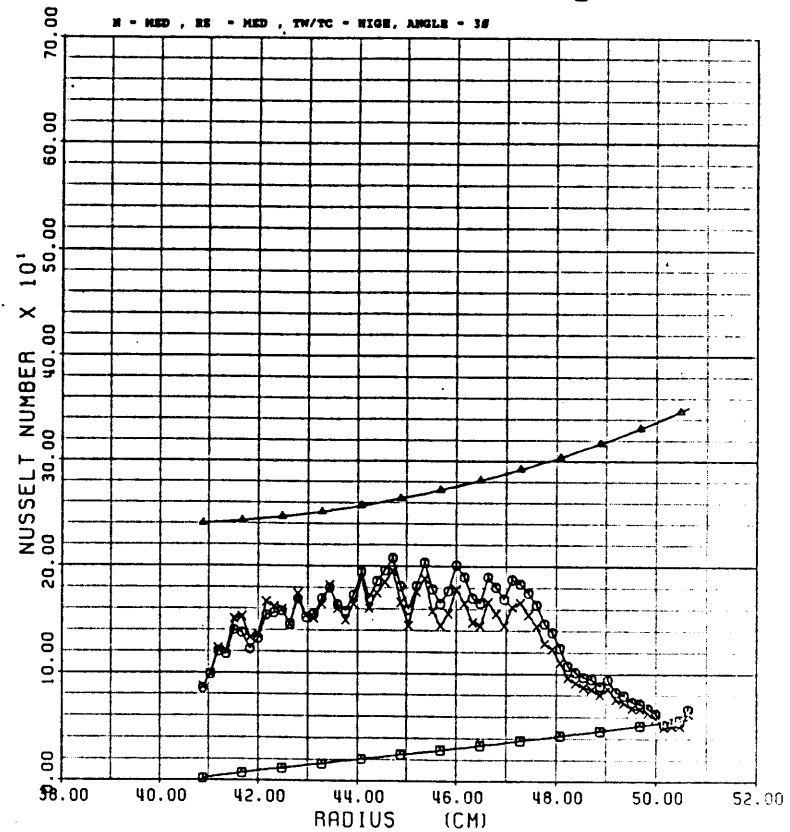


Figure 15D

### VELOCITY VS RADIUS

TEST #: 59

SYMBOLS: IMPINGEMENT = ○  
SUPPLY = X

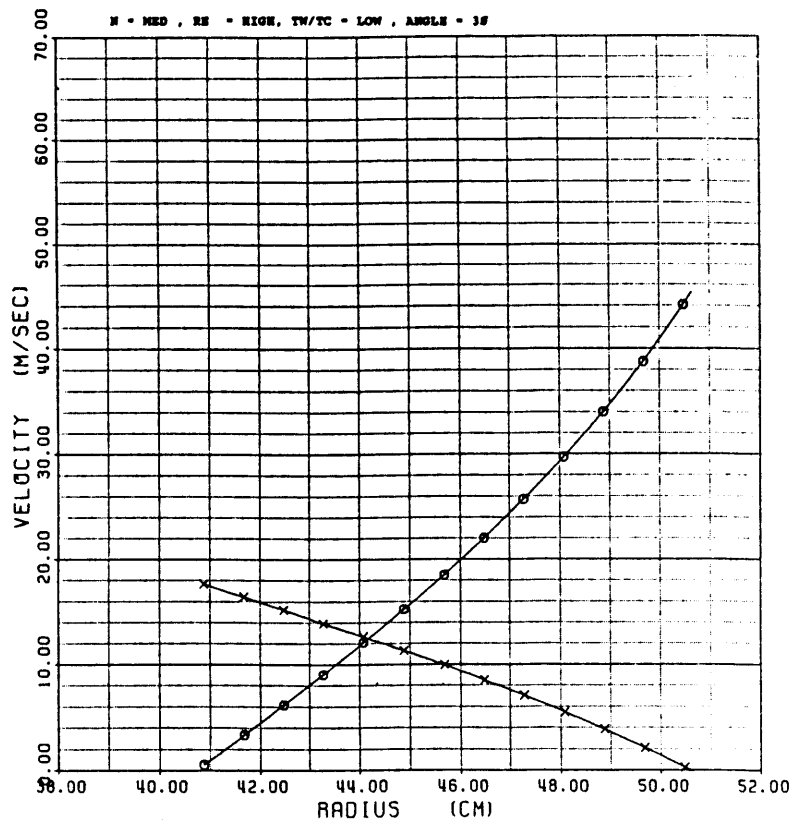


Figure 16A

### PRESSURE VS RADIUS

TEST #: 59

SYMBOLS: IMPINGEMENT = ○  
SUPPLY = X

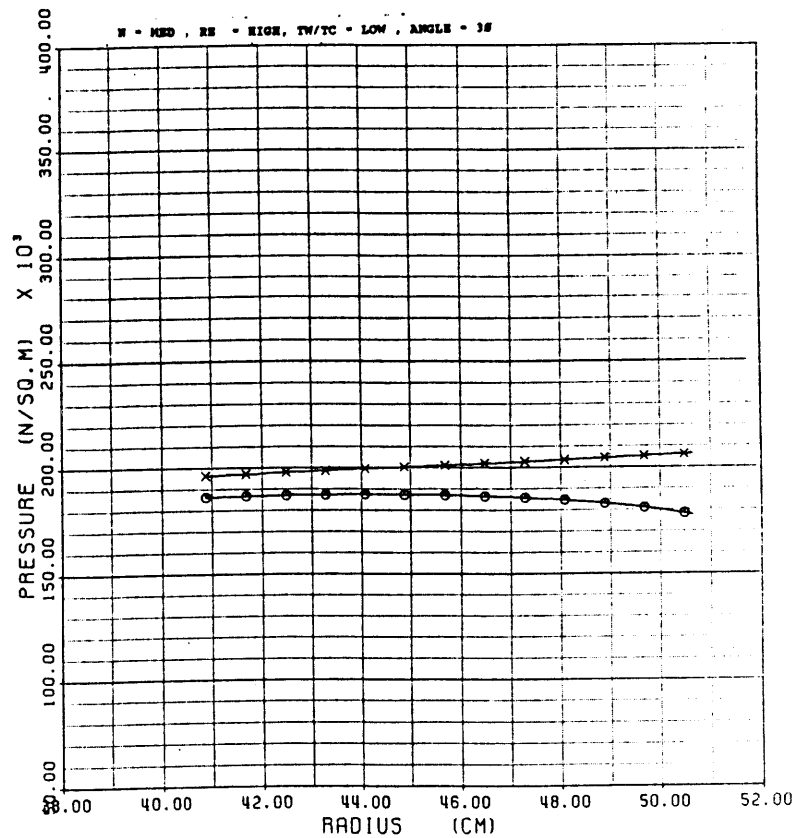


Figure 16B

TEMPERATURE VS RADIUS

TEST #: 59

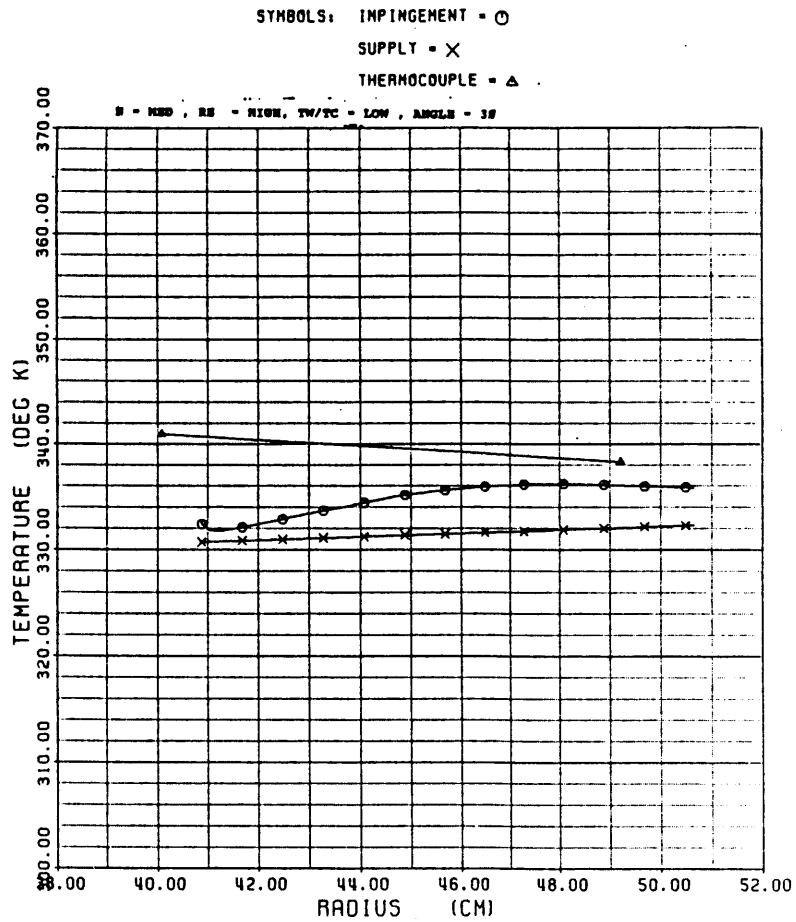


Figure 16C

AVERAGE NUSSELT NUMBER

TEST #: 59

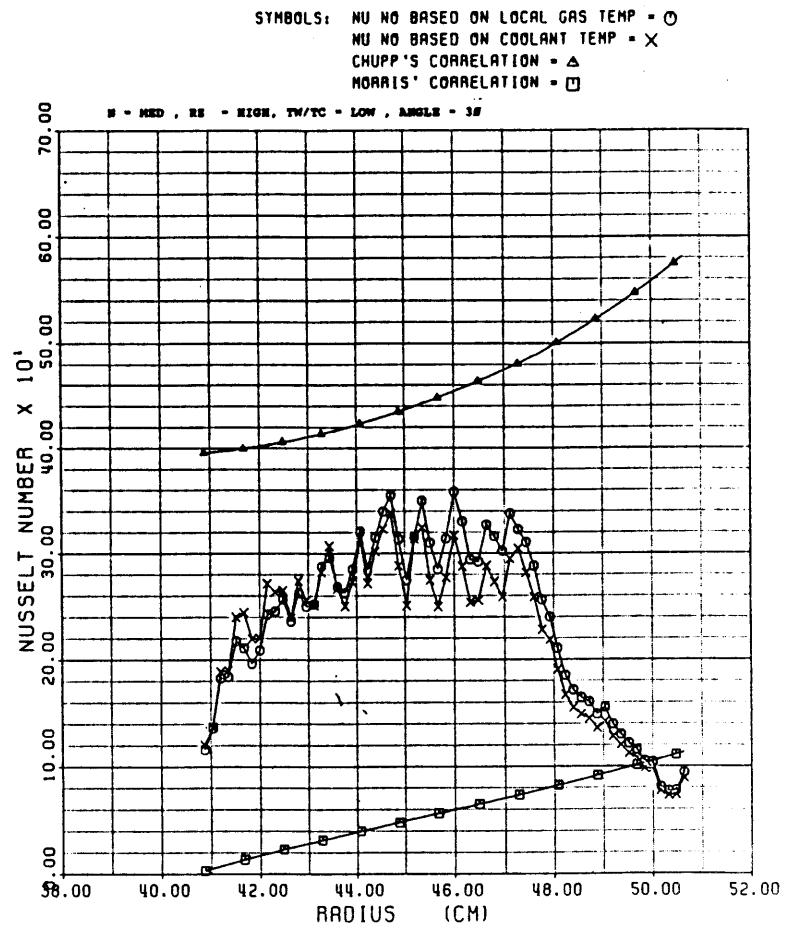


Figure 16D

# VELOCITY VS RADIUS

TEST #: 58

SYMBOLS: IMPINGEMENT - O  
SUPPLY - X

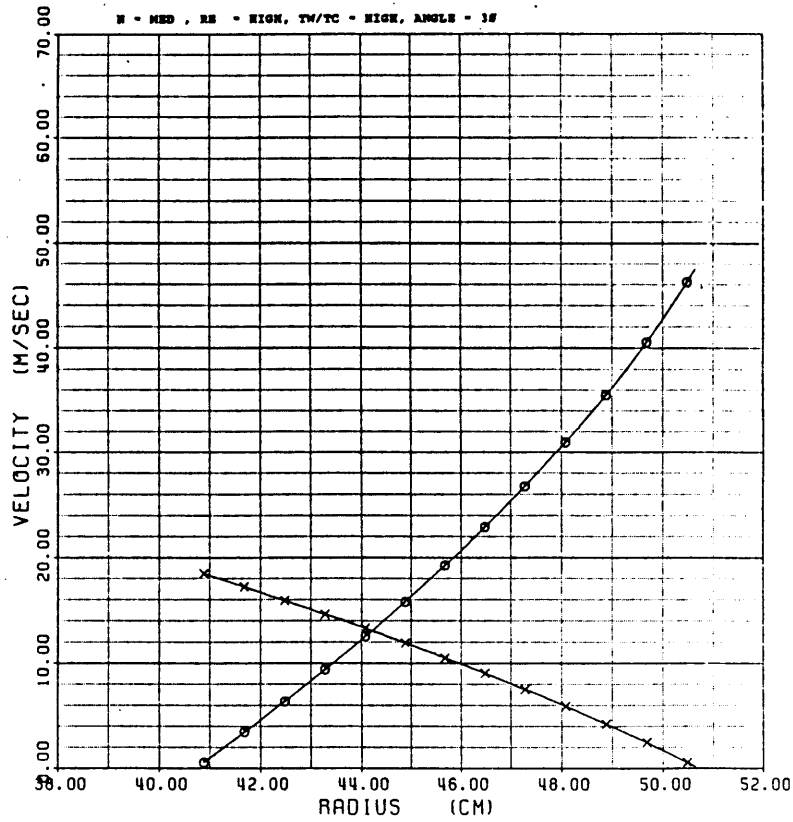


Figure 17A

# PRESSURE VS RADIUS

TEST #: 58

SYMBOLS: IMPINGEMENT - O  
SUPPLY - X

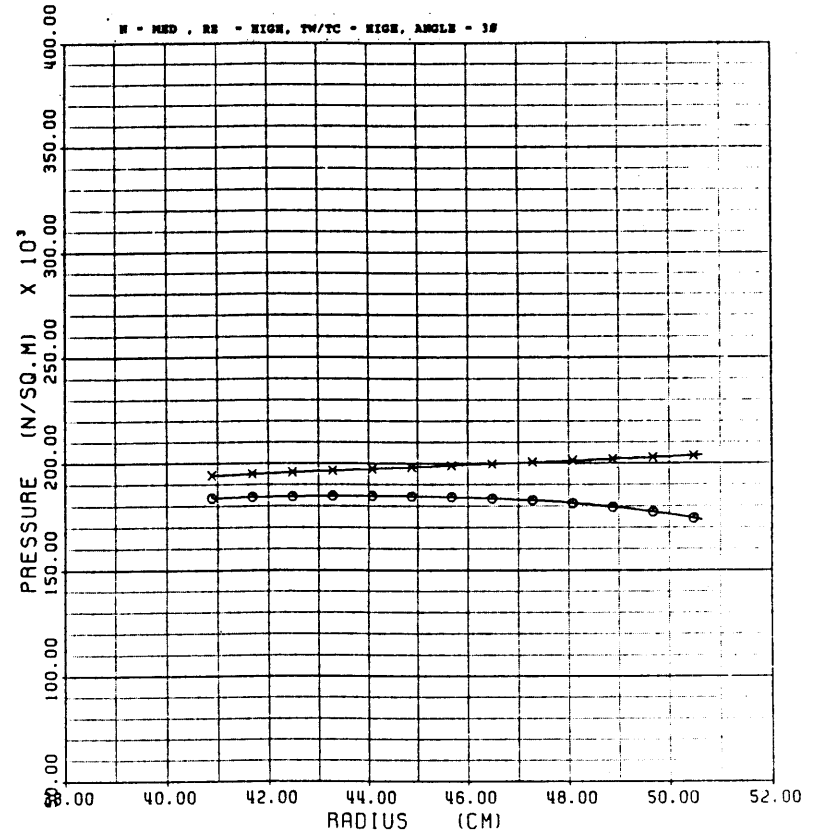


Figure 17B

# TEMPERATURE VS RADIUS

TEST #: 58

SYMBOLS: IMPINGEMENT =  $\circ$   
 SUPPLY =  $\times$   
 THERMOCOUPLE =  $\triangle$

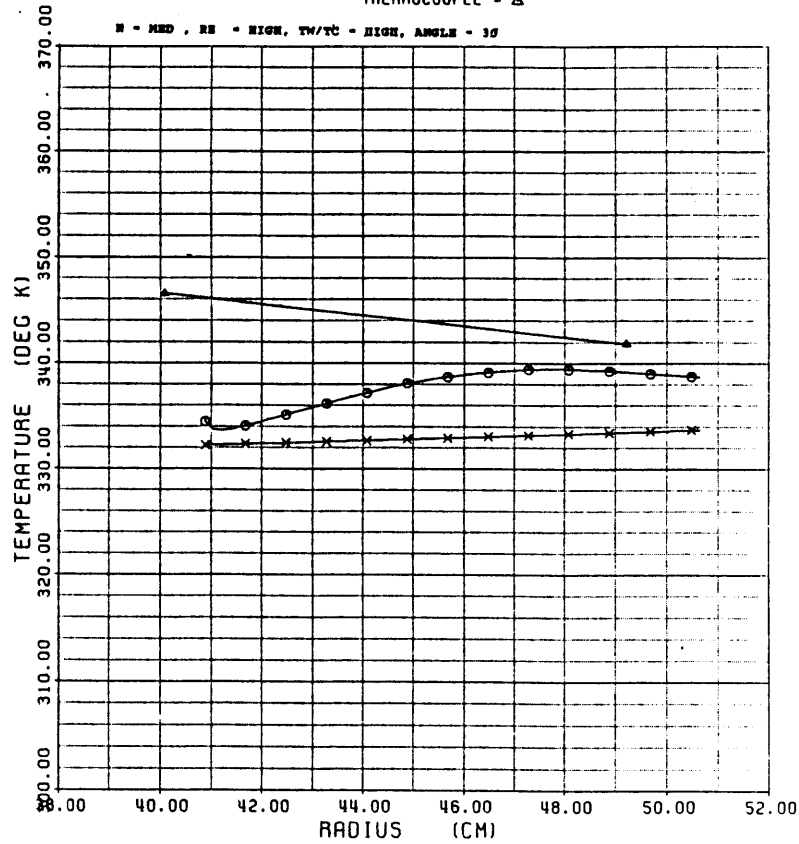


Figure 17C

# AVERAGE NUSSLELT NUMBER

TEST #: 58

SYMBOLS: NU NO BASED ON LOCAL GAS TEMP =  $\circ$   
 NU NO BASED ON COOLANT TEMP =  $\times$   
 CHUPP'S CORRELATION =  $\triangle$   
 MORRIS' CORRELATION =  $\square$

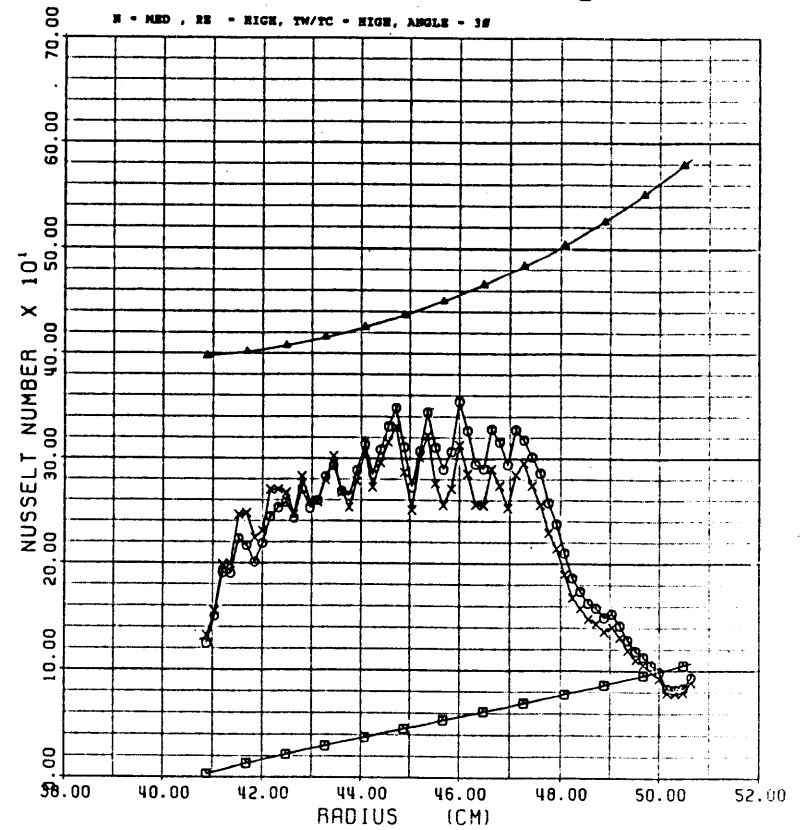


Figure 17D

# VELOCITY VS RADIUS

TEST #: 63

SYMBOLS: IMPINGEMENT - ○  
SUPPLY - X

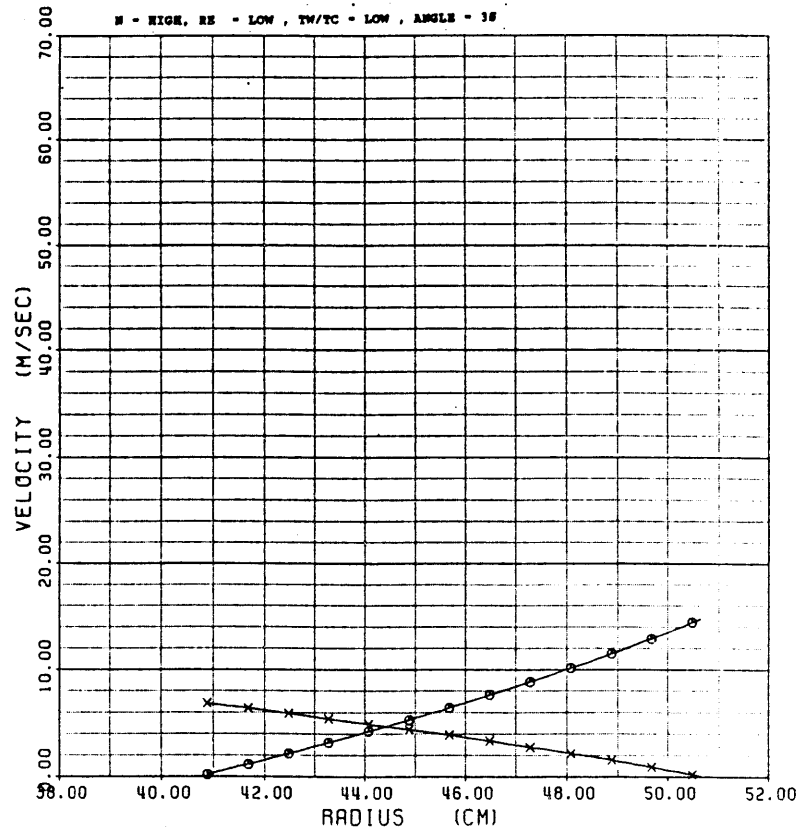


Figure 18A

# PRESSURE VS RADIUS

TEST #: 63

SYMBOLS: IMPINGEMENT - ○  
SUPPLY - X

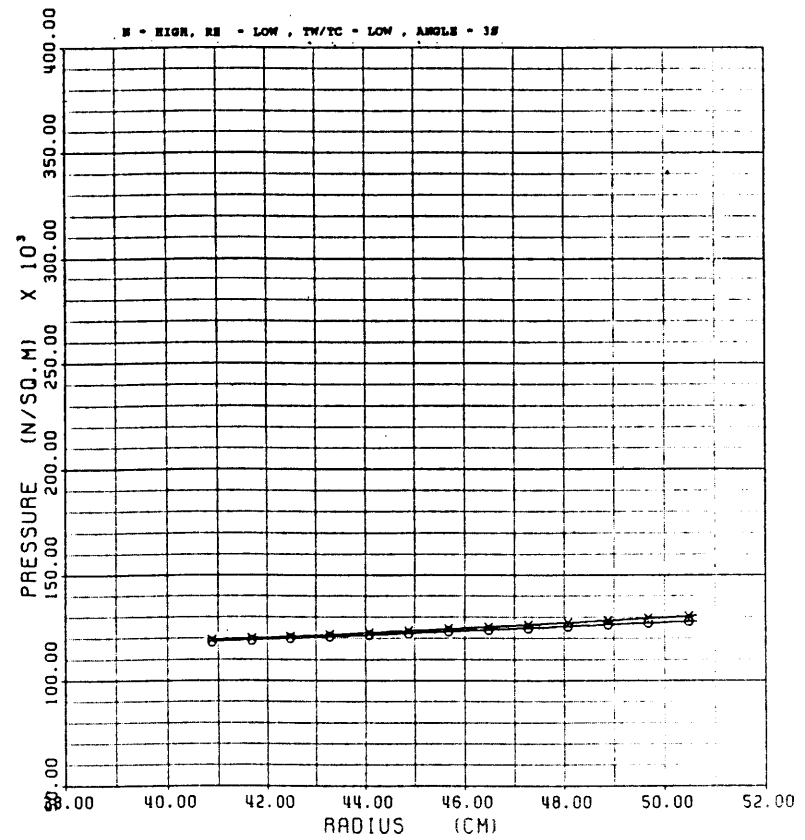


Figure 18B

### TEMPERATURE VS RADIUS

TEST #: 63

SYMBOLS: IMPINGEMENT -  $\odot$   
 SUPPLY -  $\times$   
 THERMOCOUPLE -  $\triangle$

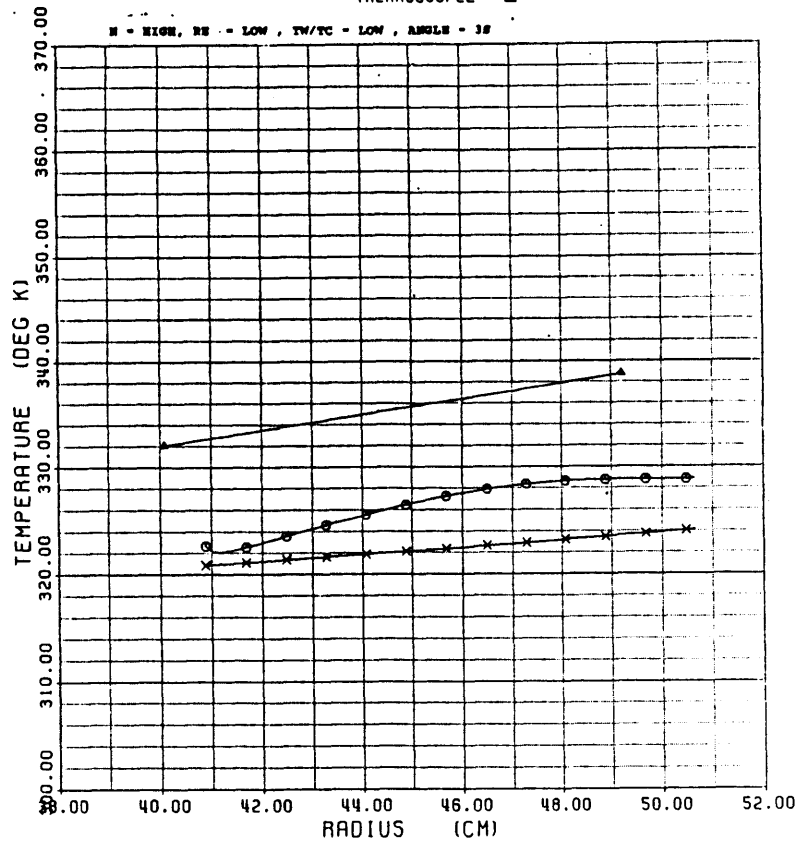


Figure 18C

### AVERAGE NUSSELT NUMBER

TEST #: 63

SYMBOLS: NU NO BASED ON LOCAL GAS TEMP -  $\odot$   
 NU NO BASED ON COOLANT TEMP -  $\times$   
 CHUPP'S CORRELATION -  $\triangle$   
 MORRIS' CORRELATION -  $\square$

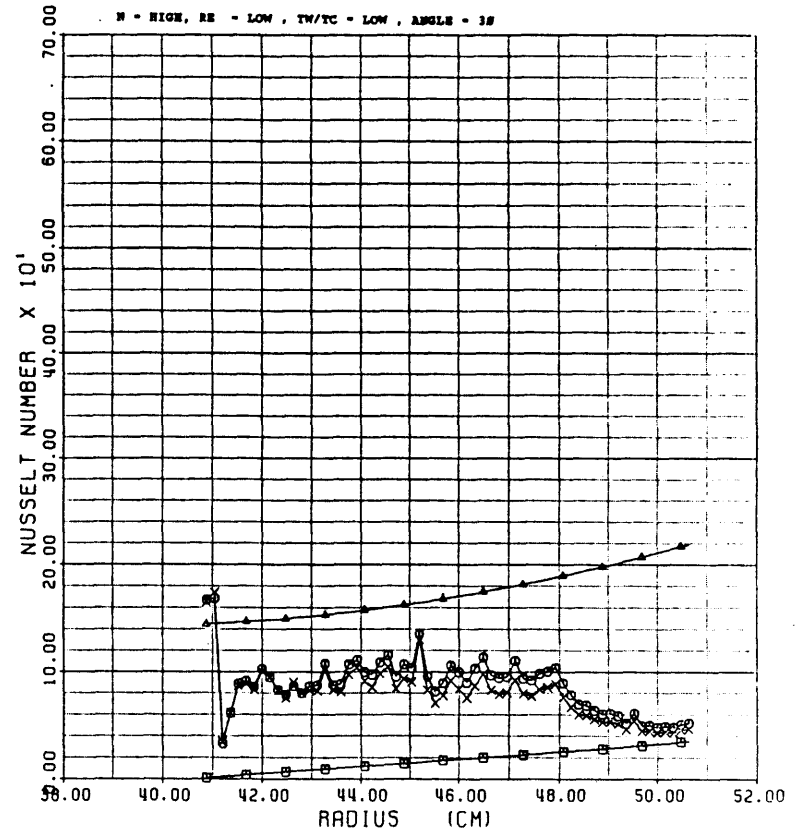


Figure 18D

### VELOCITY VS RADIUS

TEST #: 65

SYMBOLS: IMPINGEMENT - ○  
SUPPLY - X

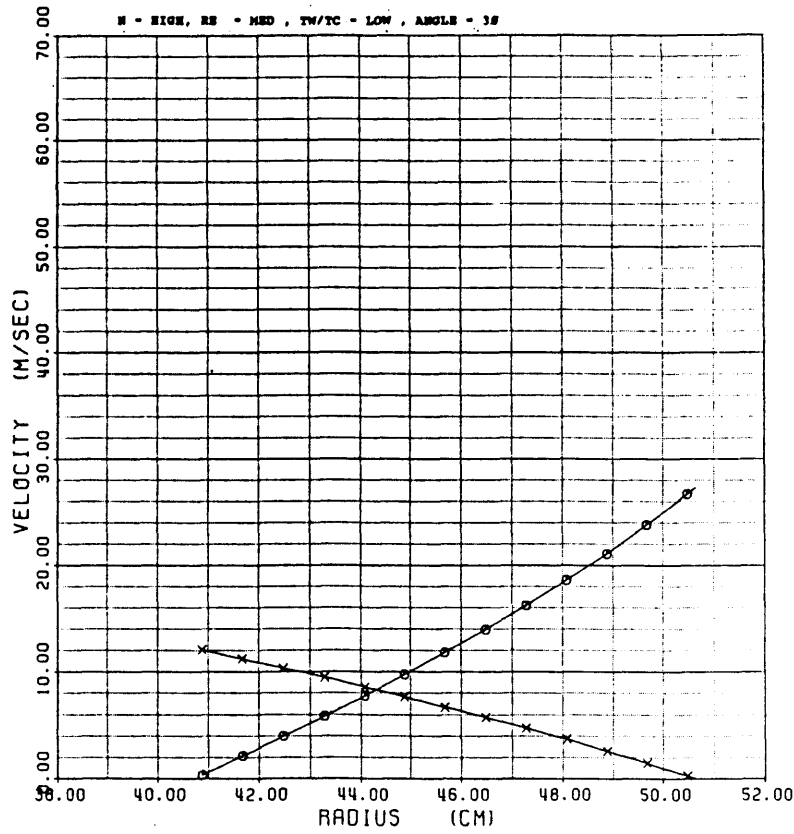


Figure 19A

### PRESSURE VS RADIUS

TEST #: 65

SYMBOLS: IMPINGEMENT - ○  
SUPPLY - X

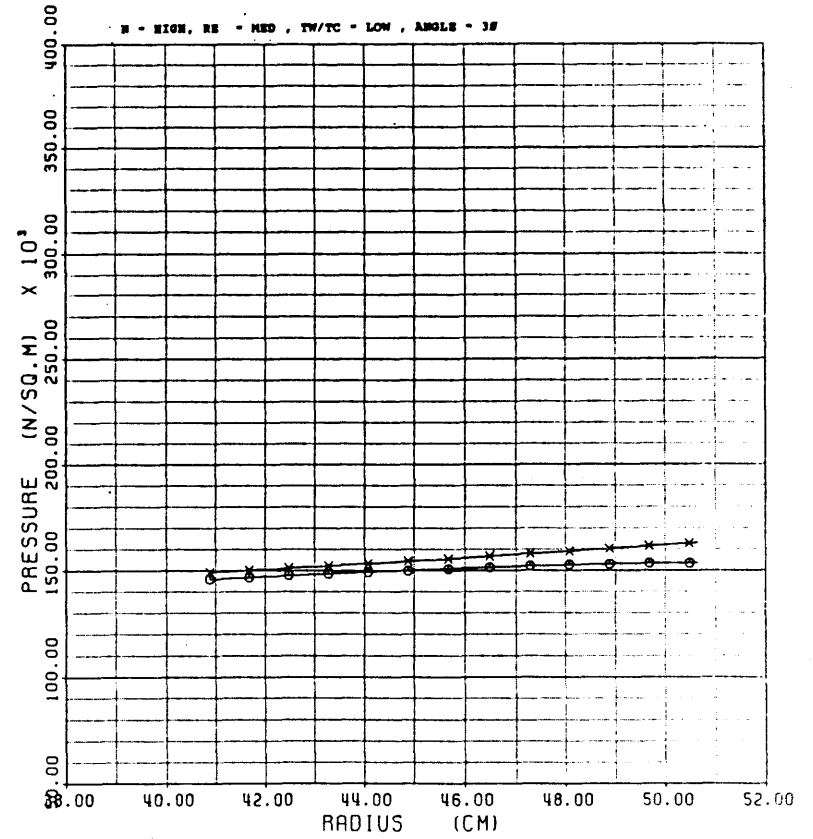


Figure 19B

### TEMPERATURE VS RADIUS

TEST #: 65

SYMBOLS: IMPINGEMENT - ○  
 SUPPLY - X  
 THERMOCOUPLE - ▲

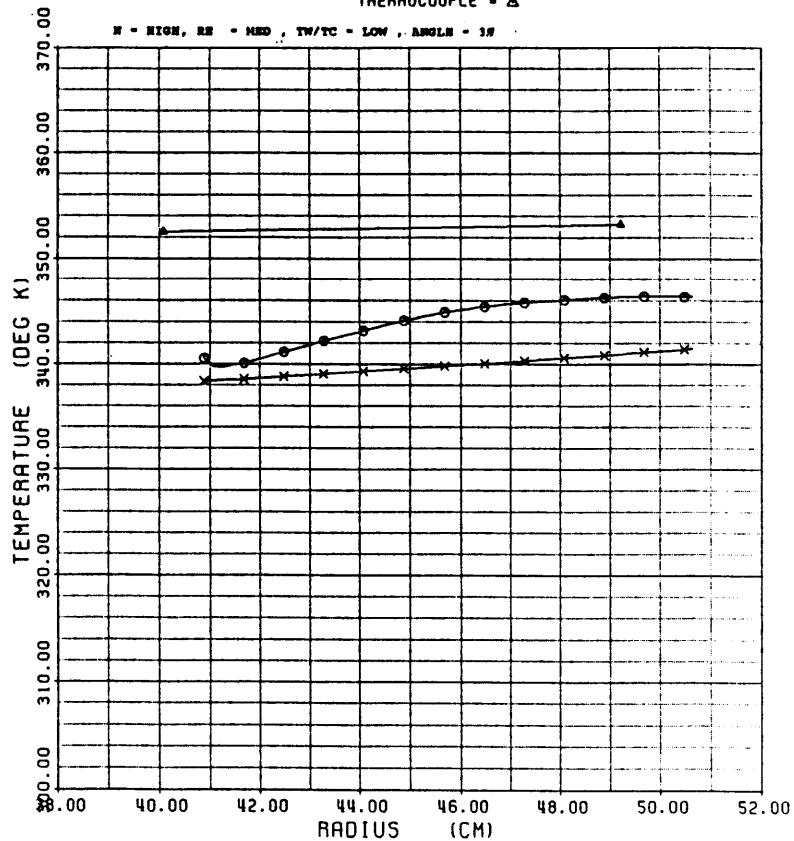


Figure 19C

### AVERAGE NUSSELT NUMBER

TEST #: 65

SYMBOLS: NU NO BASED ON LOCAL GAS TEMP - ○  
 NU NO BASED ON COOLANT TEMP - X  
 CHUPP'S CORRELATION - ▲  
 MORRIS' CORRELATION - □

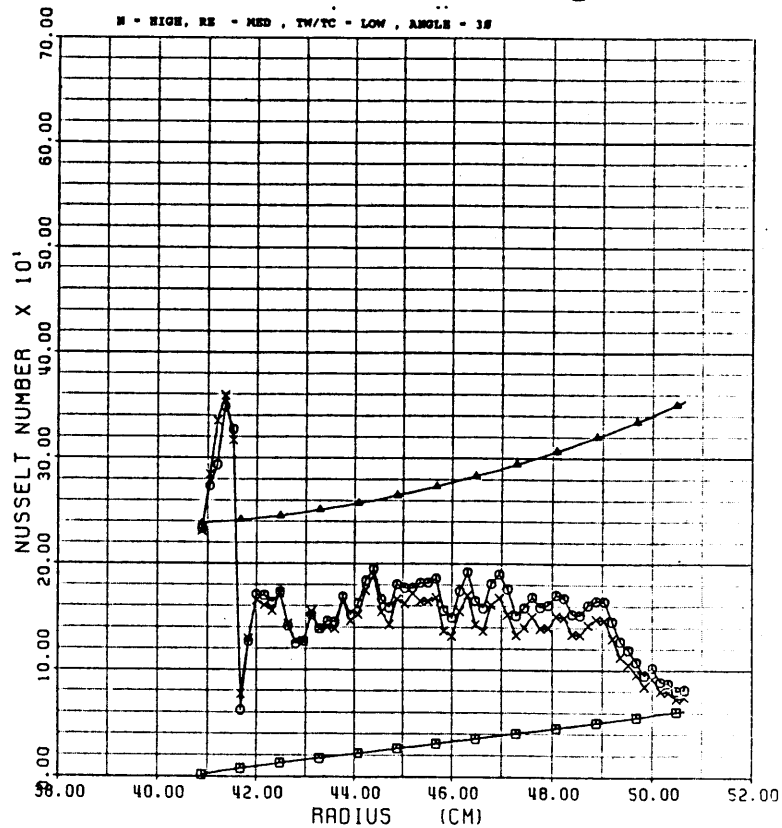


Figure 19D

# VELOCITY VS RADIUS

TEST #: 64

SYMBOLS: IMPINGEMENT = ○  
SUPPLY = X

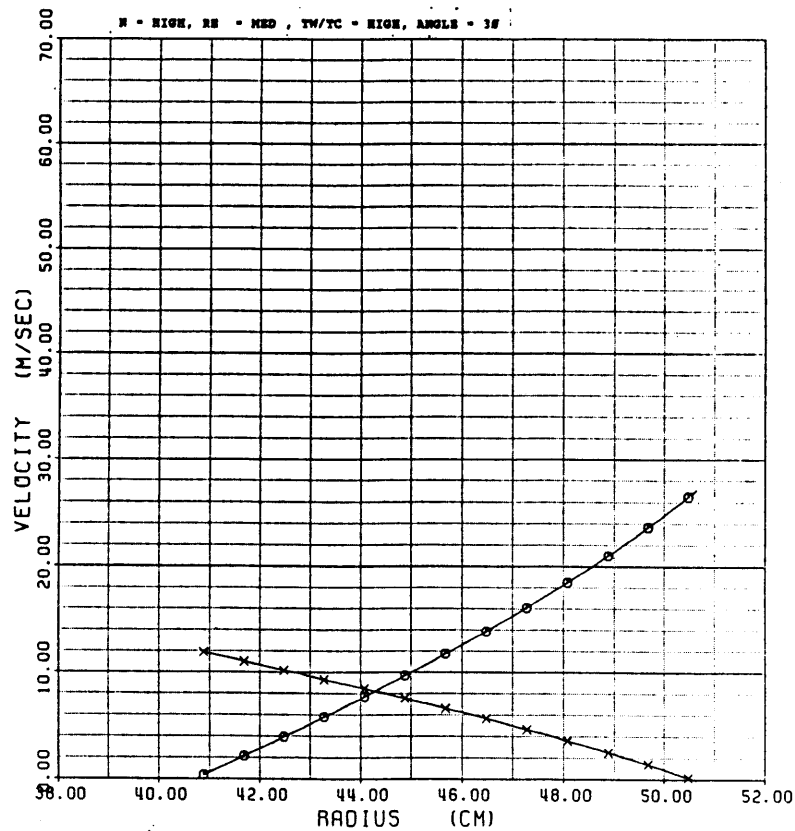


Figure 20A

# PRESSURE VS RADIUS

TEST #: 64

SYMBOLS: IMPINGEMENT = ○  
SUPPLY = X

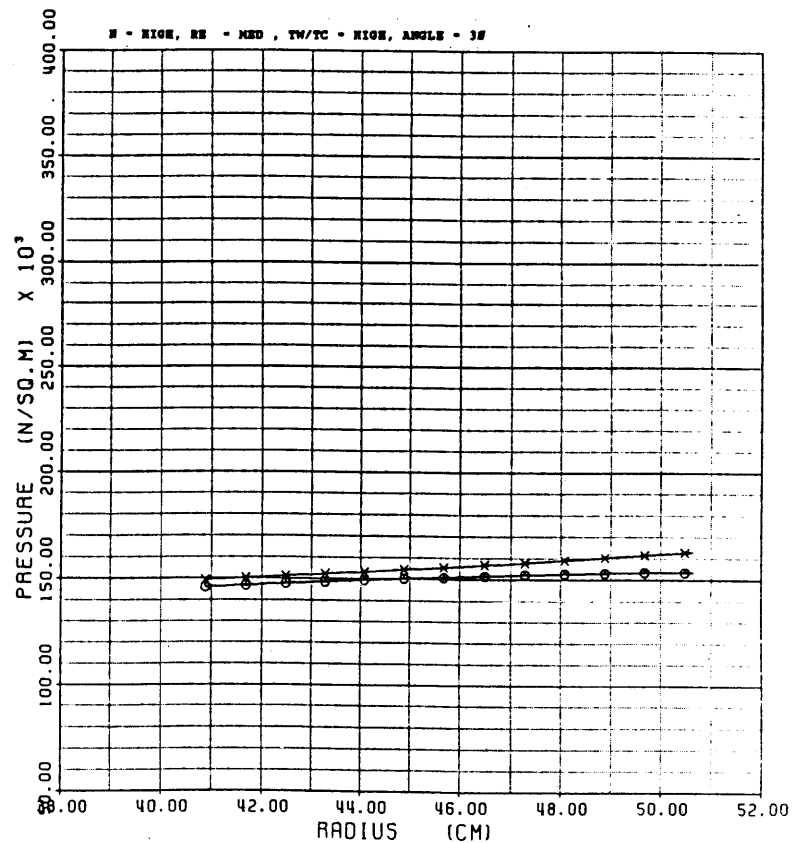


Figure 20B

### TEMPERATURE VS RADIUS

TEST #: 64

SYMBOLS: IMPINGEMENT - ○  
 SUPPLY - X  
 THERMOCOUPLE - ▲

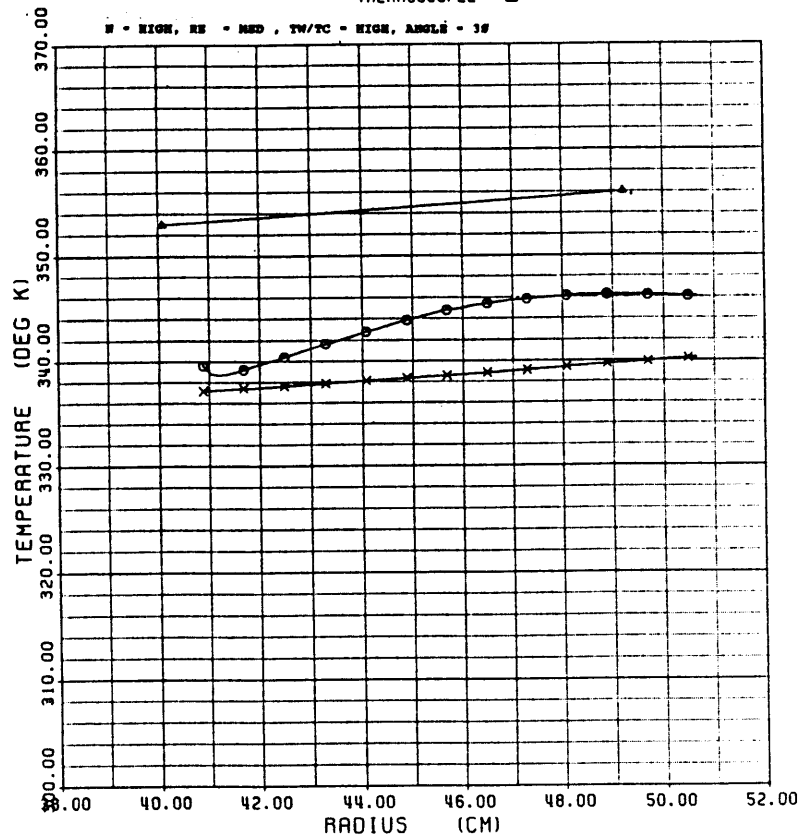


Figure 20C

### AVERAGE NUSSELT NUMBER

TEST #: 64

SYMBOLS: NU NO BASED ON LOCAL GAS TEMP - ○  
 NU NO BASED ON COOLANT TEMP - X  
 CHUPP'S CORRELATION - ▲  
 MORRIS' CORRELATION - □

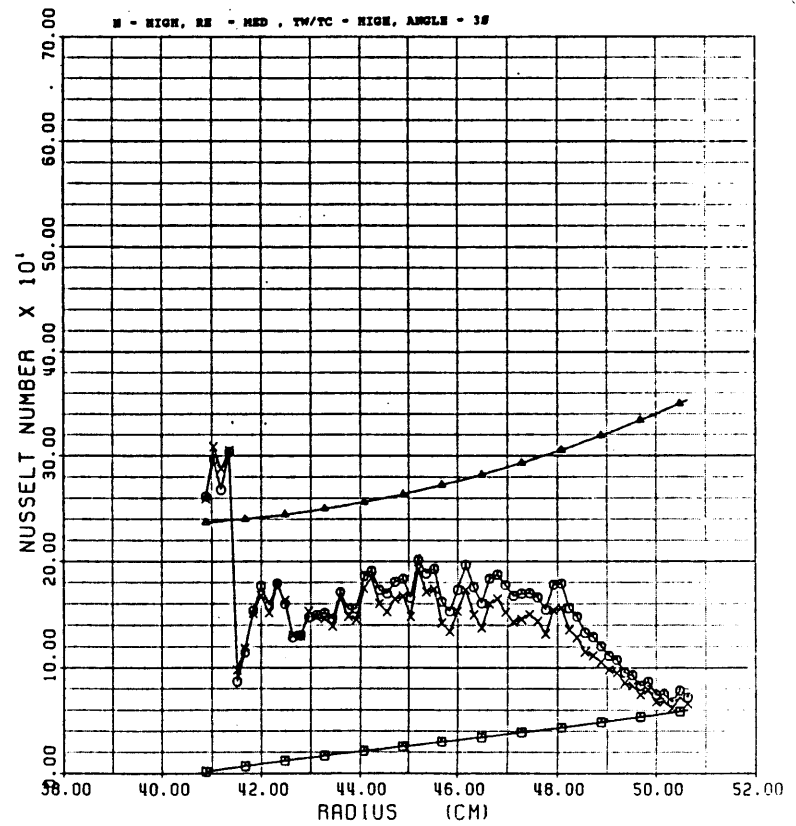


Figure 20D

# VELOCITY VS RADIUS

TEST #: 66

SYMBOLS: IMPINGEMENT - ○  
SUPPLY - X

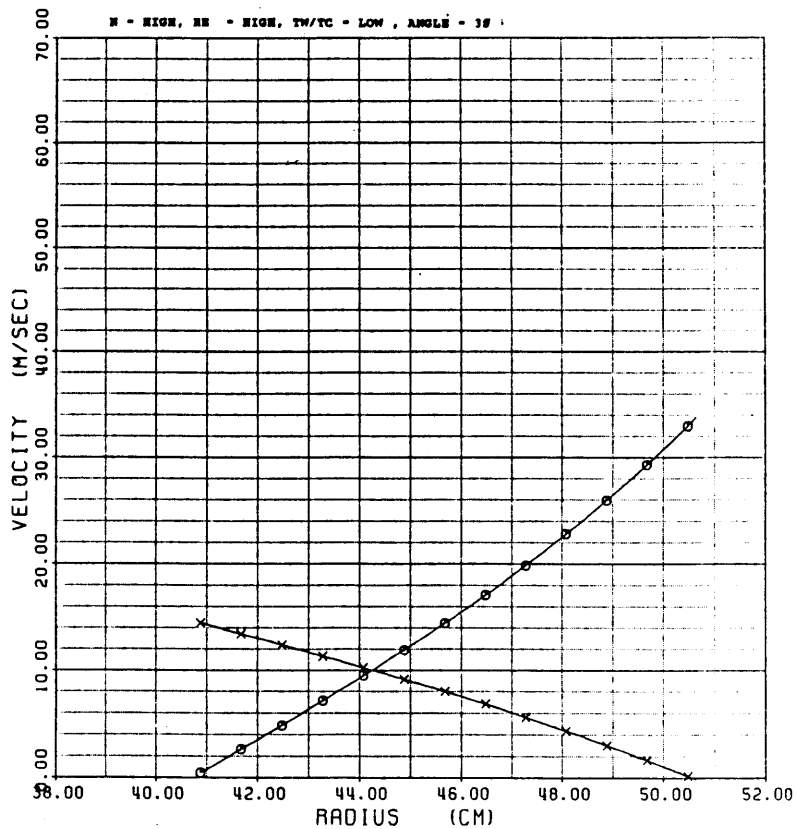


Figure 21A

# PRESSURE VS RADIUS

TEST #: 66

SYMBOLS: IMPINGEMENT - ○  
SUPPLY - X

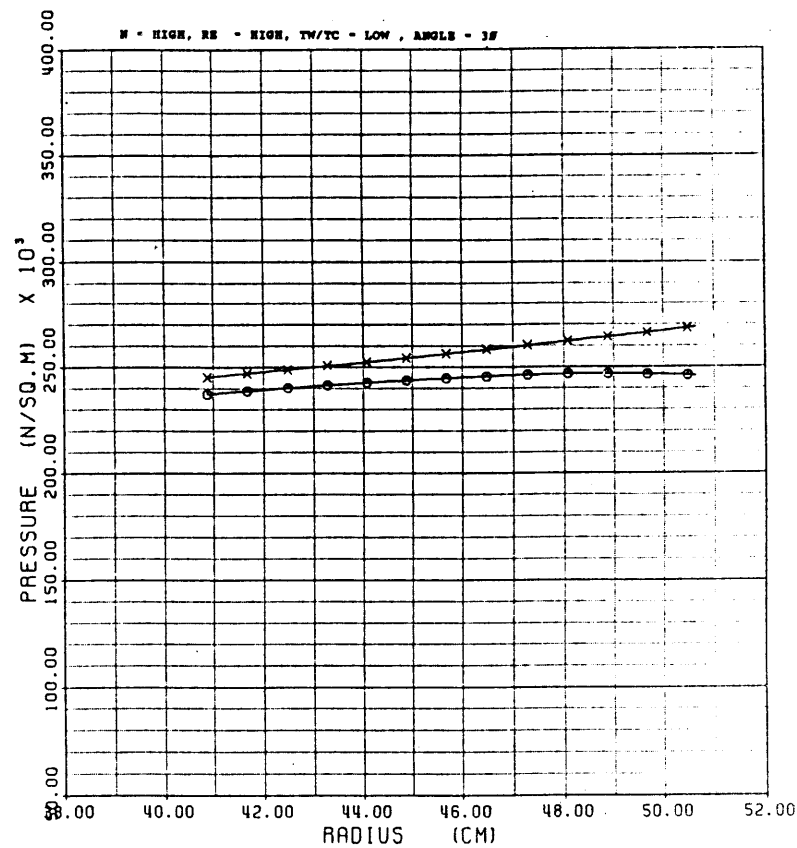


Figure 21B

### TEMPERATURE VS RADIUS

TEST #: 66

SYMBOLS: IMPINGEMENT -  $\circ$   
 SUPPLY -  $\times$   
 THERMOCOUPLE -  $\triangle$

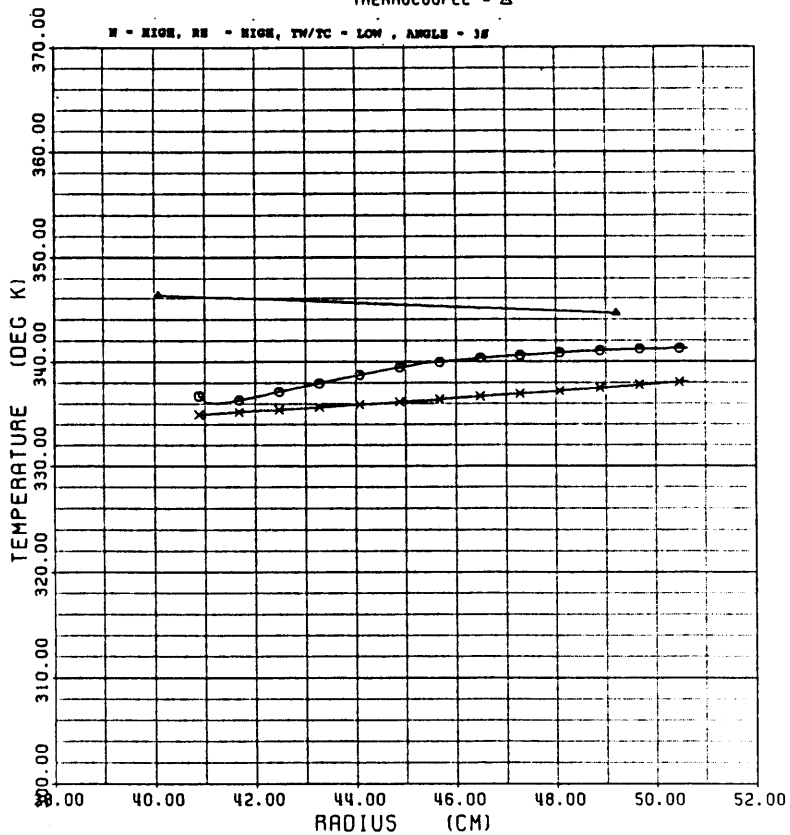


Figure 21C

### AVERAGE NUSSELT NUMBER

TEST #: 66

SYMBOLS: NU NO BASED ON LOCAL GAS TEMP -  $\circ$   
 NU NO BASED ON COOLANT TEMP -  $\times$   
 CHUPP'S CORRELATION -  $\triangle$   
 MORRIS' CORRELATION -  $\square$

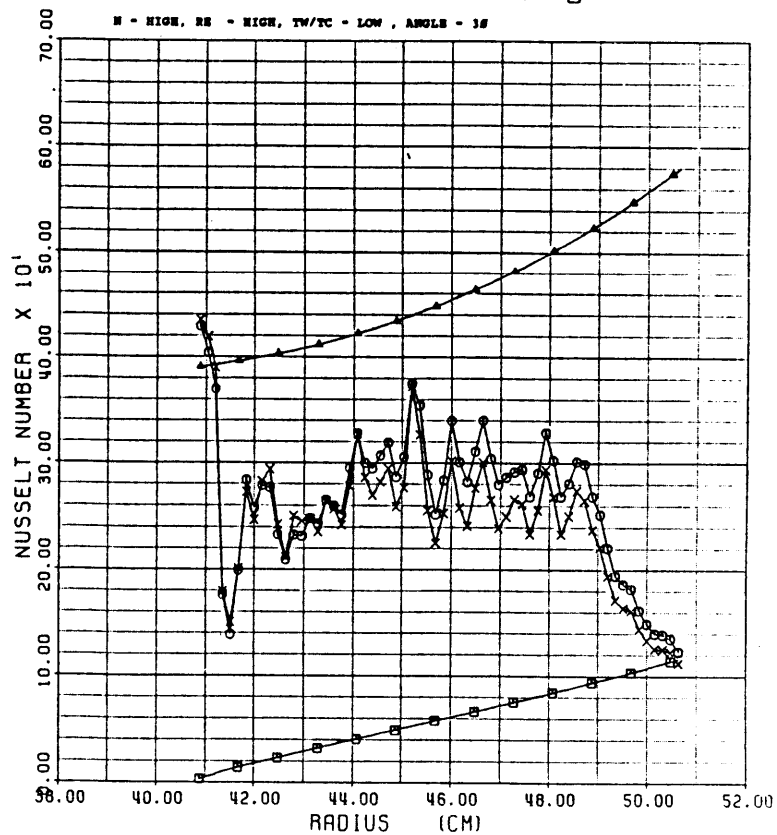


Figure 21D

VELOCITY VS RADIUS

TEST #: 67

SYMBOLS: IMPINGEMENT -  $\odot$   
 SUPPLY - X

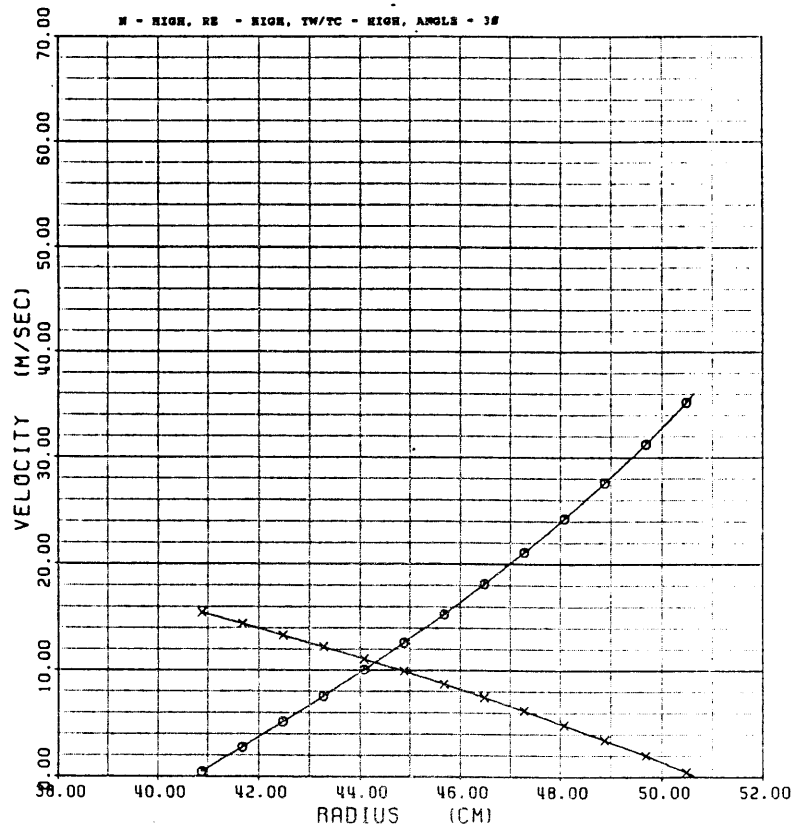


Figure 22A

PRESSURE VS RADIUS

TEST #: 67

SYMBOLS: IMPINGEMENT -  $\odot$   
 SUPPLY - X

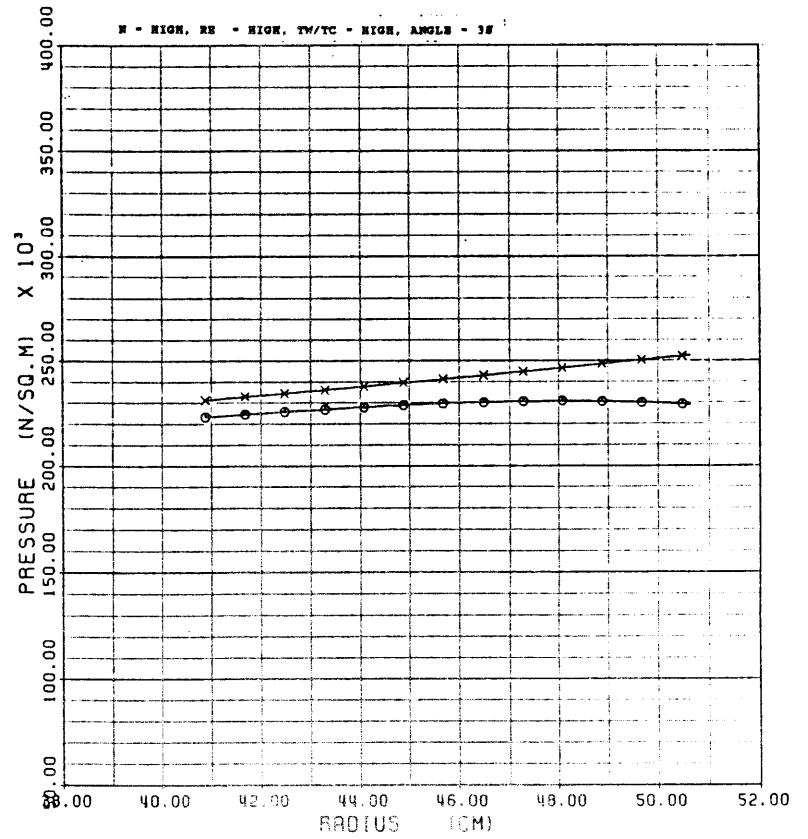


Figure 22B

### TEMPERATURE VS RADIUS

TEST #: 67

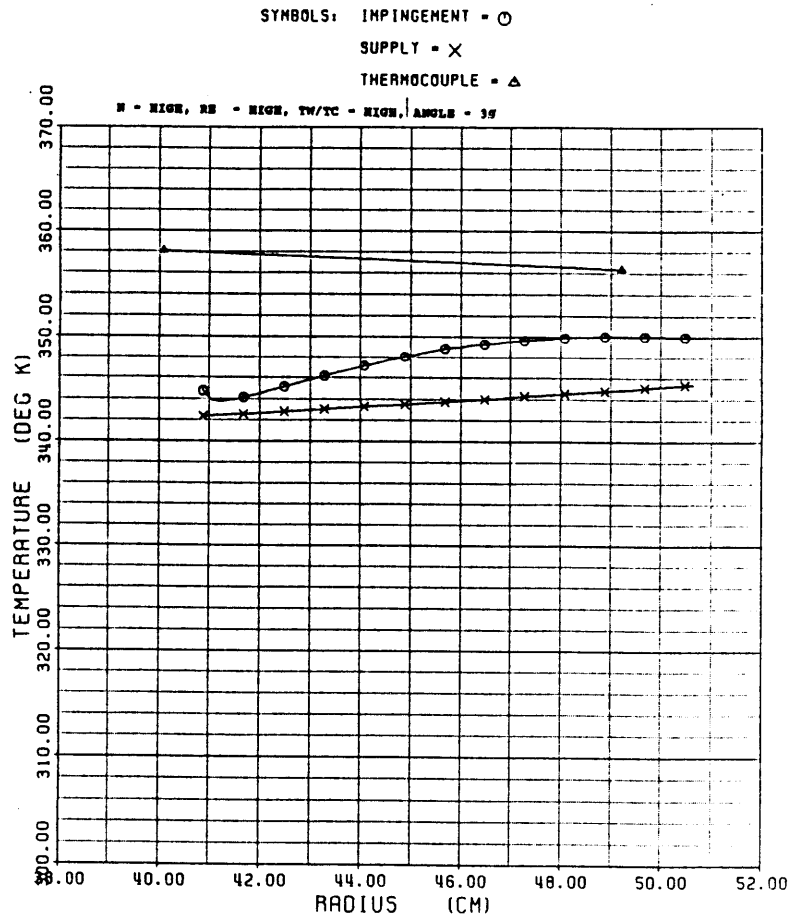


Figure 22C

### AVERAGE NUSSELT NUMBER

TEST #: 67

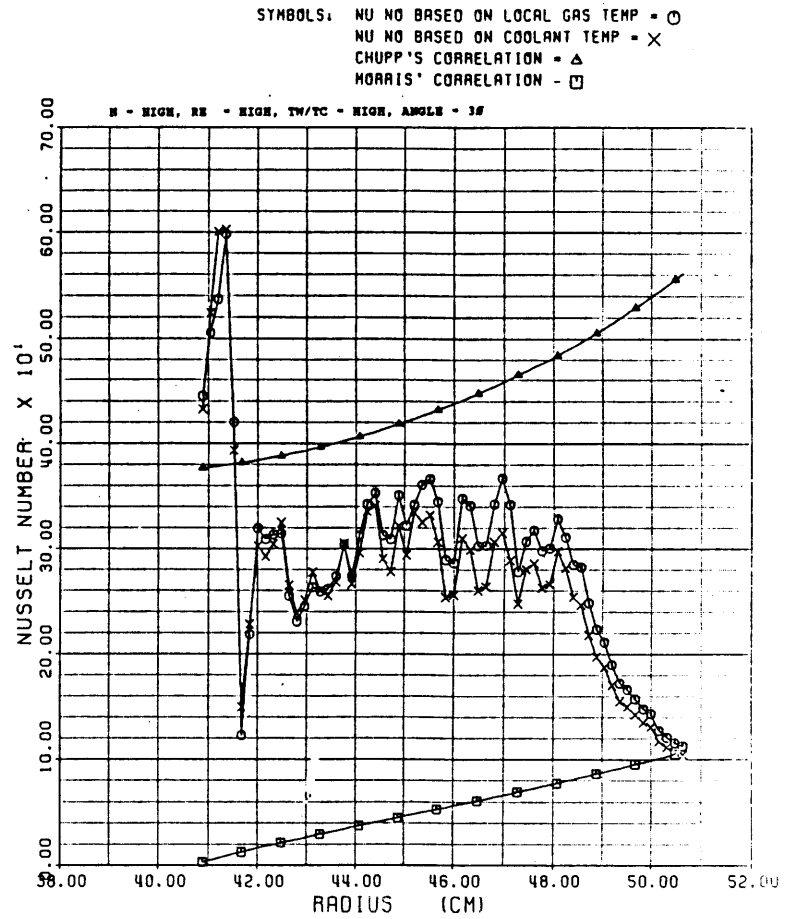


Figure 22D

### VELOCITY VS RADIUS

TEST #: 113

SYMBOLS: IMPINGEMENT - ○  
SUPPLY - X

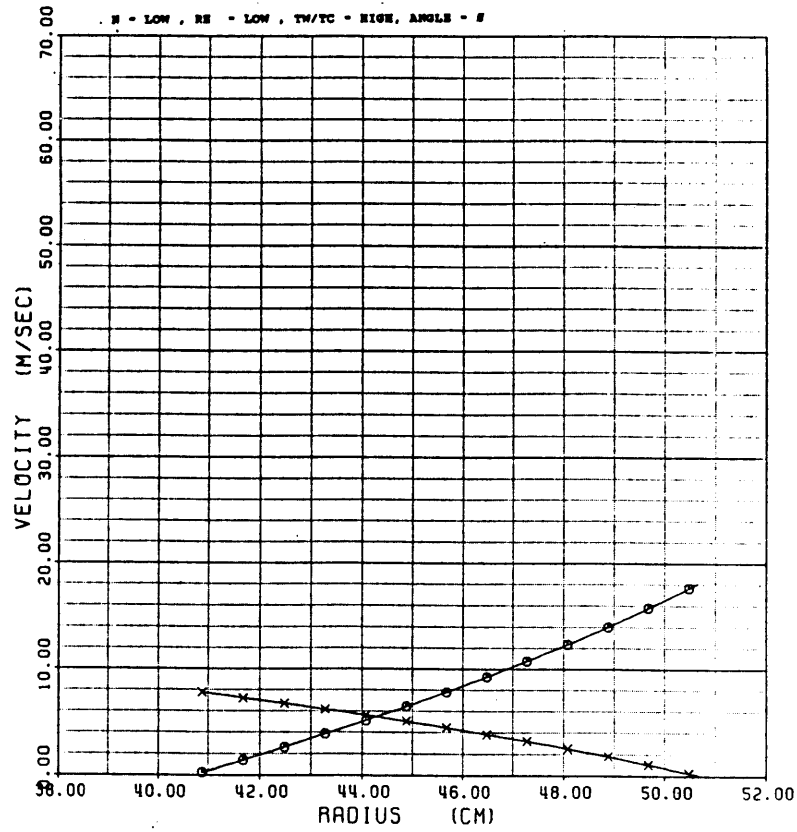


Figure 23A

### PRESSURE VS RADIUS

TEST #: 113

SYMBOLS: IMPINGEMENT - ○  
SUPPLY - X

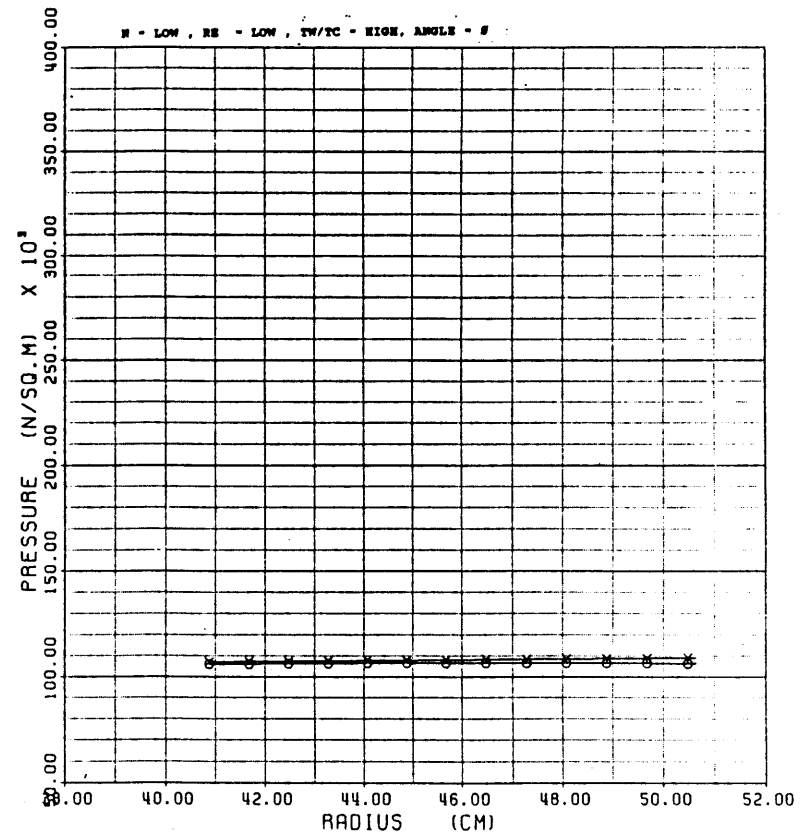


Figure 23B

### TEMPERATURE VS RADIUS

TEST #: 113

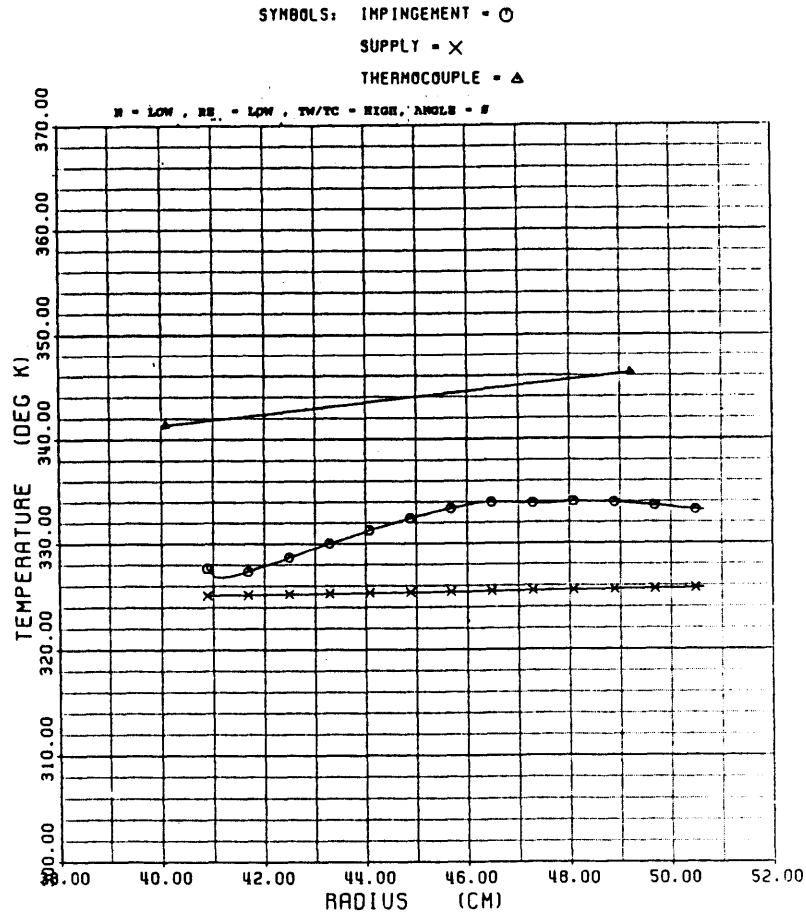


Figure 23C

### AVERAGE NUSSELT NUMBER

TEST #: 113

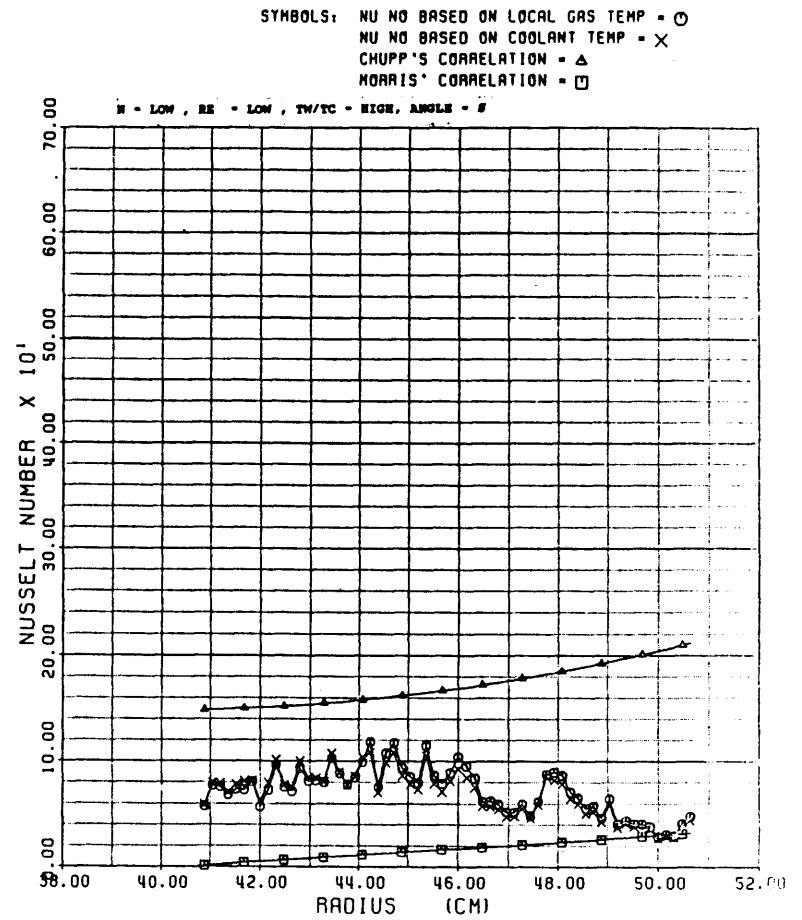


Figure 23D

### VELOCITY VS RADIUS

TEST #: 114

SYMBOLS: IMPINGEMENT - ○  
SUPPLY - X

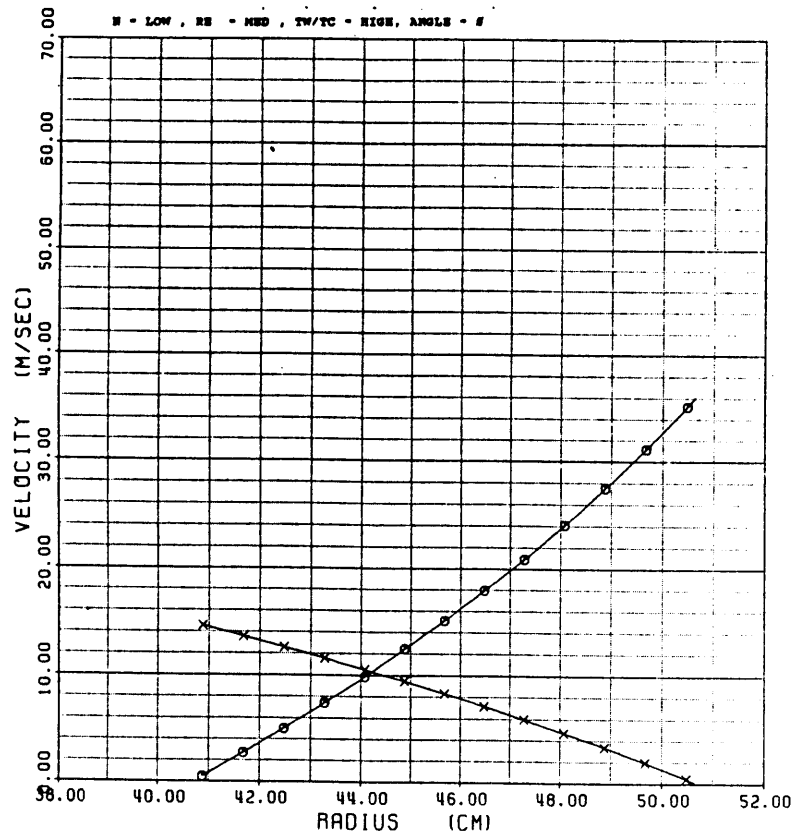


Figure 24A

### PRESSURE VS RADIUS

TEST #: 114

SYMBOLS: IMPINGEMENT - ○  
SUPPLY - X

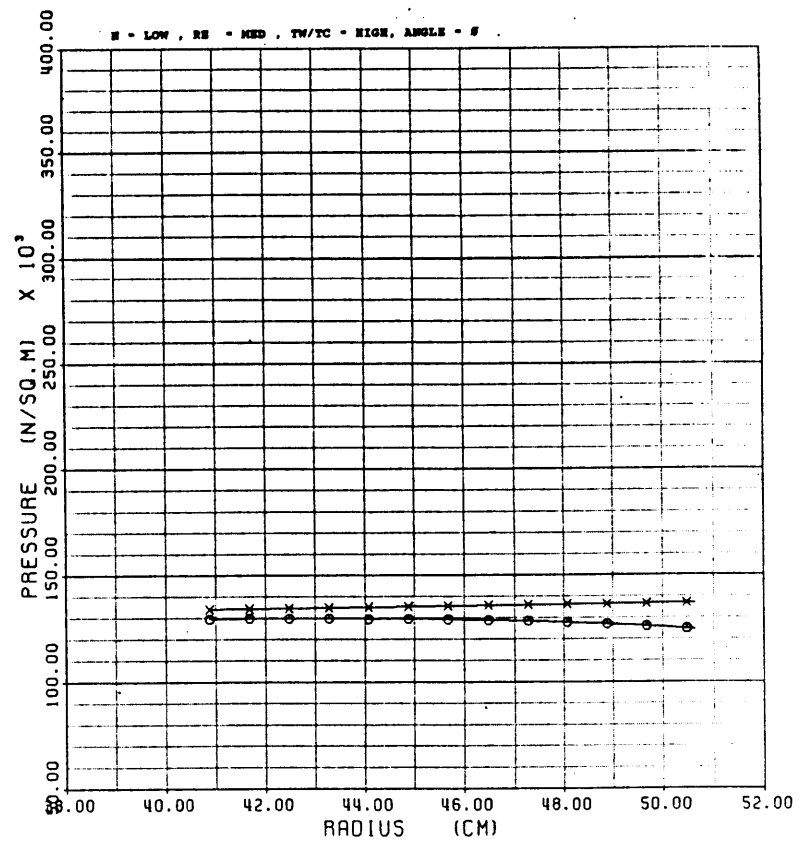


Figure 24B

### TEMPERATURE VS RADIUS

TEST #: 114

SYMBOLS: IMPINGEMENT -  $\circ$   
 SUPPLY -  $\times$   
 THERMOCOUPLE -  $\triangle$

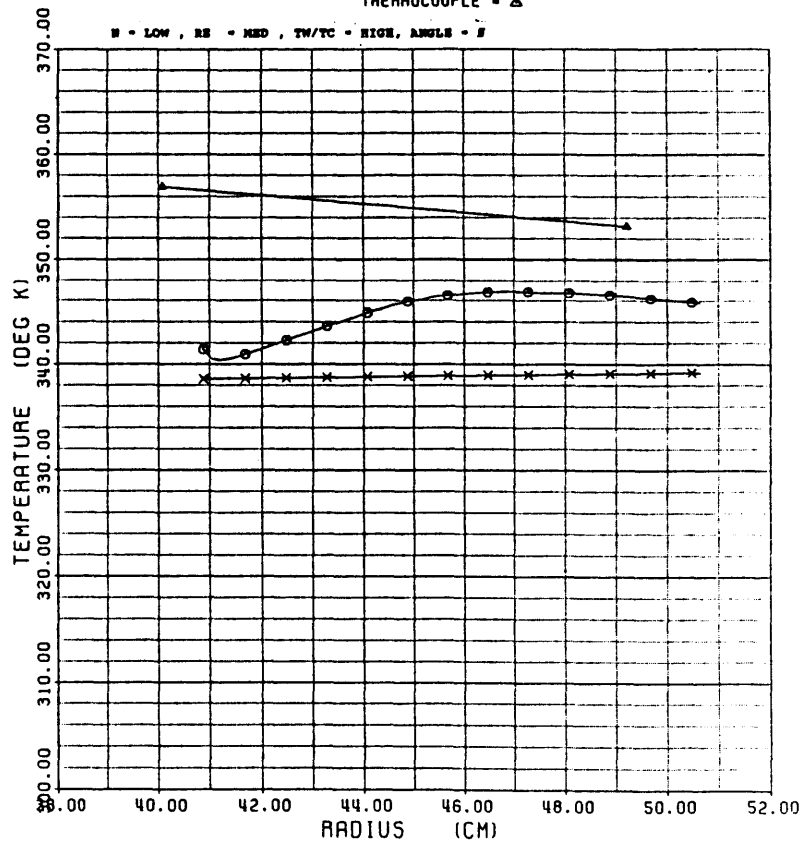


Figure 24C

### AVERAGE NUSSLELT NUMBER

TEST #: 114

SYMBOLS: NU NO BASED ON LOCAL GAS TEMP -  $\circ$   
 NU NO BASED ON COOLANT TEMP -  $\times$   
 CHUPP'S CORRELATION -  $\triangle$   
 MORRIS' CORRELATION -  $\square$

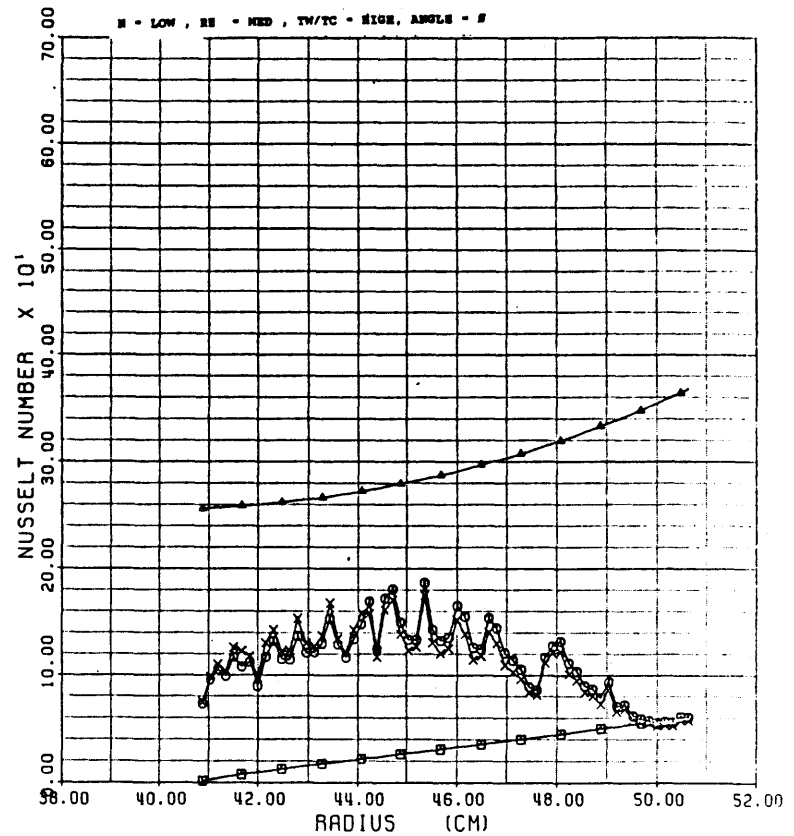


Figure 24D

# VELOCITY VS RADIUS

TEST #: 115

SYMBOLS: IMPINGEMENT - ○  
SUPPLY - X

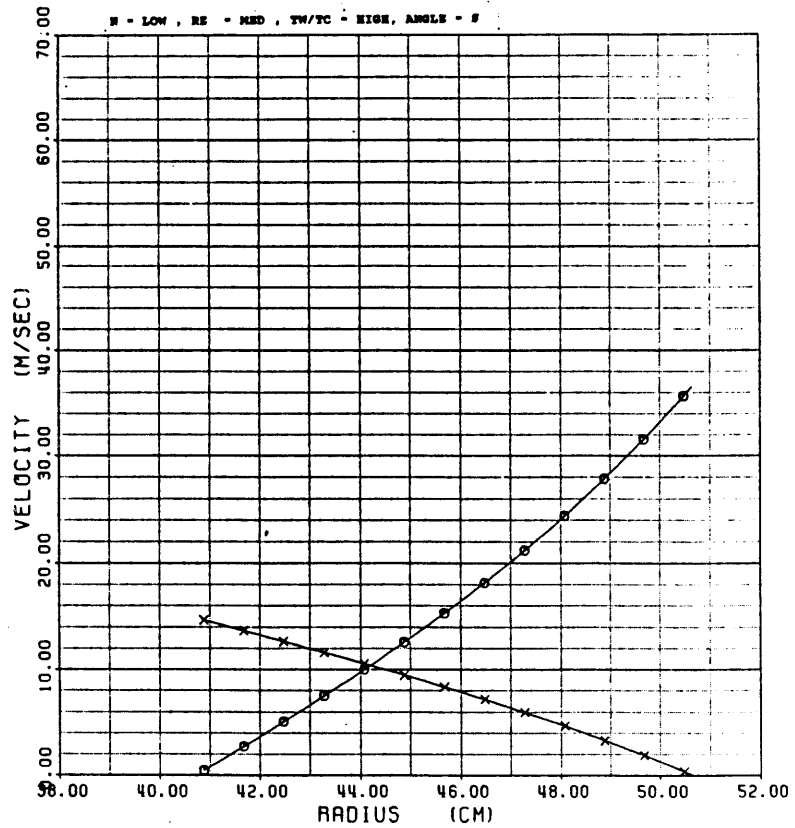


Figure 25A

# PRESSURE VS RADIUS

TEST #: 115

SYMBOLS: IMPINGEMENT - ○  
SUPPLY - X

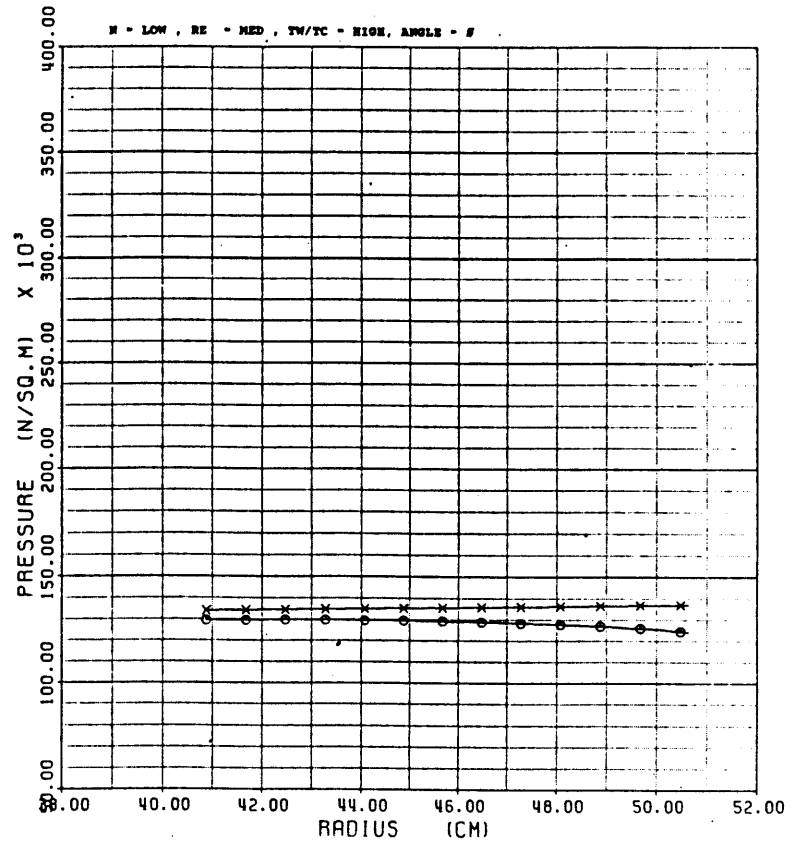


Figure 25B

### TEMPERATURE VS RADIUS

TEST #: 115

SYMBOLS: IMPINGEMENT - ○  
 SUPPLY - ×  
 THERMOCOUPLE - △

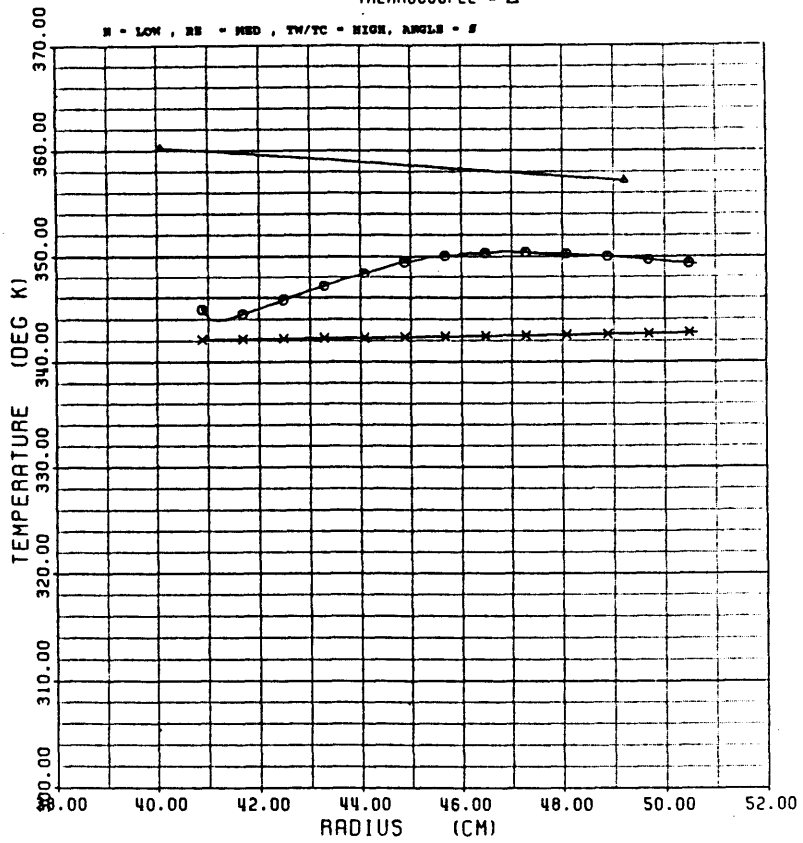


Figure 25C

### AVERAGE NUSSLELT NUMBER

TEST #: 115

SYMBOLS: NU NO BASED ON LOCAL GAS TEMP - ○  
 NU NO BASED ON COOLANT TEMP - ×  
 CHUPP'S CORRELATION - △  
 MORRIS' CORRELATION - □

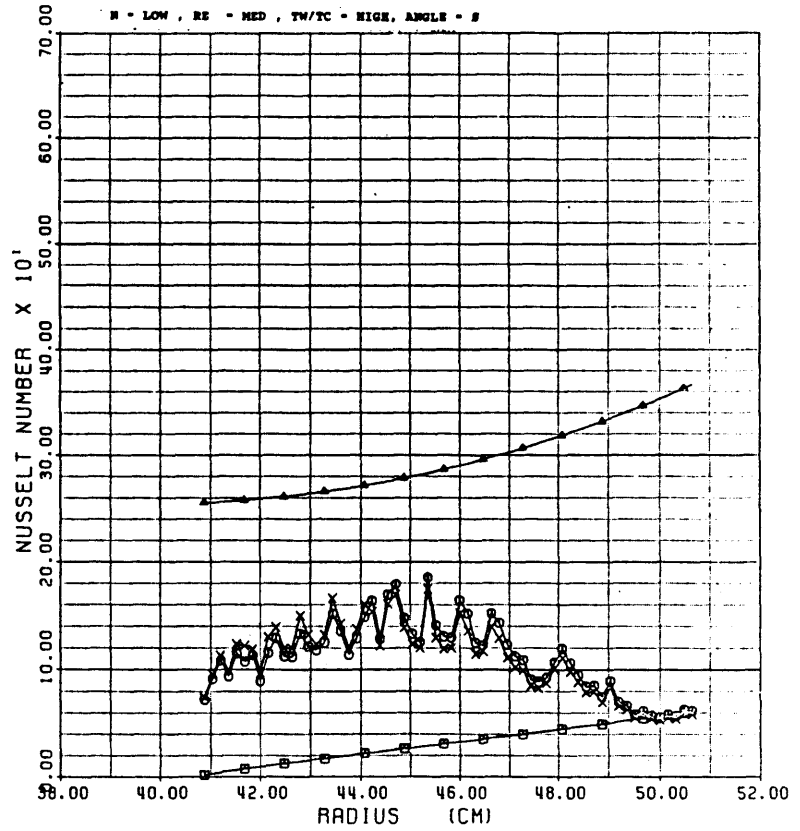


Figure 25D

### VELOCITY VS RADIUS

TEST #: 123

SYMBOLS: IMPINGEMENT -  $\circ$   
 SUPPLY - X

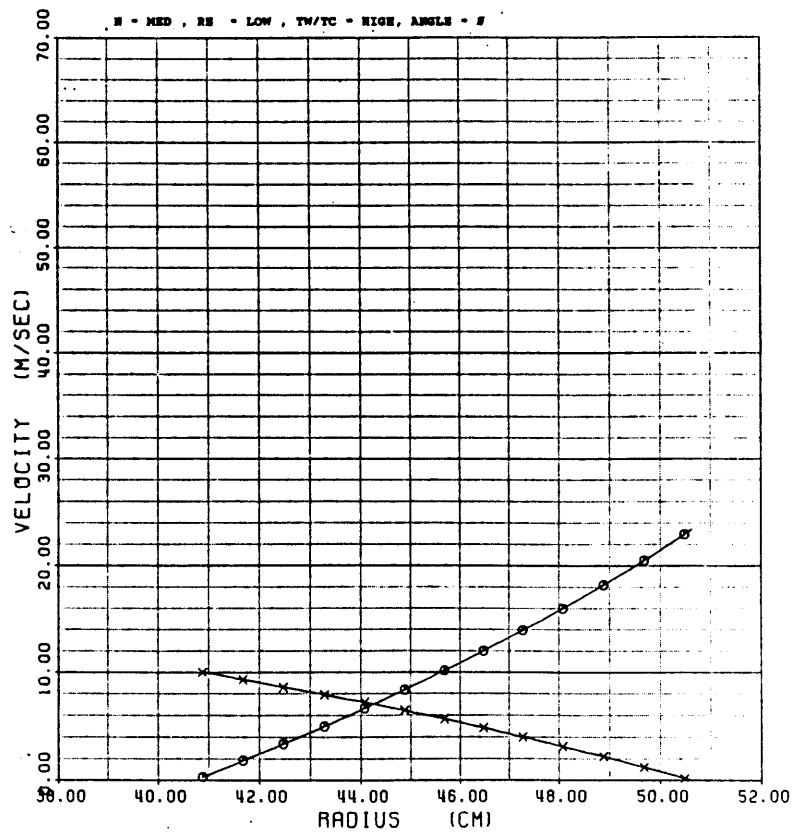


Figure 26A

### PRESSURE VS RADIUS

TEST #: 123

SYMBOLS: IMPINGEMENT -  $\circ$   
 SUPPLY - X

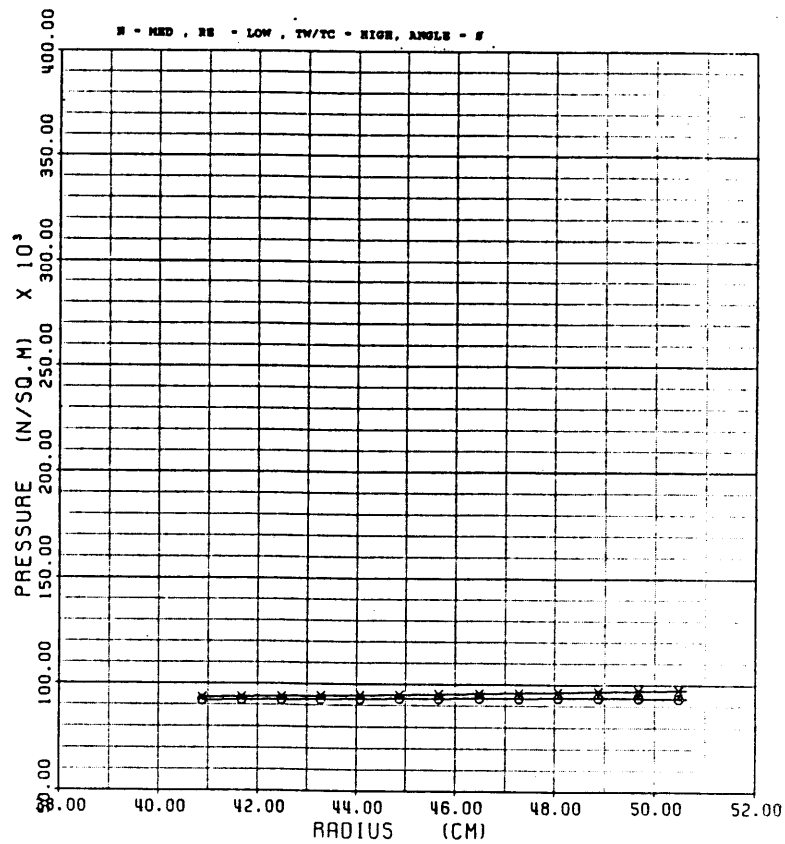


Figure 26B

# TEMPERATURE VS RADIUS

TEST #: 123

SYMBOLS: IMPINGEMENT = ○  
 SUPPLY = ×  
 THERMOCOUPLE = △

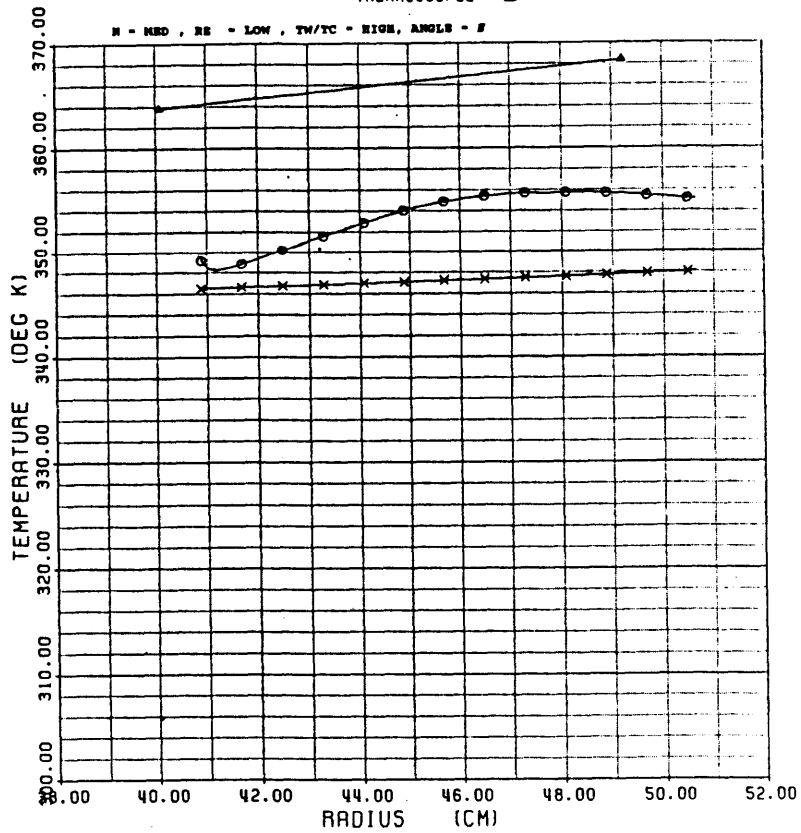


Figure 26C

# AVERAGE NUSSELT NUMBER

TEST #: 123

SYMBOLS: NU NO BASED ON LOCAL GAS TEMP = ○  
 NU NO BASED ON COOLANT TEMP = ×  
 CHUPP'S CORRELATION = △  
 MORRIS' CORRELATION = □

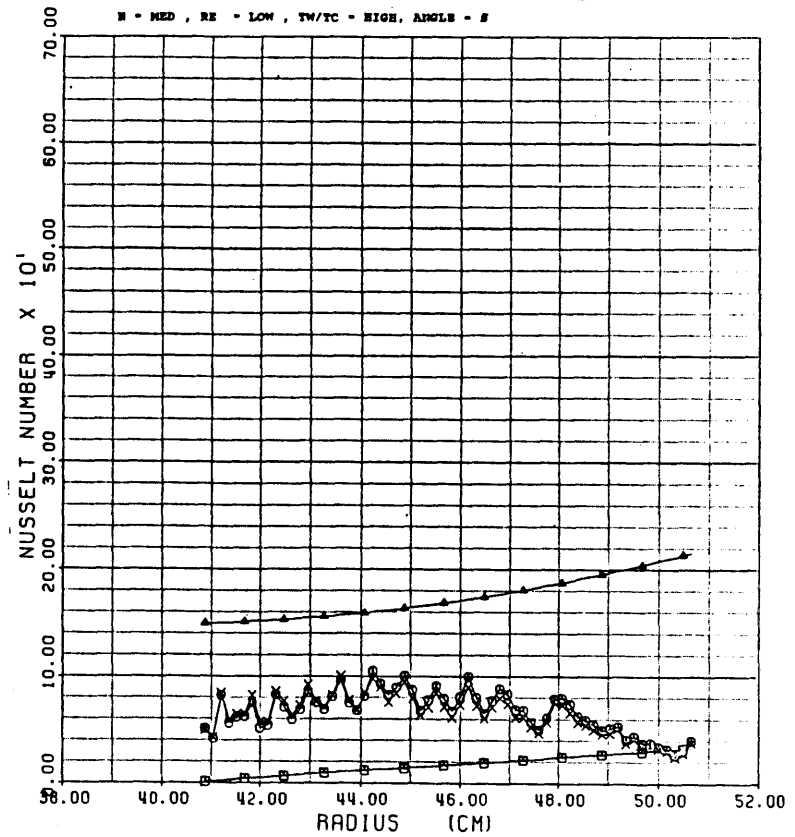


Figure 26D

### VELOCITY VS RADIUS

TEST #: 124

SYMBOLS: IMPINGEMENT - ○  
SUPPLY - X

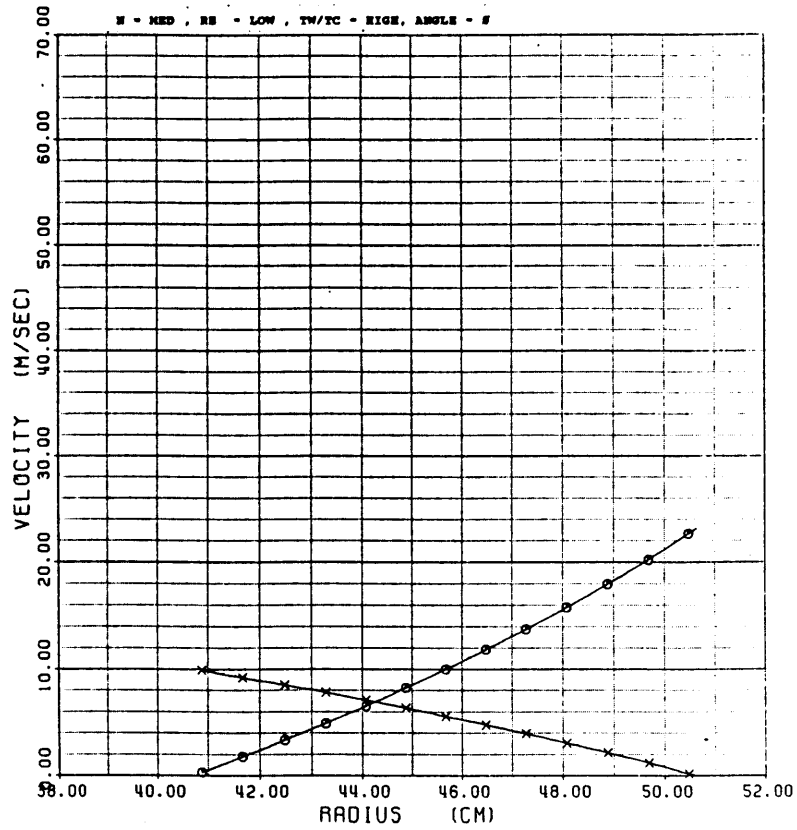


Figure 27A

### PRESSURE VS RADIUS

TEST #: 124

SYMBOLS: IMPINGEMENT - ○  
SUPPLY - X

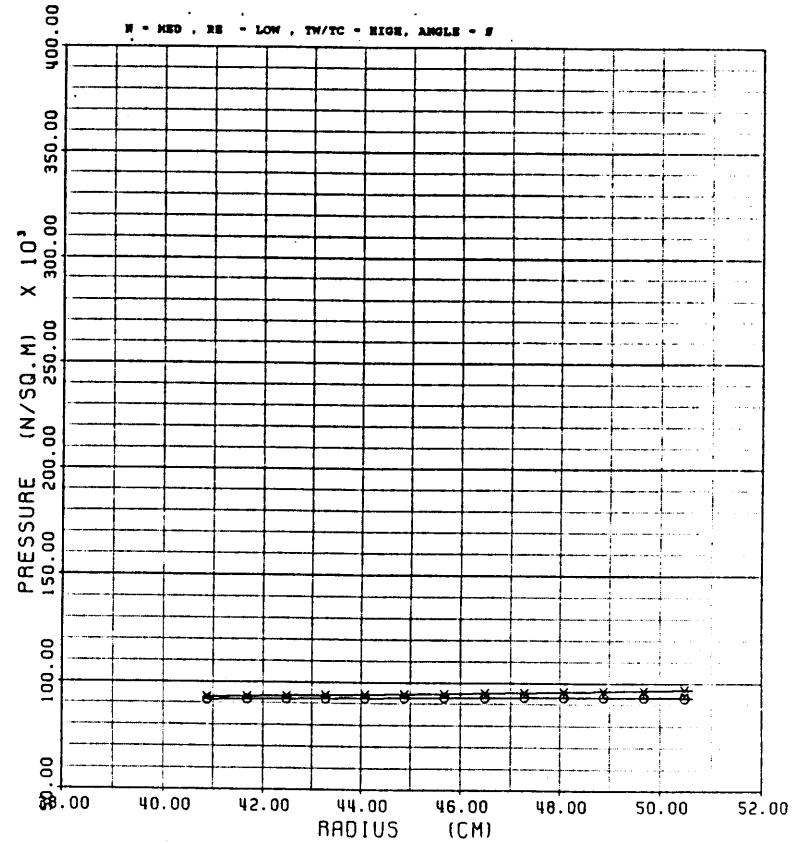


Figure 27B

### TEMPERATURE VS RADIUS

TEST #: 124

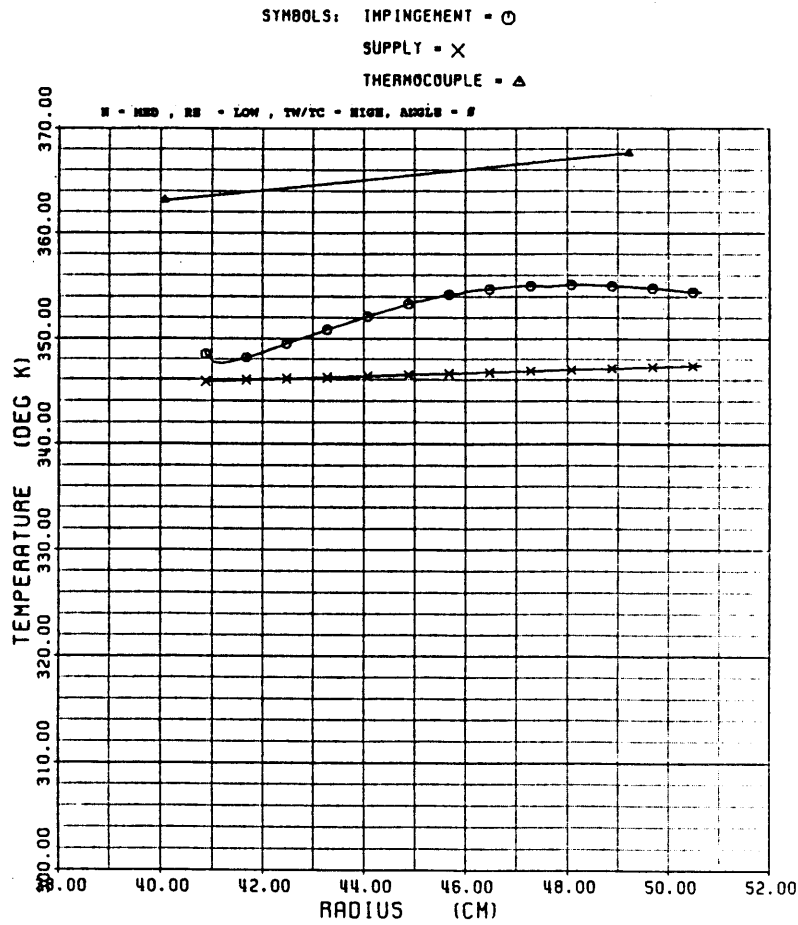


Figure 27C

### AVERAGE NUSSELT NUMBER

TEST #: 124

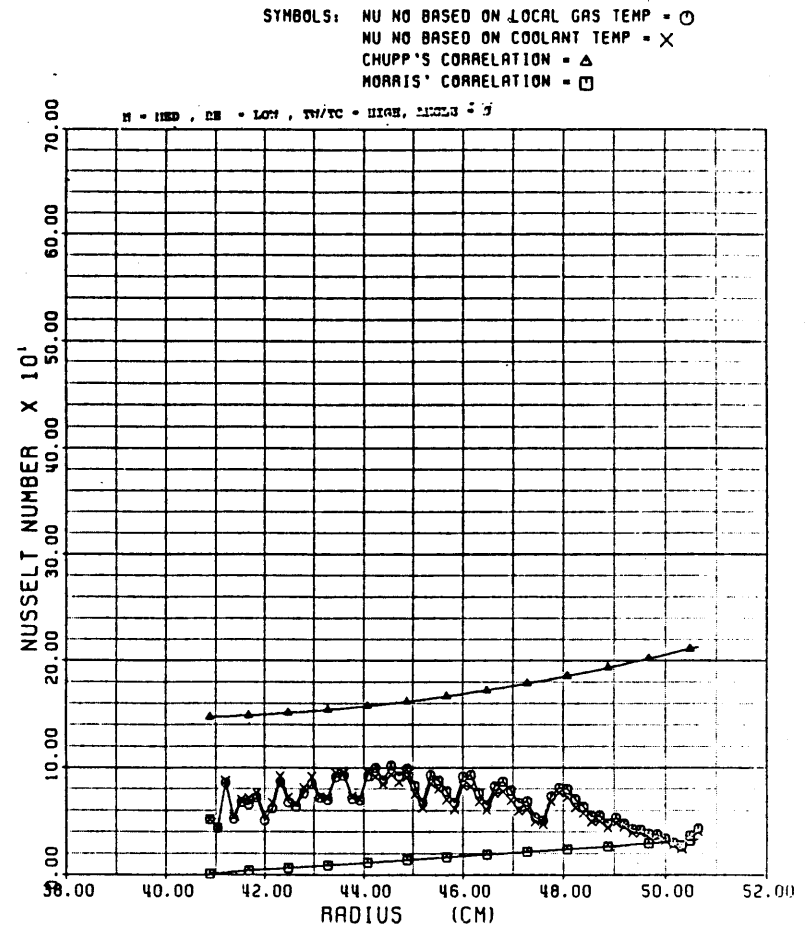


Figure 27D

### VELOCITY VS RADIUS

TEST #: 122

SYMBOLS: IMPINGEMENT - ○  
SUPPLY - X

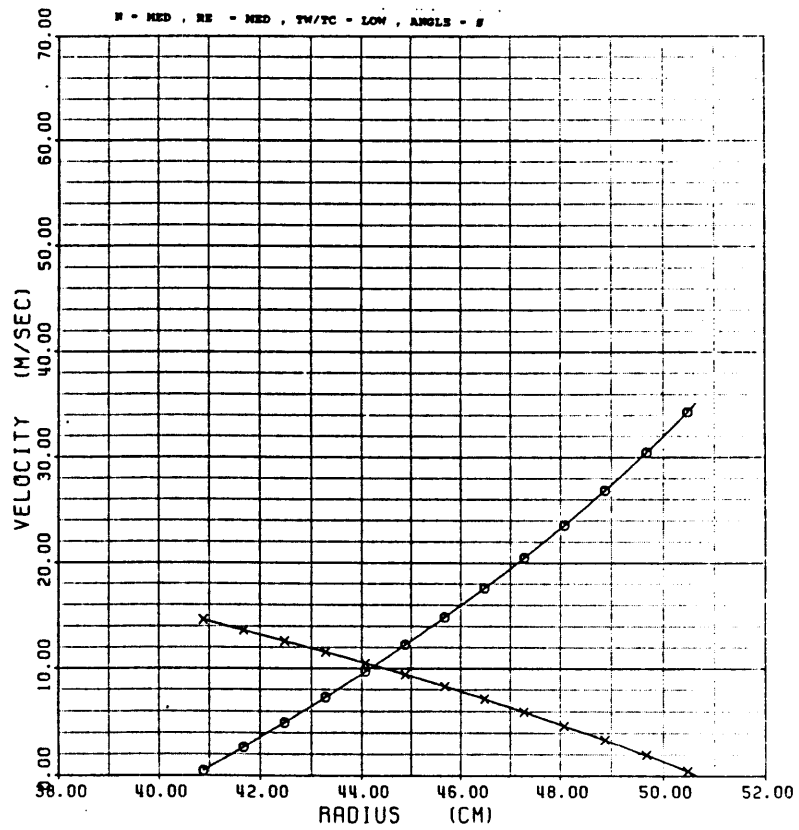


Figure 28A

### PRESSURE VS RADIUS

TEST #: 122

SYMBOLS: IMPINGEMENT - ○  
SUPPLY - X

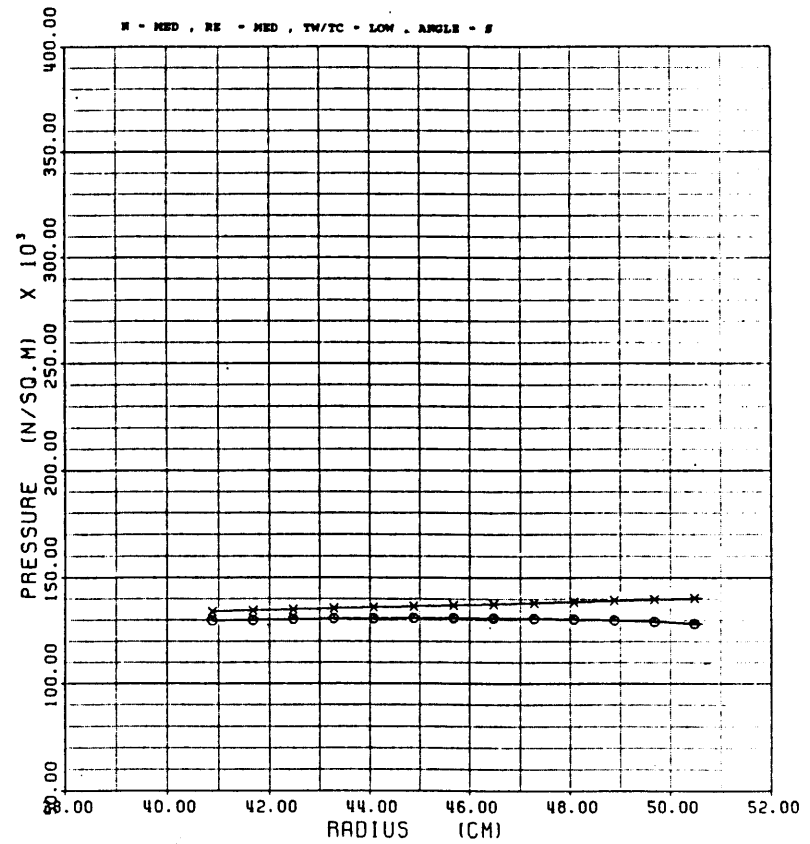


Figure 28B

### TEMPERATURE VS RADIUS

TEST #: 122

SYMBOLS: IMPINGEMENT -  $\circ$   
 SUPPLY -  $\times$   
 THERMOCOUPLE -  $\triangle$

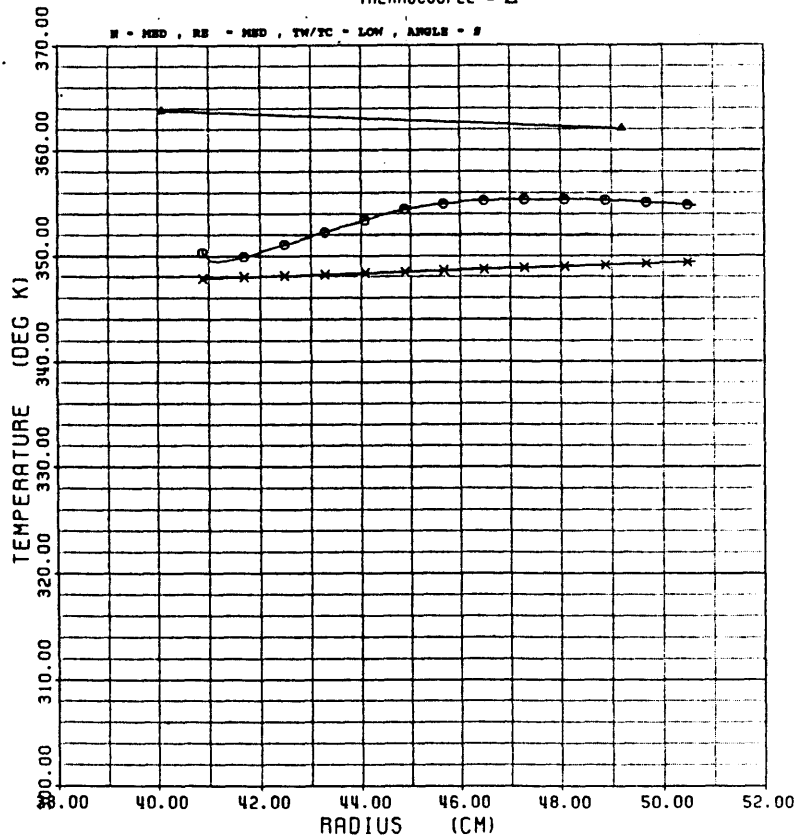


Figure 28C

### AVERAGE NUSSELT NUMBER

TEST #: 122

SYMBOLS: NU NO BASED ON LOCAL GAS TEMP -  $\circ$   
 NU NO BASED ON COOLANT TEMP -  $\times$   
 CHUPP'S CORRELATION -  $\triangle$   
 MORRIS' CORRELATION -  $\square$

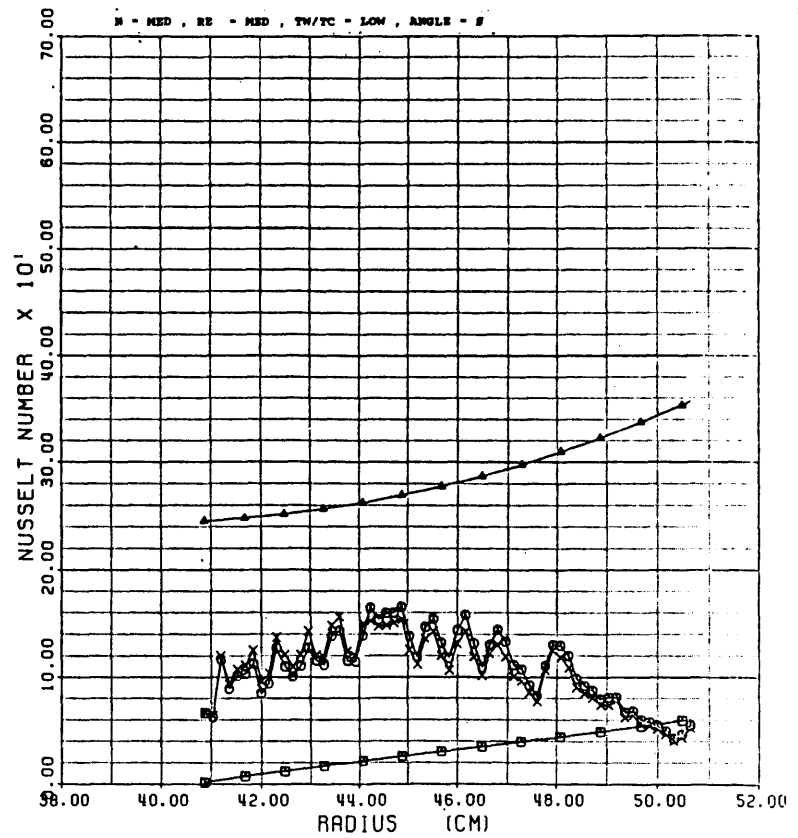


Figure 28D

# VELOCITY VS RADIUS

TEST #: 119

SYMBOLS: IMPINGEMENT - ○  
SUPPLY - X

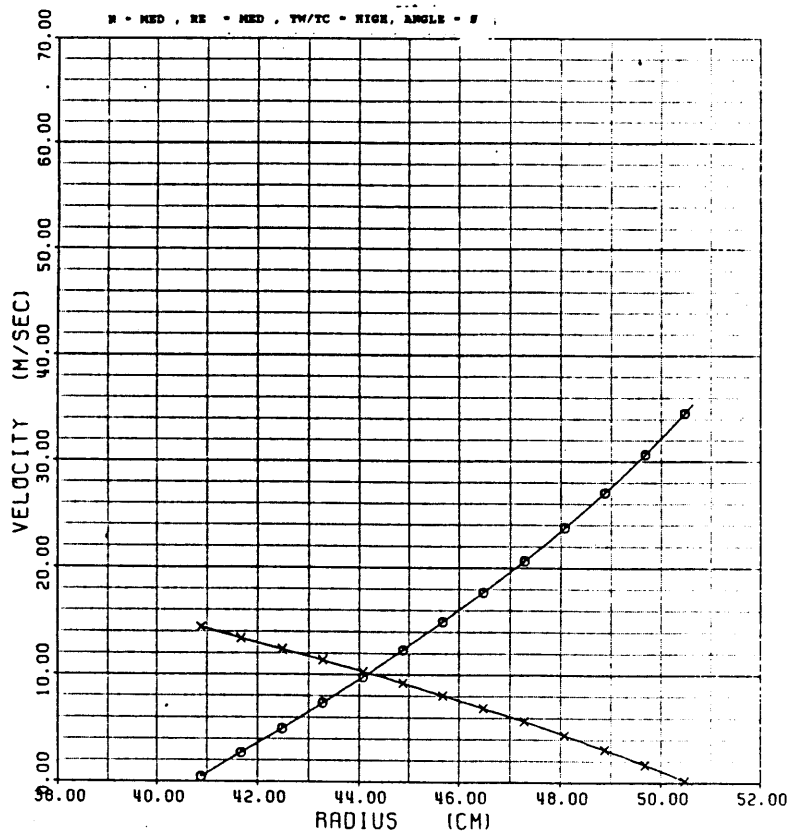


Figure 29A

# PRESSURE VS RADIUS

TEST #: 119

SYMBOLS: IMPINGEMENT - ○  
SUPPLY - X

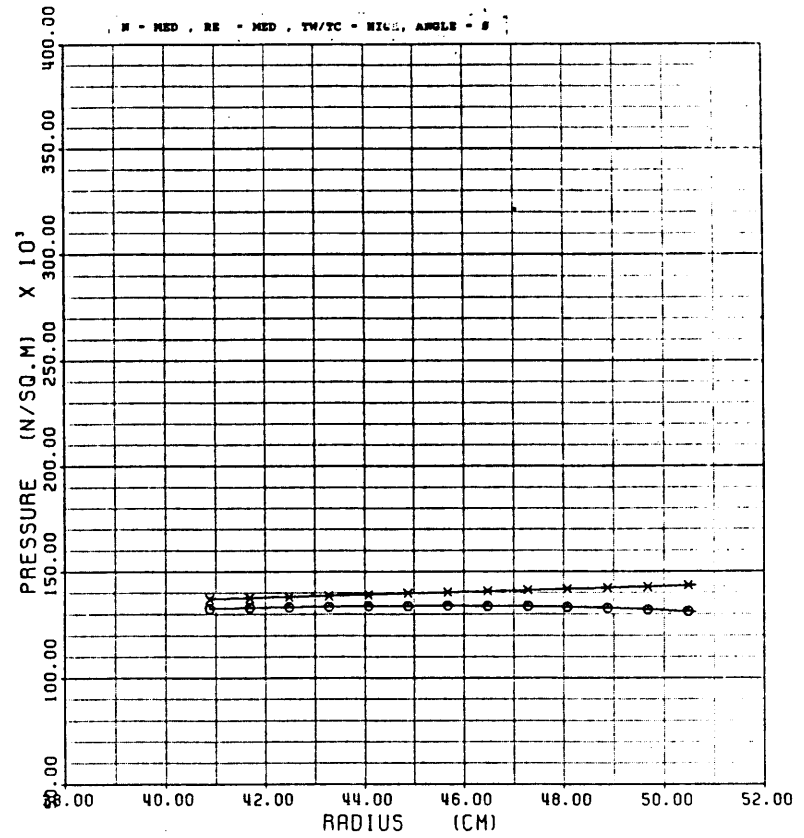


Figure 29B

### TEMPERATURE VS RADIUS

TEST #: 119

SYMBOLS: IMPINGEMENT -  $\circ$   
 SUPPLY -  $\times$   
 THERMOCOUPLE -  $\triangle$

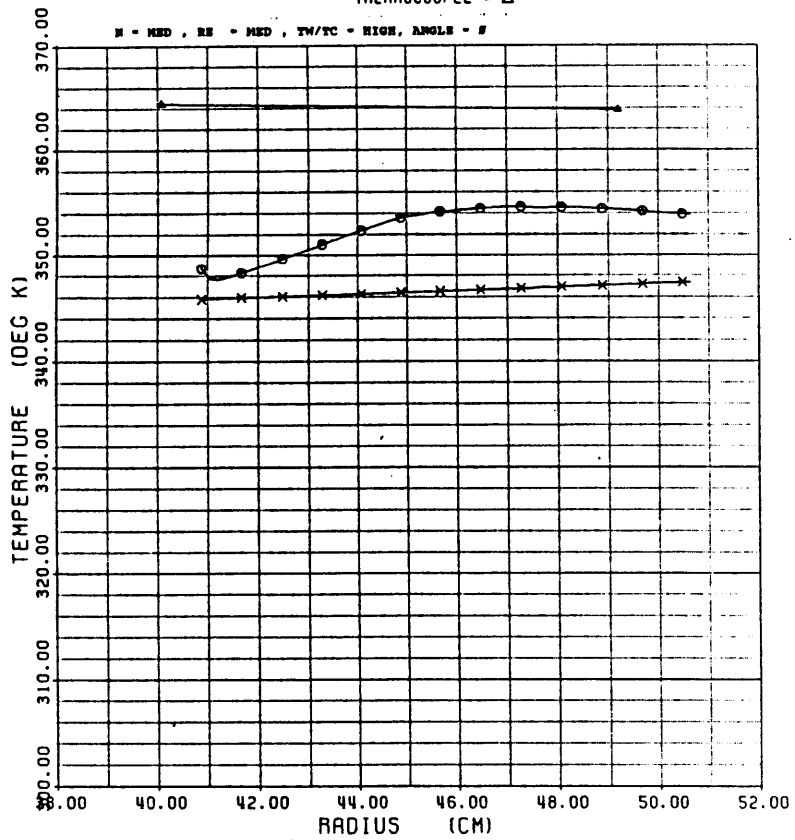


Figure 29C

### AVERAGE NUSSELT NUMBER

TEST #: 119

SYMBOLS: NU NO BASED ON LOCAL GAS TEMP -  $\circ$   
 NU NO BASED ON COOLANT TEMP -  $\times$   
 CHUPP'S CORRELATION -  $\triangle$   
 MORRIS' CORRELATION -  $\square$

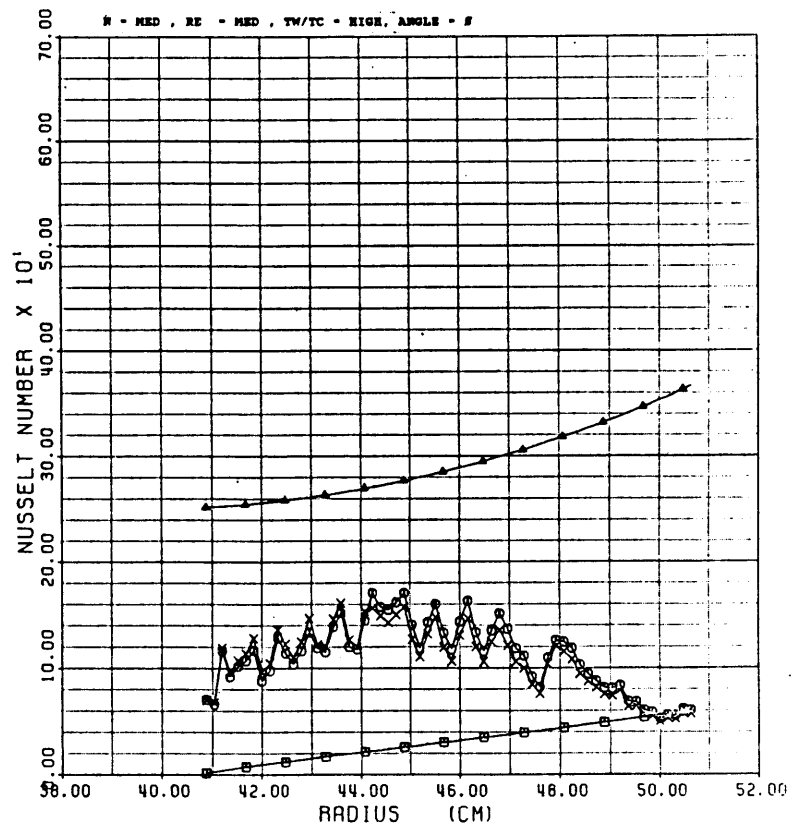


Figure 29D

VELOCITY VS RADIUS

TEST #: 120

SYMBOLS: IMPINGEMENT = ○  
SUPPLY = X

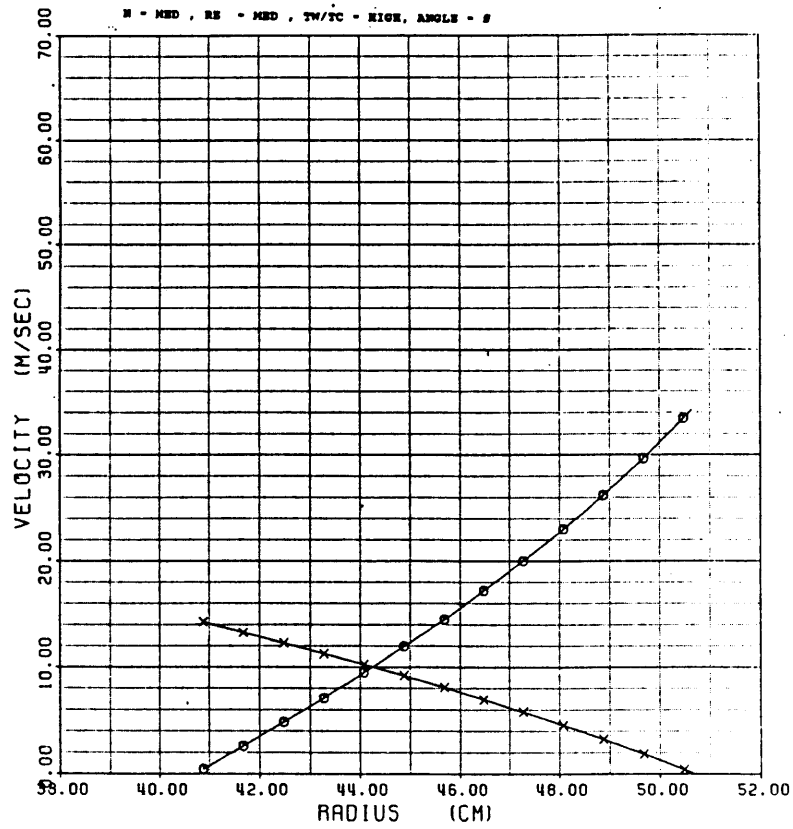


Figure 30A

PRESSURE VS RADIUS

TEST #: 120

SYMBOLS: IMPINGEMENT = ○  
SUPPLY = X

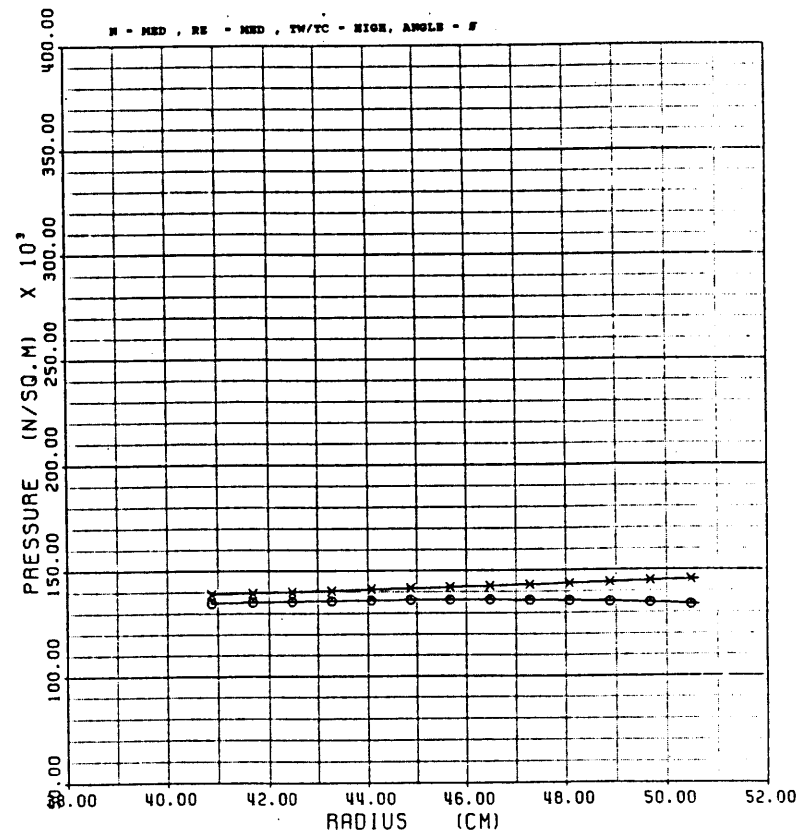


Figure 30B

### TEMPERATURE VS RADIUS

TEST #: 120

SYMBOLS: IMPINGEMENT = ○  
 SUPPLY = ×  
 THERMOCOUPLE = △

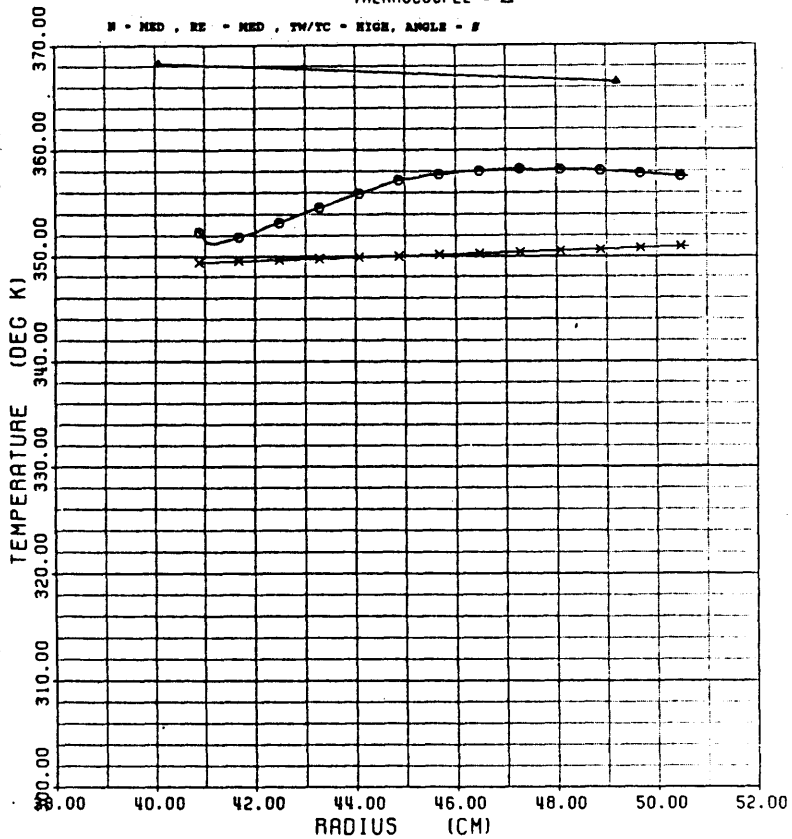


Figure 30C

### AVERAGE NUSSELT NUMBER

TEST #: 120

SYMBOLS: NU NO BASED ON LOCAL GAS TEMP = ○  
 NU NO BASED ON COOLANT TEMP = ×  
 CHUPP'S CORRELATION = △  
 MORRIS' CORRELATION = □

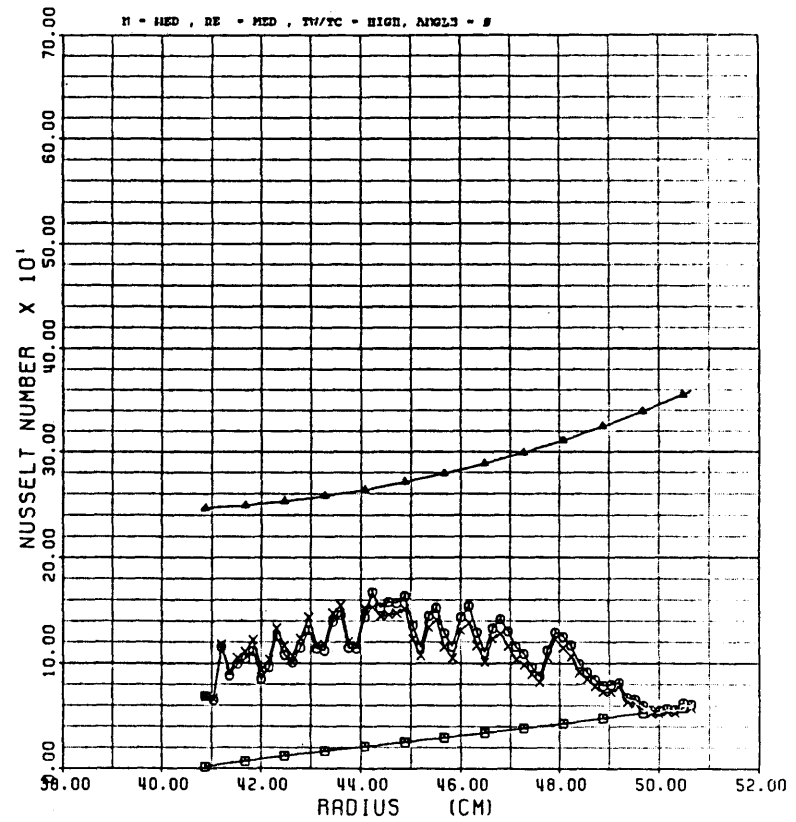


Figure 30D

### VELOCITY VS RADIUS

TEST #: 121

SYMBOLS: IMPINGEMENT - O  
SUPPLY - X

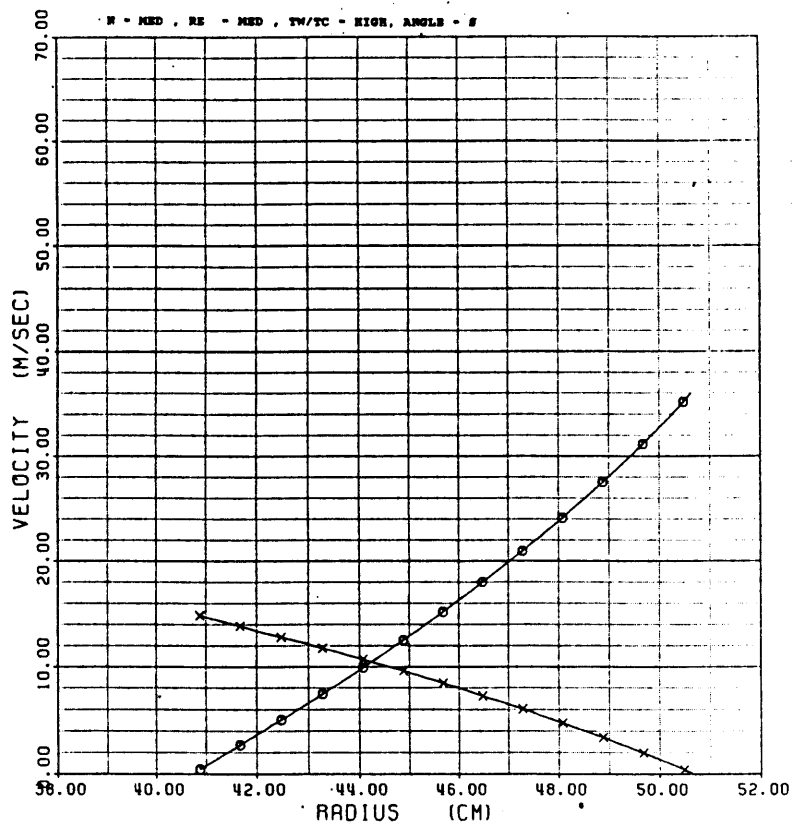


Figure 31A

### PRESSURE VS RADIUS

TEST #: 121

SYMBOLS: IMPINGEMENT - O  
SUPPLY - X

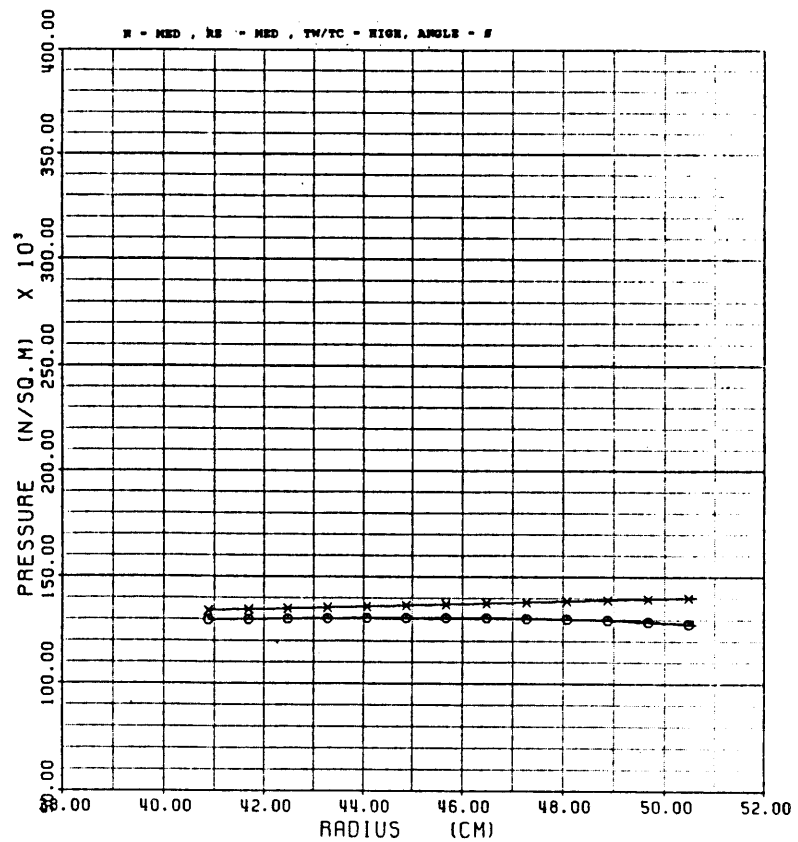


Figure 31B

### TEMPERATURE VS RADIUS

TEST #: 121

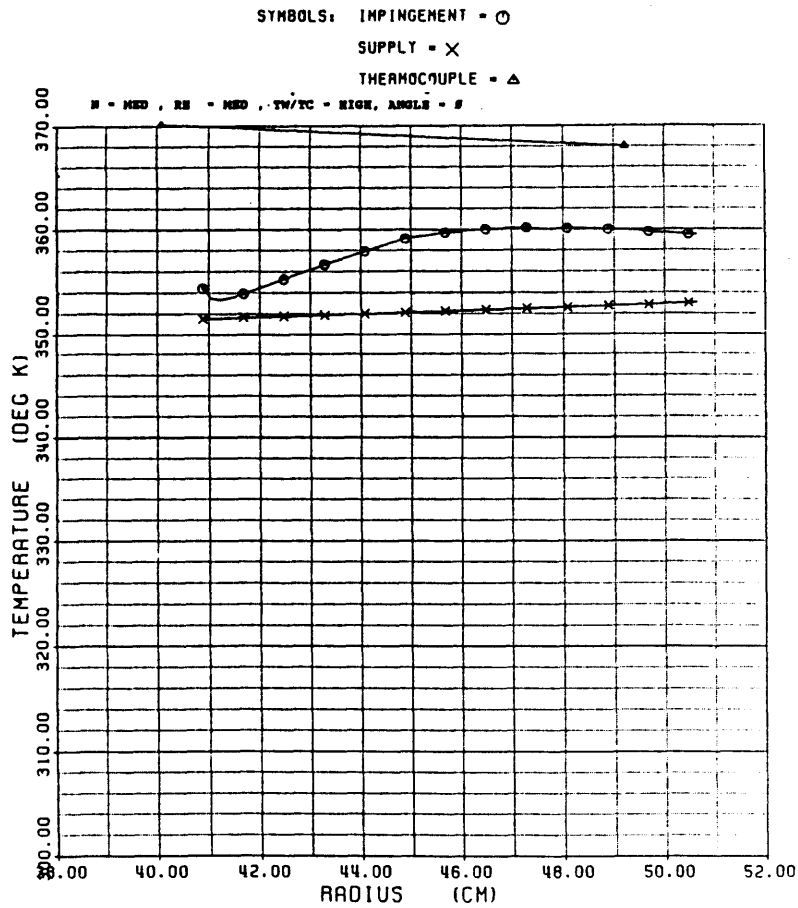


Figure 31C

### AVERAGE NUSSELT NUMBER

TEST #: 121

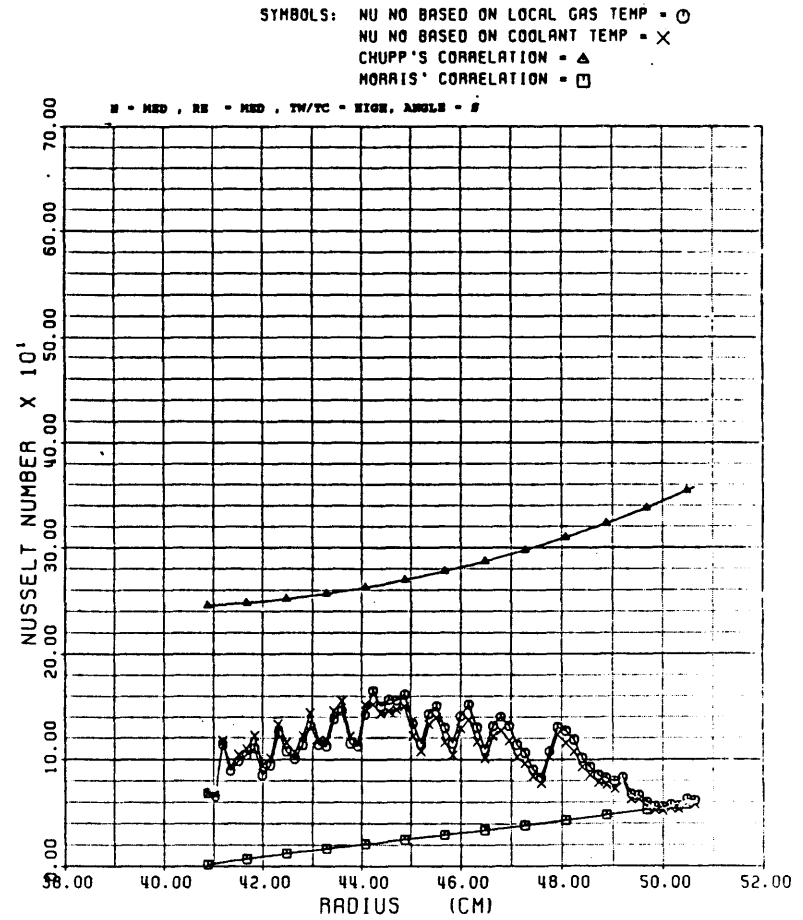


Figure 31D

### VELOCITY VS RADIUS

TEST #: 128

SYMBOLS: IMPINGEMENT - ○  
SUPPLY - X

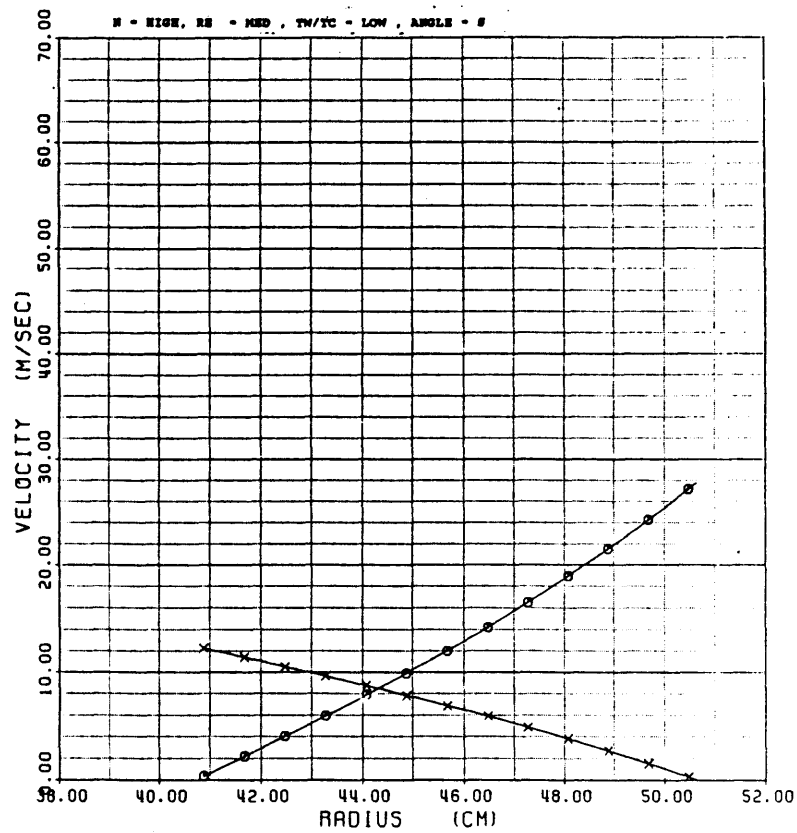


Figure 32A

### PRESSURE VS RADIUS

TEST #: 128

SYMBOLS: IMPINGEMENT - ○  
SUPPLY - X

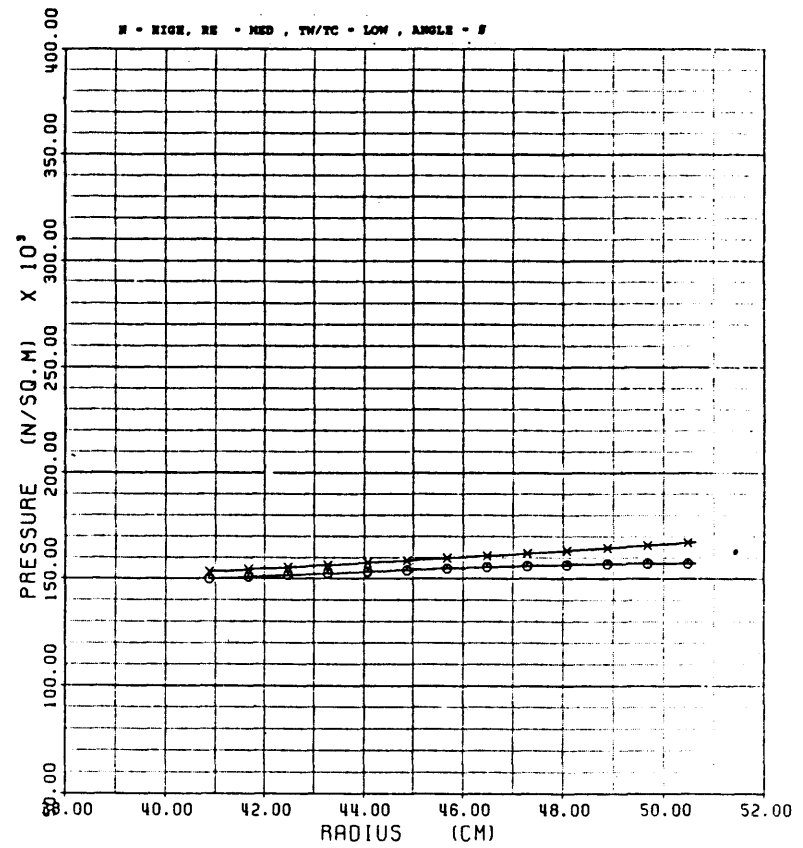


Figure 32B

### TEMPERATURE VS RADIUS

TEST #: 128

SYMBOLS: IMPINGEMENT -  $\circ$   
 SUPPLY -  $\times$   
 THERMOCOUPLE -  $\Delta$

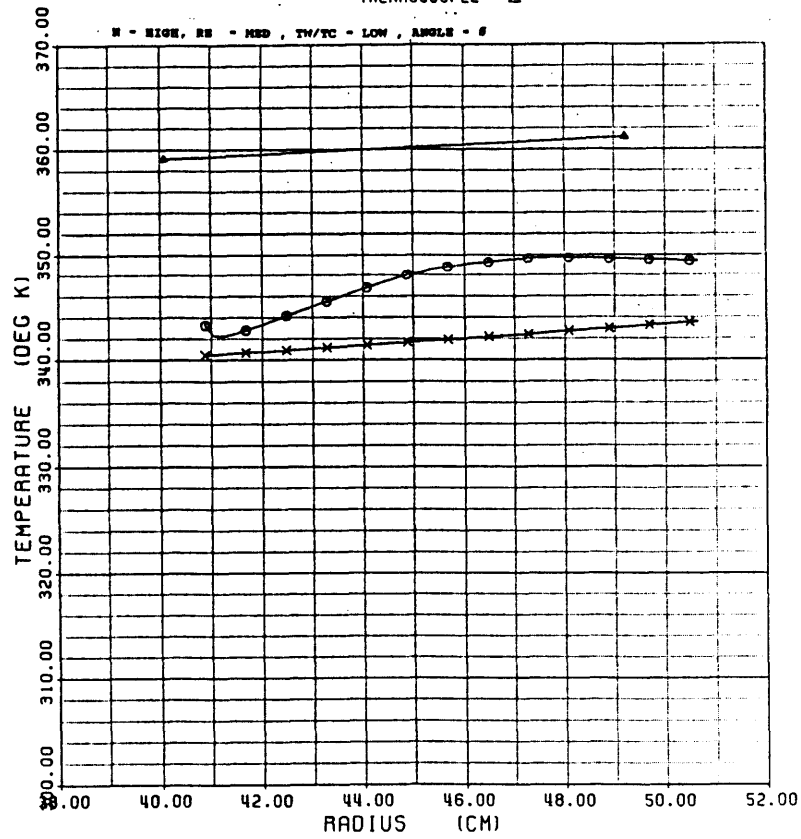


Figure 32C

### AVERAGE NUSSELT NUMBER

TEST #: 128

SYMBOLS: NU NO BASED ON LOCAL GAS TEMP -  $\circ$   
 NU NO BASED ON COOLANT TEMP -  $\times$   
 CHUPP'S CORRELATION -  $\Delta$   
 MORRIS' CORRELATION -  $\square$

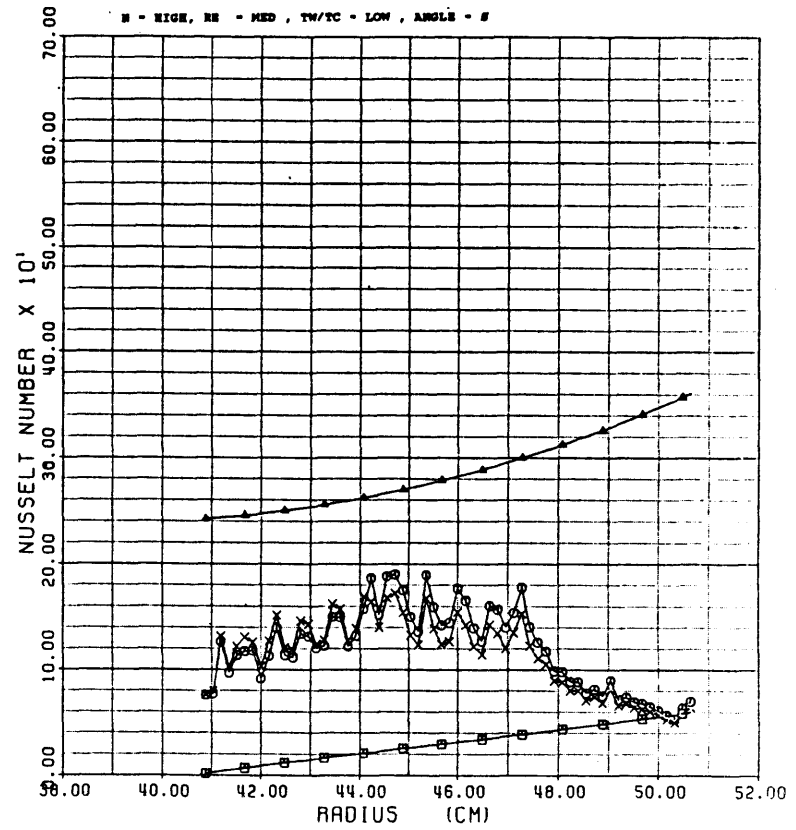


Figure 32D

### VELOCITY VS RADIUS

TEST #: 126

SYMBOLS: IMPINGEMENT - ○  
SUPPLY - X

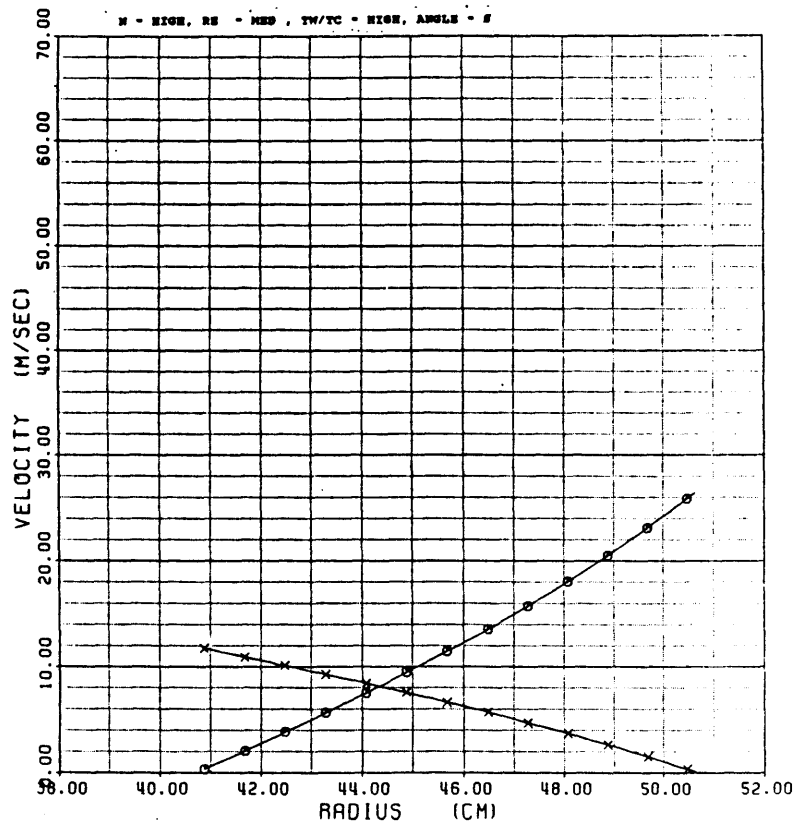


Figure 33A

### PRESSURE VS RADIUS

TEST #: 126

SYMBOLS: IMPINGEMENT - ○  
SUPPLY - X

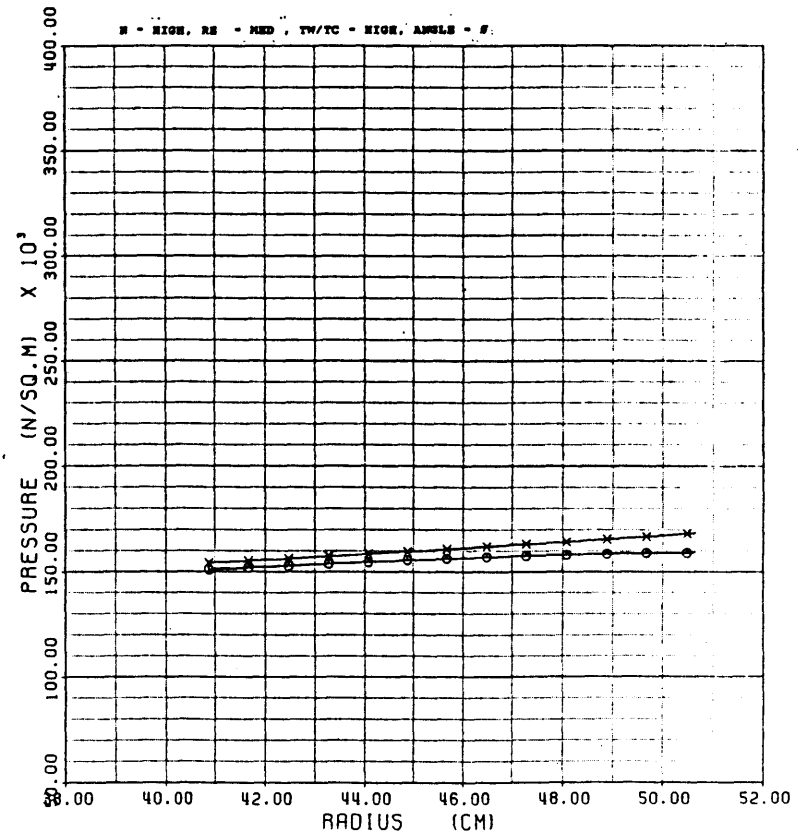


Figure 33B

### TEMPERATURE VS RADIUS

TEST #: 126

SYMBOLS: IMPINGEMENT -  $\circ$   
 SUPPLY -  $\times$   
 THERMOCOUPLE -  $\Delta$

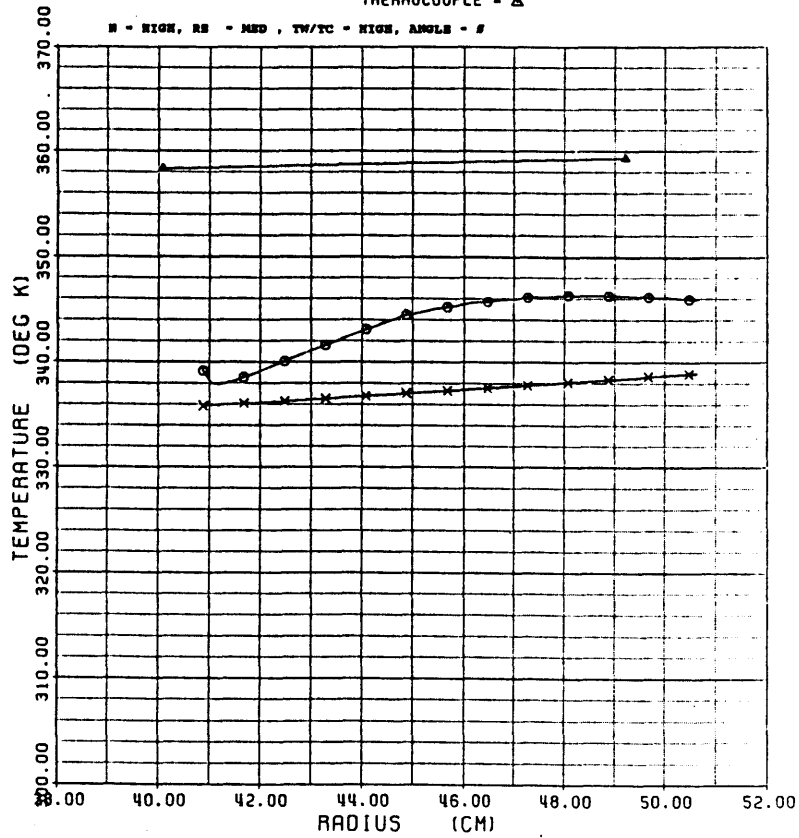


Figure 33C

### AVERAGE NUSSELT NUMBER

TEST #: 126

SYMBOLS: NU NO BASED ON LOCAL GAS TEMP -  $\circ$   
 NU NO BASED ON COOLANT TEMP -  $\times$   
 CHUPP'S CORRELATION -  $\Delta$   
 MORRIS' CORRELATION -  $\square$

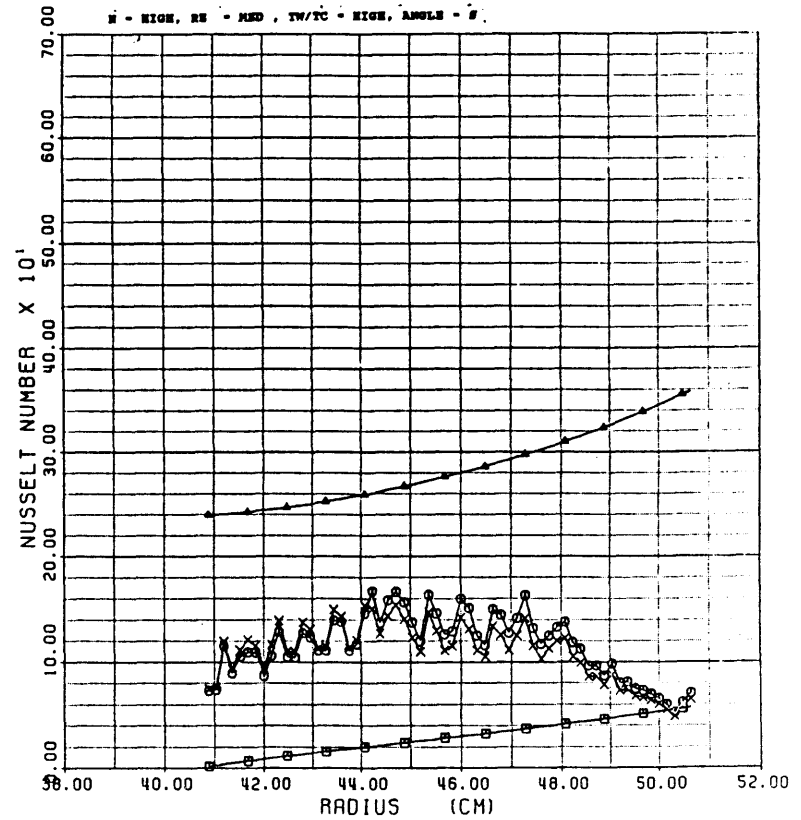


Figure 33D

### VELOCITY VS RADIUS

TEST #: 127

SYMBOLS: IMPINGEMENT - ○  
SUPPLY - X

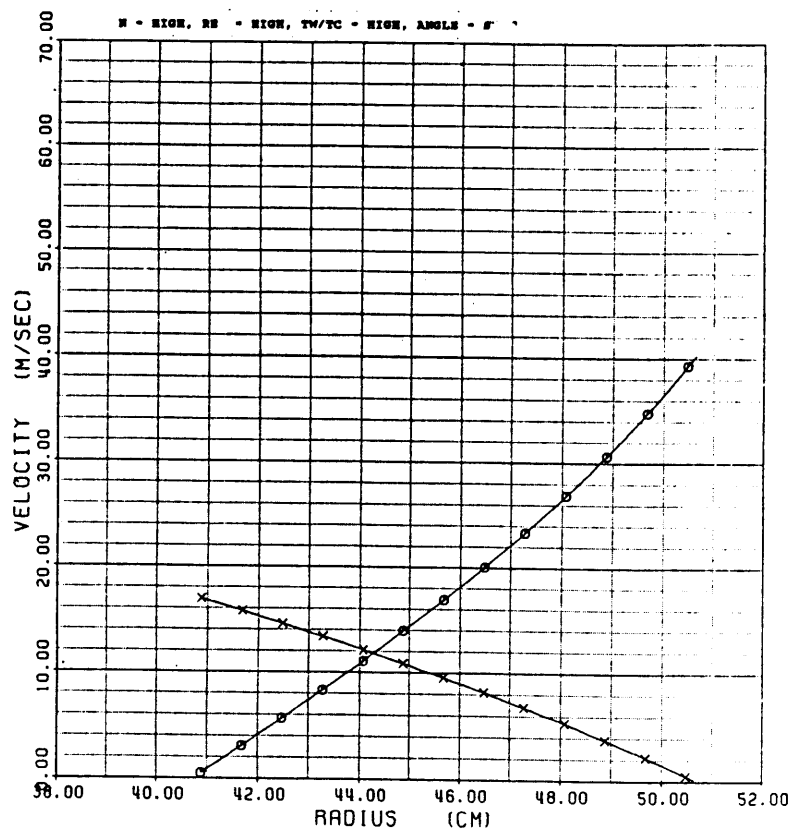


Figure 34A

### PRESSURE VS RADIUS

TEST #: 127

SYMBOLS: IMPINGEMENT - ○  
SUPPLY - X

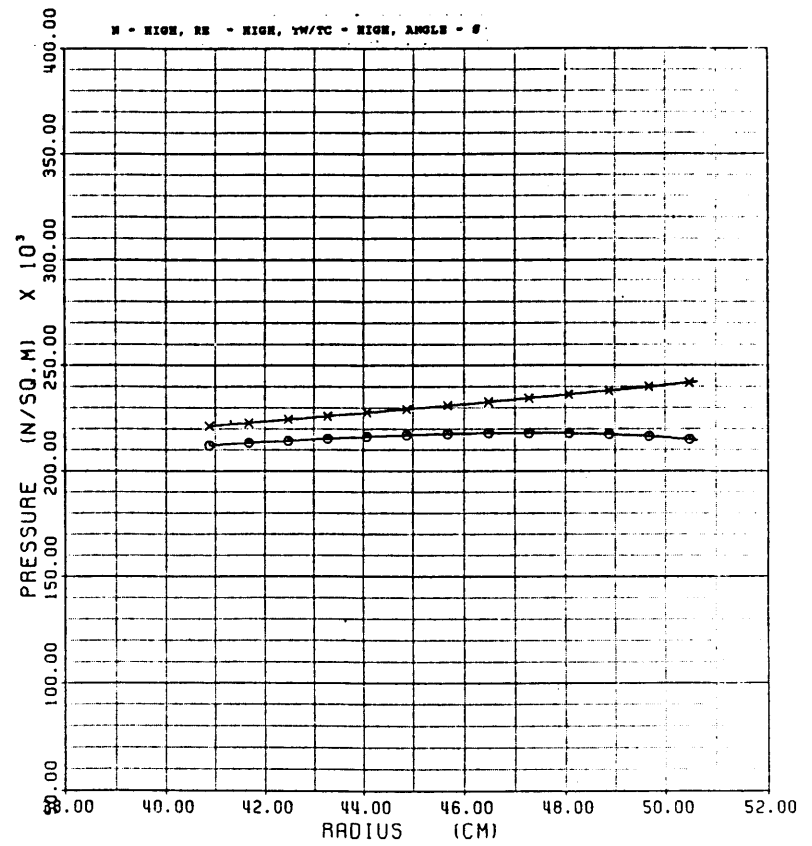


Figure 34B

### TEMPERATURE VS RADIUS

TEST #: 127

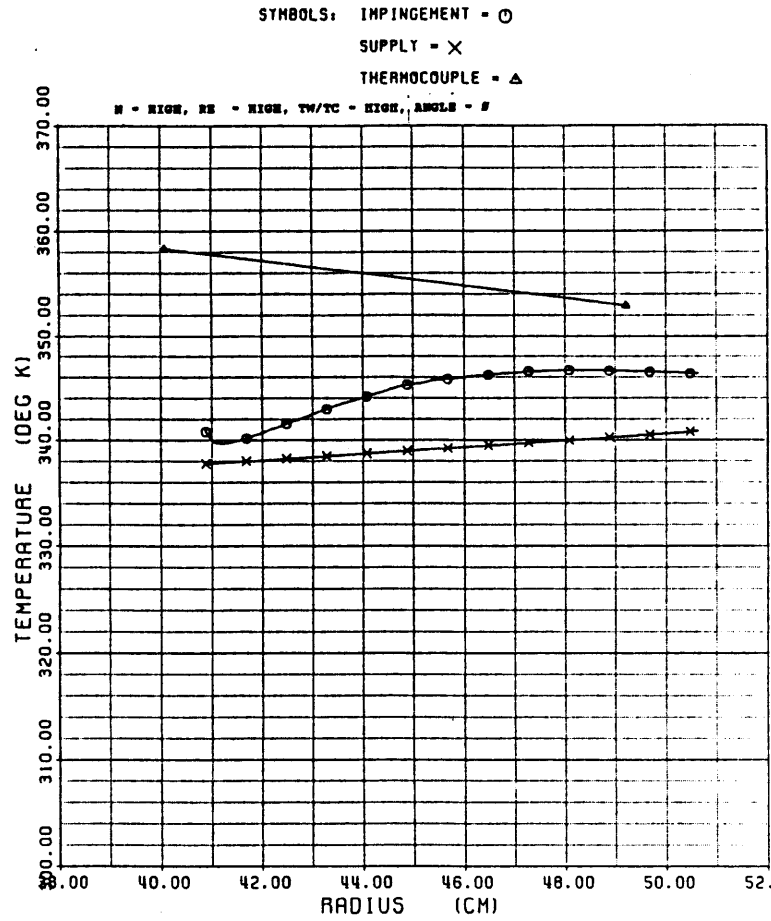


Figure 34C

### AVERAGE NUSSELT NUMBER

TEST #: 127

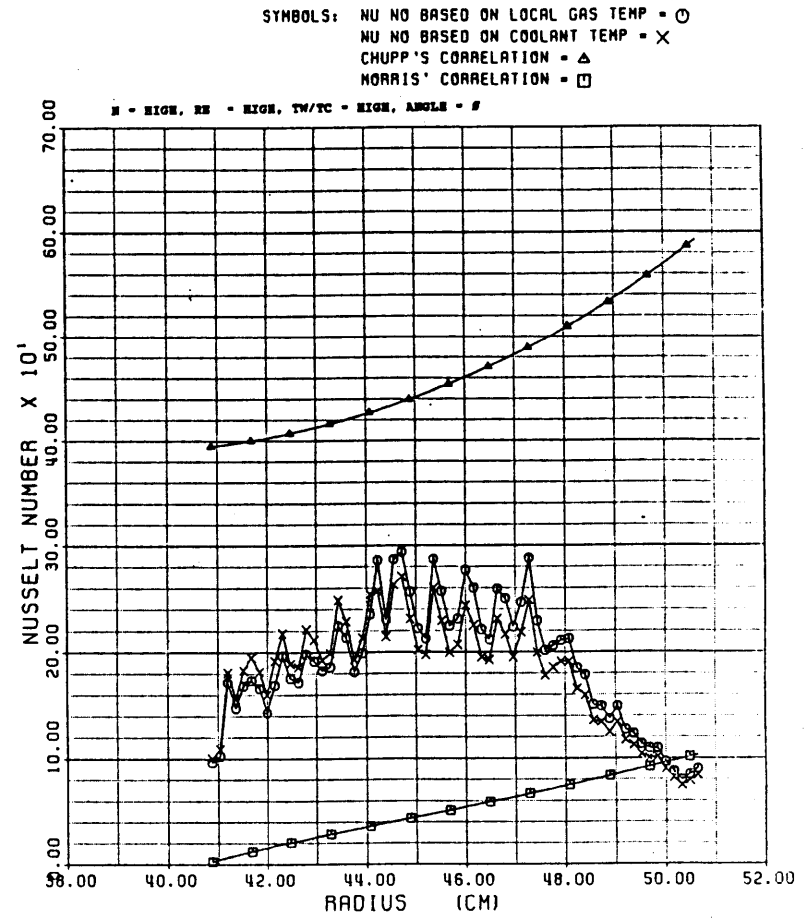


Figure 34D